UNIVERSITA' DEGLI STUDI DI NAPOLI "FEDERICO II"
C.I.R.Am. – Centro Interdipartimentale di Ricerca Ambiente

Dottorato di Ricerca in Analisi dei Sistemi Ambientali
XXV Cycle

PhD Thesis

Multiscale methods for CSEM data interpretation

Davide de Lerma di Castelmezzano

Tutor:
Prof. Maurizio Fedi

PhD Coordinator:
Prof. Maurizio Fedi

A mio padre e mia madre.

Contents

Introduction

“Oceans cover over three-fifths of the earth’s surface. Even though petroleum is produced from huge deposits on the relatively shallow continental shelf, the immense area of the ocean represents a largely unexplored and unexploited resource base. So, over the past few decades, the search for petroleum reserves has been extended from the continents offshore into progressively deeper water, making the continental shelves a focus for geophysical exploration” (Chave et al, 1991). The principal geophysical methods to discover oil reservoirs are the seismic methods, but there are marine geological areas in which the interpretation of seismic data may be difficult, such as regions dominated by scattering or high reflectivity, which is characteristic of carbonate reefs, volcanic cover, and submarine permafrost. So, complementary geophysical techniques are often required to study these regions. In recent years, significant advances have been obtained in theory, methodology, and instrumentation for marine EM methods. Many of the seafloor techniques are however simple adjustments of standard terrestrial EM approach (Chave et al, 1991).

In particular, during my work, I focused my attention on “marine Controlled Source ElectroMagnetic sounding" (mCSEM), which is a EM method getting information about the resistivity distribution beneath the sea-floor. mCSEM uses a low frequency EM signal generated by a transmitter antenna towed by a ship and received by an array of receivers deployed at sea-floor. The first publication proposing marine CSEM measurements is probably that of Bannister (1968), who presented theory for frequency-domain, seafloor-to-seafloor dipole-dipole measurements to determine seabed resistivity. Bannister also recognized the noise problems associated with magnetometers moving in the earth’s

main field and recommended the horizontal electric dipole (HED) configuration, which is still used today.

This method is very useful for oil companies because it can be used to detect and locate oil reservoir; although, to date, most marine CSEM activity has been carried out for exploration and pre-drilling appraisal, it could be also useful in monitoring the production of reservoirs, as described in two recent papers (Lien and Mannseth, 2008; Orange et al., 2009). Further applications of marine CSEM are the exploration for gas hydrates as a methane resource, and possibly pre-drilling surveys to mitigate hazard represented by hydrates and shallow gas. First proposed by Edwards (1997), the use of marine EM to study seafloor gas hydrate is gaining attention (Yuan and Edwards, 2000; Schwalenberg et al., 2005; Weitemeyer et al., 2006; Darnet et al., 2007; Evans, 2007; Ellis et al., 2008; Zach and Brauti, 2009; Schwalenberg et al., 2010). The reason of this trend is that the concentration of hydrate in the sedimentary section is difficult to be quantified using seismic alone (Constable, 2010).

During my work, in particular, I have developed two methods for the interpretation of mCSEM data.

The first method, that we call "Singular Function Normalization" method (SFN) is a fast and computationally low cost method to get information about the areal resistivity distribution. The method is based on the study of the "Magnitude Versus Offset" signals (MVO). The MVOs are the values of the amplitude of the electric field measured by a receiver versus the distance source-receiver (offset), usually represented in a semi-logarithmic scale. Our aim is at emphasizing the presence of anomalous resistive buried bodies, by approximating the MVO signal obtained at each receiver by a singular function, such as the Lipschitz-Hölder singularity function: $y = A|x|^{-b}$ and estimating, for each receiver, its exponent. This parameter is expected to vary on the set of the MVO curves acquired during the survey, so to reflect the presence of the anomalous body. Another singularity function we have considered is the Exponential Singularity Function (ESF): $y = Ae^{-b|x|}$. In this case we estimate the coefficient of the exponent b of the best-fit ESF. The

method was successfully tested on synthetic data and then was applied to a real dataset kindly allowed by eni. In this latter case, the results are in agreement with the published results obtained by anisotropic 3D inversion (Dell'Aversana, 2012).

The second proposed method is the Depth from Extreme Points (DEXP) method (Fedi, 2007) applied to mCSEM data. The DEXP method is used in potential field in order to get a fast imaging of the source distribution and have information about the depth to the source, the structural index, *N,* and the mass or magnetic moment modulus, respectively for gravity and magnetic data (Fedi, 2007). In particular, this method fits in the framework of semi-automatic methods, as Euler Deconvolution method, used in potential field to estimate the source position and *N* (Reid el al, 1990). *N* is a source-dependent parameter, which corresponds to the fall-off rate of the field with distance for many, but not all, ideal sources. A more general meaning of *N* is that it is the opposite of the homogeneity degree of the field.

During this work I have shown that it is possible to apply this method also to non-static fields, such as low-frequency electromagnetic fields, under specific assumptions. In particular, I have applied the method to the electric field scattered by buried resistive sources. The DEXP method (Fedi, 2007; Fedi and Abbas, 2013) is based on the evaluation of the static field (magnetic, gravity or self-potential) at altitudes higher than the measurement altitude thanks to a routine procedure called upward-continuation (Blakely, 1995). Equivalently, I have shown (Chapter 3) that upward-continuation may be well established also for low-frequency non-static fields, under the condition that the distance from the source is kept less than the skin-depth δ. So, similarly to potential fields, we can get in a fast way, and without any *a-priori* information, the position and the structural index of the anomalous resistive bodies buried beneath the sea-floor. In a similar way, I have demonstrated that is possible to apply to mCSEM data also a geometric method called *multi-ridge* method, developed by Fedi et al.(2009) for potential field data, again under the condition that the distance from the source is less than the skin-depth. This method is very fast and gives information about the depth and horizontal position of the sources, while it does not provide a direct

estimation of the structural index. As the DEXP method, the *multi-ridge* method is based on the upward-continuation of the electromagnetic field scattered by the buried resistive sources. By this method we: (a) built some characteristic lines in the upward continuation domain, formed by joining the maxima of the vertical and horizontal derivatives of the field, at distances less than skin-depth, and (b) extrapolate them below the measurement level until they intersect each other. For ideal and isolated sources such lines are straight and, as it is demonstrated in the Paragraph 3.2, intersect in correspondence of the source of the scattered electro-magnetic field.

The DEXP and multi-ridges methods were tested on synthetic data obtained starting from simple models, such as a uniform resistive sphere buried in a half-space or an infinite horizontal cylinder buried in an half-space, and from more complex models such as a horizontal finite thin resistive layer buried in a half-space. Moreover, the DEXP method was tested on the real data-set provided by eni and the results were compared with the results obtained using 3D anisotropic inversion (Dell'Aversana, 2012) showing a good agreement with them.

Chapter 1

Controlled Source Electromagnetic methods

1.1 The CSEM methods

All the electromagnetic methods using an antenna as source of the electromagnetic field can be considered “Controlled Source ElectroMagnetic” methods (CSEM).

CSEM sounding has been used since 1930’s to get information about the resistivity distribution in the subsurface.

A land CSEM sounding is the Controlled Source Audio-frequency Magneto-Telluric method (CSAMT). This is a frequency domain electromagnetic sounding technique, using as source of the electromagnetic field a fixed grounded dipole or horizontal loop. CSAMT is similar to the natural-source magnetotellurics (MT) and audio-frequency magnetotellurics (AMT) techniques; the chief differences are about the use of an artificial CSAMT signal source and about the distance, being it finite in CSEM.

Using an artificial source allows us to have higher precision and more economical measurements than those usually obtainable with natural-source measurements in the same spectral bands, but the use of controlled source can also be problematic by adding source effects and logistical restrictions on the survey. However, the method has proven particularly effective in mapping the upper 2 to 3 km of the earth's crust. The CSAMT source usually consists of a grounded electric dipole about

1 to 2 km in length, ideally located at least four skin depths from the area where soundings are to be made. Measurements are made within the 0.1 Hz to 10 kHz frequency band. The signal generated by the source and propagating in the subsurface is acquired by grounded dipoles and magnetic receivers which measure amplitude and phase of the electric and magnetic field components respectively. The ratio of orthogonal, horizontal electric and magnetic field magnitudes yields the apparent resistivity. The difference between the phase of the electric and magnetic fields yields the phase of the impedance. In tensor measurements, these quantities may be treated by standard MT processing techniques. "Since its introduction in the mid-1970s, CSAMT has been used in exploration for petroleum, geothermal resources, massive sulfides, base and precious metals, structure, lithology, and sources of groundwater contamination" (Zonge and Hughes, 1991).

Another CSEM sounding technique is the marine Controlled Source Electromagnetic Method (mCSEM). This method is actually used by the oil companies as support to other geophysical methods as seismic methods to discover oil reservoirs beneath the seafloor. The mCSEM mostly uses as source of the EM field a "Horizontal Electric Dipole" (HED) which generates a signal having a fundamental frequency ranging from 0.1-10 Hz. The marine CSEM method has become a method of commercial interest in the last years because it is very sensitive to the presence of thin resistive bodies such as oil and gas reservoir. In fact, the HED system combines TM and PM modes and is preferred to MT sounding when resistive zones have to be mapped (Zonge and Hughes, 1991). We will describe more accurately the TM and PM modes in the Paragraph 1.2.

mCSEM method provides information about the conductivity of the subsurface that is strictly linked to pore volume and fluid properties. For this reason this method can be also used to monitor the CO_2 stored underground to reduce the pollution due to mining activities.

1.2 The resistivity of the rocks

The electrical conductivity of the rocks is a function of the porosity and permeability of the rocks and of the pore fluid conductivity.

Electric current may be propagated in rocks and minerals in three ways: electronic (ohmic), electrolytic, and dielectric conduction. The first is the normal type of current flow in materials containing free electrons such as metals. In an electrolyte the current is carried by ions at a comparatively slow rate. Dielectric conduction takes place in poor conductors or insulators, which have very few free carriers or none at all (Telford et al., 1990). Under the influence of an external varying electric field, the atomic electrons are displaced slightly with respect to their nuclei; this slight relative separation of negative and positive charges is known as dielectric polarization of the material and it produces a current known as the *displacement current.*

The *electrical resistivity* of a cylindrical solid of length L and cross section A, having resistance R between the end faces, is given by:

$$\rho = \frac{RA}{L} \tag{1.1}$$

If A is in square meters, L in meters, and R in ohms, the resistivity unit is the ohm by meter (Ωm). The resistance R is given in terms of the voltage V applied across the ends of the cylinder and the resultant current l flowing through it, by Ohm's law:

$$R = V/I \tag{1.2}$$

The electric conductivity σ is the reciprocal of the resistivity, so will be given by:

$$\sigma = \frac{1}{\rho} = \frac{L}{RA} = \frac{\frac{I}{A}}{\frac{V}{L}} = \frac{J}{E} \tag{1.3}$$

where J is the current density (A/m) and E is the electric field (V/m). The units of σ are Siemens per meter (S/m).

Most of the rocks are characterized by high values in resistivity, but may be seen as conductive due to the fluids inside the pores. As result the rocks are *electrolytic conductors,* whose effective resistivity may be defined as in equation (1.1)*,* where the propagation of current is by ionic conduction, e.g. by conduction of molecules having an excess or deficiency of electrons. Hence the resistivity varies with the mobility, concentration, and degree of dissociation of the ions; the latter depends on the dielectric constant of the solvent (Telford et al, 1990). There are various ways to model porosity and water content. The most popular is Archie's Law (1942):

$$\sigma = \sigma_S + \left(\sigma_f - \sigma_S\right)\beta^m \tag{1.4}$$

where the exponent *m* is between 1.5 and 2.0 (determined empirically), σ_S is the conductivity of the mineral grains, σ_f is the conductivity of the fluid and β is the fluid fraction (or porosity, if saturated).

There are several other models on which mixing laws can be based, for example fluid filled tubes:

$$\sigma = \frac{1}{3}\beta\sigma_f + (1-\beta)\sigma_s \tag{1.5}$$

All possible isotropic models must lie between the Hashin-Shtrikman (HS) bounds:

$$HS^- = \sigma_S + \beta\left(\frac{1}{\sigma_f - \sigma_S} + \frac{1-\beta}{3\sigma_S}\right)^{-1} \tag{1.6}$$

$$HS^+ = \sigma_f + (1 - \beta)\left(\frac{1}{\sigma_S - \sigma_f} + \frac{\beta}{3\sigma_f}\right)^{-1} \tag{1.7}$$

The geometrical arrangement of the interstices in the rock has a less pronounced effect, but may make the resistivity anisotropic, meaning that it may have different values as the current flows in different directions.

Anisotropy is characteristic of stratified rocks, which are generally more conductive in the bedding plane. The anisotropy, whose effect depends

on the maximum to minimum resistivity ratio, may be as large as 2 in some graphitic slates, and varies from l to 1.2 in rocks such as limestone, shale, and rhyolite (Telford et al., 1990).

The third type of current flow is the *displacement current*. This kind of current flows only in non-conductors when the external electric field changes with time. This kind of conduction is also knows as dielectric conduction. The significant parameter in dielectric conduction is the *dielectric constant k,* sometimes called the *specific inductive capacity* of the medium.

As we will see in Chapter 3, the displacement currents are of secondary importance, at the frequencies used in mCSEM sounding.

1.3 Basics physics of EM

Both MT and CSEM sounding use electromagnetic induction, which describes what happens around a time-varying primary field.

Michael Faraday proved that the electromotive force (EMF) produced around a closed path is proportional to the rate of change of the magnetic flux through any surface bounded by that path. In practice, this means that an electric current will be induced in any closed circuit when the magnetic flux changes through a surface bounded by the conductor.

In particular Faraday's law says that a time varying magnetic field will induce an electric field in a conductor:

$$\oint_C \mathbf{E} \cdot d\mathbf{l} = -\frac{d\Phi}{dt} \tag{1.8}$$

where Φ is the magnetic flux.

The induced electric field **E** will generate a current **I** with a density current **J** in a conductor, according to the Ohm's law:

$$\mathbf{J} = \sigma \mathbf{E} \tag{1.9}$$

This current, following the Ampere's law will generate a secondary magnetic field:

$$\oint_C \mathbf{B} \cdot d\mathbf{l} = \mu I \tag{1.10}$$

The secondary field opposes to the changes in the primary field. The consequence of this is that conductive rocks will absorb variations of EM fields more than resistive rocks.

Operationally, an alternating magnetic field is established by the circulation of alternating current through a coil or along a very long wire. This field is measured with a receiver consisting of a coil or a dipole connected to a sensitive electronic meter, or potentiometer bridge. The frequency of the alternating current is chosen such that an insignificant eddy-current field is induced in the ground, assuming it has an average electrical conductivity. But if the source and receiver are brought near a more conductive zone, stronger eddy currents may be caused to circulate within it and an appreciable secondary magnetic field will thereby be created. Close to the conductor this secondary or anomalous field may be comparable in magnitude with the primary or normal field (which prevails in the absence of conducting zones), in which case the receiver can very easily detect it. Prospecting for these anomalous zones is carried out by systematically traversing the ground either with the receiver unit alone or with the source and receiver in combination, depending upon the system in use.

Equations 1.8 and 1.10 can be expressed also as differential equations, so equation 1.8 will be rewritten as:

$$\nabla \times \mathbf{E} = -\frac{\partial \mathbf{B}}{\partial t} \tag{1.11}$$

and equation 1.10 becomes:

$$\nabla \times \mathbf{H} = \mathbf{J} + \frac{\partial \mathbf{D}}{\partial t} \tag{1.12}$$

where:

B is the magnetic induction in webers per square meter;

H is the magnetic field intensity in Ampere-turns per meter;

E is the electric field intensity in volts per meter;

D is the electric displacement in coulombs per square meter;

J is the electric current density in ampere per square meter;

Equations 1.11 and 1.12 are the first and second Maxwell's equation respectively.

By taking the divergence of 1.11, we obtain:

$$\begin{aligned} \nabla \cdot \nabla \times \mathbf{E} = 0 &= -\nabla \cdot \frac{\partial \mathbf{B}}{\partial t} \\ &= -\frac{\partial}{\partial t} \nabla \cdot \mathbf{B} \end{aligned} \tag{1.13}$$

because the divergence of a rotor is zero. The divergence of **B** is therefore time-independent, and since **B** is generally time-varying, it follows that:

$$\nabla \cdot \mathbf{B} = 0. \tag{1.14}$$

This is the third Maxwell's equation.

Instead, considering the divergence of (1.12) we obtain:

$$\begin{aligned} \nabla \cdot \nabla \times \mathbf{H} = 0 &= \nabla \cdot \mathbf{J} + \nabla \cdot \frac{\partial \mathbf{D}}{\partial t} \\ &= \nabla \cdot \mathbf{J} + \frac{\partial}{\partial t} \nabla \cdot \mathbf{D} \end{aligned} \tag{1.15}$$

To reduce this further, we must employ a relationship involving the electric charge density q. The equation of continuity, which follows from the definition of current as the rate of flow of indestructible charge, is:

$$\nabla \cdot \mathbf{J} = -\frac{\partial q}{\partial t} \tag{1.16}$$

and therefore we obtain:

$$\frac{\partial}{\partial t}(\nabla \cdot \mathbf{D} - q) = 0 \tag{1.17}$$

Since both **D** and q may be time-varying, this suggests that:

$$\nabla \cdot \mathbf{D} = q \tag{1.18}$$

This is the fourth Maxwell's equation.

Due to the fact that in any region of non-vanishing conductivity the charge density will reach its equilibrium in an extremely short time, and the charge does not accumulate appreciably during the flow of current, so that (Grant and West, 1965):

$$\nabla \cdot \mathbf{J} = 0 \tag{1.19}$$

and therefore also:

$$\nabla \cdot \mathbf{E} = \nabla \cdot \mathbf{D} = 0 \tag{1.20}$$

As we can see, the first two Maxwell's equations are vectorial equations and the last two ones are scalar equations. So, we have an under-determined system because we have a system of eight equations with five unknowns.

Hence, the problem of the solution of the Maxwell's equations is undetermined and the eight Maxwell's equations are not independent.

To reduce the number of Maxwell's equations we have to consider other relationship. These are two empirical relationships, named *constitutive equations* that, for an isotropic linear material, are:

$$\mathbf{D} = \varepsilon \mathbf{E} \tag{1.21}$$

$$\mathbf{H} = \frac{\mathbf{B}}{\mu} \tag{1.22}$$

where μ is the magnetic permeability ($\mu = \mu_r \mu_0$, where μ_r is the relative magnetic permeability and μ_0 is the magnetic permeability of the free space ($4\pi \times 10^{-7}$H/m)) and ε is the electric permittivity ($\varepsilon = \varepsilon_r \varepsilon_0$, where ε_r is the relative electric permittivity and ε_0 is the electric permittivity of the free space (8.854×10^{-12} Farad/m)).

By using the relations (1.21 and 1.22), we can eliminate three of the five variables from Maxwell's equations and reduce them to the following set:

$$\nabla \times \mathbf{E} = -\mu \frac{\partial \mathbf{H}}{\partial t} \tag{1.23}$$

$$\nabla \cdot \mathbf{H} = 0 \tag{1.24}$$

$$\nabla \times \mathbf{H} = \sigma \mathbf{E} + \varepsilon \frac{\partial \boldsymbol{E}}{\partial t} \tag{1.25}$$

$$\nabla \cdot \mathbf{E} = 0 \tag{1.26}$$

The four equations can be reduced still further by taking the curl of 1.23 and 1.24 and substituting each into the other. Then, by making use of the vector identity: $\nabla \times (\nabla \times \mathbf{A}) = \nabla(\nabla \cdot \mathbf{A}) - \nabla \cdot \nabla \mathbf{A} = \nabla(\nabla \cdot \mathbf{A}) - \nabla^2 \mathbf{A}$ where $\nabla^2 \mathbf{A}$ is to be interpreted as the Laplacian operator acting on the *rectangular components* of **A**, we obtain (Grant and West, 1965):

$$\nabla^2 \mathbf{E} - \sigma\mu \frac{\partial \mathbf{E}}{\partial t} - \varepsilon\mu \frac{\partial^2 \mathbf{E}}{\partial t^2} = 0 \tag{1.27}$$

$$\nabla^2 \mathbf{H} - \sigma\mu \frac{\partial \mathbf{H}}{\partial t} - \varepsilon\mu \frac{\partial^2 \mathbf{H}}{\partial t^2} = 0 \tag{1.28}$$

From these two necessary (but not sufficient) relationships we observe that both **E** and **H** must propagate as a dissipative wave motion. These are the wave equations; we have to consider these two equations when the frequencies are high (as in GPR sounding).

In most cases we shall be dealing with alternating fields, and we may therefore assume for **H** and **E** a time dependence which is of the form: $\mathbf{H}(\mathbf{r}, t) = \mathrm{Re}\mathbf{H}(\mathbf{r}, \omega)e^{i\omega t}$ where ω is the angular frequency of the field. In this case equations 1.27 and 1.28 become:

$$\nabla^2 \mathbf{E} = i\sigma\mu\omega\mathbf{E} - \varepsilon\mu\omega^2\mathbf{E} \tag{1.29}$$

$$\nabla^2 \mathbf{H} = i\sigma\mu\omega\mathbf{H} - \varepsilon\mu\omega^2\mathbf{H} \tag{1.30}$$

The term $\mu\varepsilon\omega^2 - i\mu\sigma\omega$ is the propagation constant or wave number k^2:

$$k^2 = \mu\varepsilon\omega^2 - i\mu\sigma\omega = \mu\omega(\varepsilon\omega - i\sigma)\mathrm{Re}(k) > 0 \quad (1.31a)$$

$$k^2 = -\gamma^2 = -i\mu\omega(\sigma + i\omega\varepsilon)\mathrm{Im}(k) < 0 \quad (1.31b)$$

Hence, the wave equations can be rewritten as:

$$\nabla^2\mathbf{E} + k^2\mathbf{E} = 0 \quad (1.32)$$

$$\nabla^2\mathbf{H} + k^2\mathbf{H} = 0. \quad (1.33)$$

The first term $(\varepsilon\omega)$ in the parentheses of equation 1.31a is the displacement term, which dominates at high frequencies and in a nonconductive medium. The second term$(\sigma)$is the conduction term, which dominates when frequencies are low and when the medium is relatively conductive.

Now we treat the problem of the wave propagation in the quasi-static limit, following the approach described in Zonge and Hughes, 1991.

The dominance of the conduction term over the displacement term holds for most earth materials at mCSEM frequencies. Following the convention of Ward and Hohmann (1988, Chapter 4, Volume 1), the propagation constant can be written in complex form as:

$$k = \alpha - i\beta = [-i\mu\omega(\sigma + i\omega\varepsilon)]^{1/2} \quad (1.34)$$

In which the phase constant α is given by:

$$\alpha = \omega\left[\frac{\mu\varepsilon}{2}\left(\sqrt{1 + \left(\frac{\sigma}{\varepsilon\omega}\right)^2} + 1\right)\right]^{\frac{1}{2}} \quad (1.35)$$

and the attenuation constant β is given by:

$$\beta = \omega \left[\frac{\mu\varepsilon}{2} \left(\sqrt{1 + \left(\frac{\sigma}{\varepsilon\omega} \right)^2} - 1 \right) \right]^{\frac{1}{2}}. \tag{1.36}$$

The skin depth δ *i*s defined as:

$$\delta = \frac{1}{\beta}. \tag{1.37}$$

The wavelength of the signal is:

$$\lambda = 2\pi\delta, \tag{1.38}$$

and the propagation velocity is given by:

$$v_P = \lambda f \tag{1.39}$$

where f is the frequency of the signal.

Angular frequency ω is related to linear frequency f by:

$$\omega = 2\pi f. \tag{1.40}$$

For a horizontal plane wave propagating downward along the z axis in a homogeneous earth, the solutions to wave equations (1.32) and (1.33) are:

$$\mathbf{E} = \mathbf{E}_0 \mathbf{e}^{-ikz} e^{i\omega t} = \mathbf{E}_0 e^{-i\alpha z} e^{-\beta z} e^{i\omega t} \tag{1.41}$$

$$\mathbf{H} = \mathbf{H}_0 e^{-ikz} e^{i\omega t} = \mathbf{H_0} e^{-i\alpha z} e^{-\beta z} e^{i\omega t} \tag{1.42}$$

$\mathbf{E_o}$ and $\mathbf{H_o}$ are the maximum electric and magnetic field strengths, respectively. In these equations, note that the amplitude decays in conductive media according to the attenuation constant β, while the phase reference of the fields depends upon the phase constant α.

Wave impedance is defined as the ratio of the orthogonal components of **E** and **H** fields:

$$\mathbf{Z} = \left| \frac{\mathbf{E}}{\mathbf{H}} \right| \tag{1.43}$$

It is useful to examine two extreme limits of the wave solutions: the quasi-static limit and the dielectric limit. We look first at the quasi-static

limit, which is of most interest to geophysical applications (in particular for mCSEM sounding).

Earth materials usually have resistivity $\rho < 10^4\ \Omega \cdot \mathrm{m}$ and permittivity $\varepsilon < 10^{-11}\ \mathrm{F/m}$. For frequencies below 100 kHz, $\sigma \gg \varepsilon\mu$, and $\varepsilon\mu$can be neglected, which is the quasi-static approximation. In this case we have $\alpha = \beta$ and the propagation constant simplifies to:

$$k = (1 - i)\sqrt{\frac{\mu\sigma\omega}{2}}. \tag{1.44}$$

For the horizontal electric field component $\mathbf{E_x}$, assuming implicitly a harmonic time dependency $e^{i\omega t}$, we have for a horizontal plane wave propagating downward along the *z* axis:

$$E_x = E_{0x}e^{-i\alpha z}e^{-\beta z} \tag{1.45}$$

Equation 1.45 can be rewritten using $\alpha = \beta$ as:

$$E_x = E_{0x}e^{-i\sqrt{\mu\omega\sigma/2}z}e^{-\sqrt{\mu\omega\sigma/2}z} \tag{1.46}$$

Considering equation 1.37, equation 1.46 can be rewritten as:

$$E_x = E_{0x}e^{-iz/\delta}e^{-z/\delta}. \tag{1.47}$$

At a depth equal to the skin depth ($z = \delta$), we obtain:

$$E_x = E_{0x}e^{-i}e^{-1}, \tag{1.48}$$

and the real part of the electric field is attenuated by $1/e$ (~63%of the original field strength). The magnetic field has an identical behavior. In the quasi-static approximation, equation 1.37 reduces to:

$$\delta = \sqrt{\frac{2}{\mu\sigma\omega}}. \tag{1.49}$$

Assuming $\mu = \mu_0 = 1.256 \times 10^{-6}\ \mathrm{H/m}$, and converting frequency in Hertz ($\omega = 2\pi f$), equation 1.49 can be written in terms of resistivity as:

$$\delta = 503\sqrt{\frac{\rho}{f}}\,\text{m}. \tag{1.50}$$

The skin depth is not a measure of resolution, but it is a guide to the maximum distance at which the EM energy can propagate.

The equivalent depth of investigation D of a plane wave can be derived from asymptotic relations based on a uniformly layered half-space (Bostick, 1977):

$$D = \frac{\delta}{\sqrt{2}} = 356\sqrt{\frac{\rho}{f}}\,\text{m}. \tag{1.51}$$

Note that penetration is dependent upon two parameters: the resistivity of the earth, and the frequency of the signal being used. Penetration is shallower with decreasing resistivities and increasing frequencies. Conversely, penetration is deeper with increasing resistivities and decreasing frequencies. By varying the signal frequency, continuous vertical soundings can be obtained.

The propagation velocity under quasi-static conditions is:

$$v_P = \sqrt{\frac{2\omega}{\mu\sigma}} = \delta\omega. \tag{1.52}$$

For the mCSEM range the propagation velocity is about of the same order of the skin depth δ.

material	σ S/m	1 day	1 hour	1 sec	1 ms
Seawater	3	85 km	17 km	290 m	9 m
Sediments	0.1	460 km	95 km	1.6 km	50 m
Igneous rock	10^{-5}	50000 km	9500 km	160 km	5 km

Table 1.1: *the skin depth is described as a function of the period T* ; $(T = 1/f)$.

Very resistive materials can behave like dielectrics. The case of a material appearing to be a dielectric medium occurs when displacement currents dominate conduction currents. In this case $\sigma \ll \varepsilon\omega$ and the propagation constant becomes:

$$k = \omega\sqrt{\mu\varepsilon}, \tag{1.53}$$

And the skin depth approaches infinity. The propagation velocity is then:

$$v_p = \frac{1}{\sqrt{\mu\varepsilon}}. \tag{1.54}$$

Dielectric effects can be observed in very resistive ground and at very high signal frequencies, but not generally at the low frequencies used in mCSEM. Hence the quasi-static approximation is good for nearly all earth materials.

In EM methods there are several mechanisms producing changes in amplitude and phase (Figure 1.1). The first is the geometric spreading from the transmitter, which in the low-frequency limit is simply the characteristic $1/(range)^3$ dipole decay that is familiar to users of DC resistivity sounding. The second is the galvanic effect associated with current flowing across a conductivity boundary. The normal component of current must be continuous (from conservation of charge), and so Ohm's law ($\mathbf{J}=\sigma\mathbf{E}$, where $\mathbf{J}$ is current density) requires a jump in the electric field. Again, this is the low-frequency behavior, characteristic of DC resistivity sounding, and, like the geometric effects, has no associated changes in phase. Finally, the process of inductive attenuation and phase shift occurs when the skin depths are comparable to the distance over which the EM energy has traveled (Constable 2010).

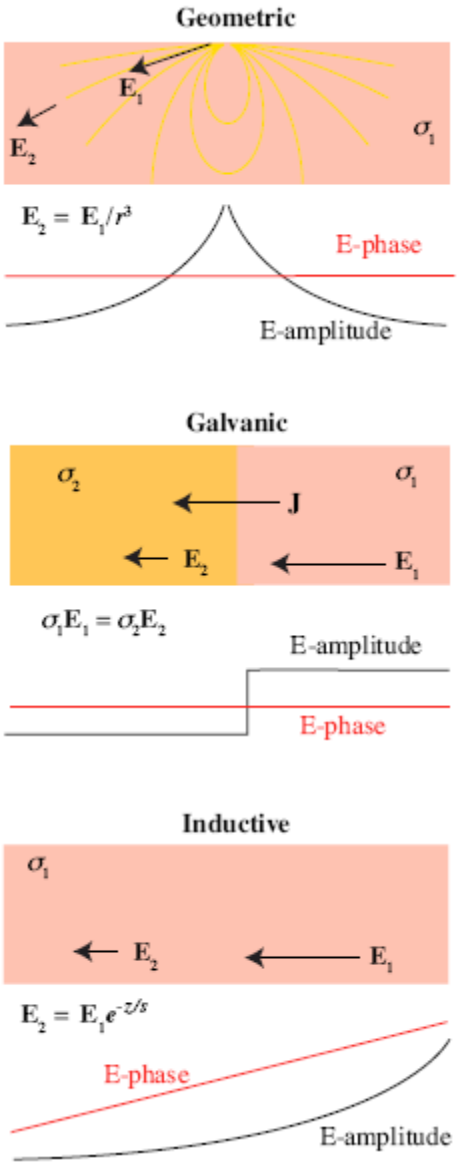

Figure 1.1: *from Constable (2010); three mechanisms are at work determining the amplitude and phase of CSEM signals as a function of source–receiver offset. The first is simple geometric spreading from a dipole, the second is a galvanic change in the electric field as current crosses a conductivity boundary, and the third is inductive attenuation. Only induction produces a change in phase.*

1.4 The story of the mCSEM method

The use of electromagnetic methods in hydrocarbon exploration began in the early twentieth century (e.g., Rust, 1938) and, on land, continues to this day, mainly through MT surveys carried out to provide structural constraints. Marine electrical methods started with DC resistivity surveys

carried out over water within only a few years of the method's inception (Schlumberger et al., 1934; Constable, 2007).

However, because these are all shallow water systems and the market for offshore mineral mining is small, these methods were (Constable, 2007).

1.4.1 The development of "Controlled Source Electromagnetic" methods.

The first to develop the method as we know today was Cox of Scripps Institution of Oceanography in the late 1970s (Cox, 1981). He performed the first experiment in 1979 on a mid-ocean ridge in the Pacific (Young and Cox, 1981). The original motivation for his CSEM experiments was to study the shallow and resistive parts of the oceanic lithosphere by replacing the relatively high frequency energy lost to magnetotelluric fields with a deep-towed man-made transmitter (Constable, 2007).

Early funding for instrument development came from the U. S. Defense Advanced Research Projects Agency (DARPA), which was interested in the effect of the seafloor on submarine communications. Support also came from the U. S. Office of Naval Research (ONR), which wanted to learn more about the seafloor noise environment (Constable, 2007). Martin Sinha of Cambridge University started to develop a CSEM system in the '80s (Sinha et al. 1990). He and his group introduced an antenna that could be towed to a distance of about 100 m above the seafloor and so they could work on very complex morphologies.

"Collection of data sets cannot proceed far without supporting theory and numerical modeling algorithms" (Constable, 2007). So, first studies, based on the asymptotic solutions, were carried on by Kraichman (1970) and Bannister (1968, 1984) (Constable, 2007). Then, numerical finite-element solutions to the 2D electric dipole problem were developed for the time-domain by Everett and Edwards (1993) and for the frequency domain by Unsworth et al. (1993); Constable (2007). The first 2D inversion of real data was published by MacGregor et al. (2001), who modified the Unsworth forward code (1995) to handle experimental geometries and bathymetry and implemented the OCCAM inversion algorithm (Constable, 2007). A finite-element forward code for CSEM

was written by Li and Key (2007) and has been broadly distributed. A 2D finite-difference forward and inverse code was published by Abubakar et al. (2008), but this code is proprietary. Other 1D, 2D, and 3D codes have been written and are being used on a proprietary basis also (Constable, 2010).

Proprietary restrictions on access make it difficult to validate and compare codes, and the author has seen examples of very different results being obtained from the same data set by different contractors using different inversion codes (Constable, 2010).

1.4.2 The marine CSEM development in the oil and gas industry.

ExxonMobil started to study marine EM methods in early '80s, but only in the '90s the oil companies started to use this methodology routinely.

In November 1999, Steven Constable was invited to review Statoil's internal research project, which consisted of a variety of numerical and analog modeling. The conclusion was that if the target is not too small compared with its depth of burial, and the water depth is sufficient to suppress the air wave, then the controlled source signature of the oil-filled layer is detectable, yielding controlled source amplitudes that are a factor of 2 to 10 different than models without the oil layer (Constable, 2007). So, in 2000 Statoil started a test in the Angola off-shore and ExxonMobil started a test in the Scotland off-shore and West Africa off-shore.

Today EM methods are very attractive for oil companies; in fact these methods are very useful as complementary to seismic and potential fields methods.

In the last years in Italy ENI showed his interest in this innovative technology developing new inversion and interpretation techniques for data acquired in shallow depth water.

1.5 Marine CSEM concepts

In this paragraph we are going to show the physics of mCSEM method, basing mostly on the paper by Chave et al. (1991).

There are numerous approaches to the theory of EM induction in conducting media by finite or distant sources; see Ward and Hohmann, VoI. 1 (1988) for a review. Here, following Chave et al. (1991), we use the modal form of the induction equations for one-dimensional (l-D) media.

The EM fields for an l-D conductivity structure may be separated into independent toroidal and poloidal magnetic (TM and PM) modes about the vertical axis. The TM modes are associated with electric currents flowing in loops containing the vertical, and possess no vertical magnetic field component, while PM modes are driven by electric current systems which are always horizontal, and have no vertical electric field component. Because of this distinction, the sensitivity of the two modes to electrical structure is quite different. This difference can be demonstrated considering a horizontal insulating layer buried in a half-space, and deducing the behavior of vertical and horizontal currents in its presence. Due to the existence of vertical electric currents and consequent galvanic interactions, TM modes are strongly affected by relatively low conductivity zones, being unable to penetrate them very effectively, while the PM mode is quite insensitive to such regions due to its entirely inductive nature. Both modes are influenced by relatively high conductivity material. A summary of mode theory appears in the Appendix 1, including Green functions, which account for seafloor and sea-surface boundary effects explicitly, and will be referred to as needed.

As we said before, controlled source EM methods utilize time-varying electric and magnetic dipole sources of known geometry to induce electric currents inside the conducting earth. The electric or magnetic signature of the currents can be detected and can yield a measure of the electrical conductivity of the underlying rock. The four fundamental source/receiver types for controlled source work are the vertical and horizontal electric dipoles (VED and HED) and the vertical and horizontal magnetic dipoles (VMD and HMD), and there are many practical combinations of them.

Unlike what happens in CSAMT, in Marine controlled source problems both source and receiver are always immersed in a conductive medium

and this has to be in account when we consider the induction problem. Furthermore, some system geometries require the explicit inclusion of the ocean-atmosphere boundary in the theory (Chave et al, 1991).

TM and PM modes can be associated with the four basic types of sources: (1) the vertical electric dipole (VED), which generates only TM modes, (2) the vertical magnetic dipole (VMD), which induces only PM modes, and (3) the horizontal electric dipole (HED) and (4) horizontal magnetic dipole (HMD), which are more general, and can produce both modes. An EM exploration system is made up of some source-receiver combination. Generally, symmetric systems in which the source and receiver are of the same type are commonly used. In our notation, when HED, VMD, and HMD refer to systems, they are the collinear horizontal electric dipole-dipole, coplanar vertical magnetic dipole-dipole, and coaxial horizontal magnetic dipole-dipole combinations. In particular, when these systems are not immersed in a conductive medium, the VMD and HMD systems detect only horizontal current (PM modes) in an l-D earth, hence are relatively insensitive to thin resistive zones instead, HED system combines TM and PM modes and it is preferred when resistive zones have to be mapped. But, when these systems are deployed on the seafloor the behavior is different. In fact, in this case source and receivers are now buried inside a conductive medium rather than lying on a conductive half-space, and preconceptions based on their terrestrial use can be quite misleading. The VMD system still is based only on a PM mode, but the HED and HMD systems generate and receive both PM and TM modes. Furthermore, the secondary EM fields due to induction in the crustal material are measured near the interface of a good conductor (seawater), so a system like the VMD, in which a component of a field vanishing at the surface of a good conductor is measured, is unlikely to display sensitivity to a resistive seafloor. This is not true for the HED and HMD systems, which are both quite capable of accurately measuring the conductivity of the seafloor in the common instance where seawater is more conductive than rock. The less common circumstance of a relatively conductive seafloor is analogous to the terrestrial case, and systems like the VMD type are then sensitive to seafloor conductivity.

The choice of operating an EM system in either the frequency domain, transmitting a set of discrete frequencies one or a few at a time, or in the time domain, transmitting a square or triangular step and measuring the transient response of the seafloor-ocean system, also exists. The physics of the two methods are identical, the response in one domain being the Fourier transform of the response in the other domain. Because of the finite and inexact nature of practical measurements, this transformation cannot usually be made outside the realm of theoretical studies. The choice of one system over another must be made on the basis of practical and logistical considerations.

Chave and Cox (1982) developed the theory for the frequency domain HED method using the modal formulation given in the Appendix 1, and some details will be summarized to illustrate the behavior of CSEM method in the frequency domain. In particular, here we consider only the electric field. Using the Green functions from equations (A1.14) and (A1.15), taking the limit of an infinitely deep ocean ($H \to \infty$), and utilizing the cylindrical symmetry to convert from a Fourier to a Hankel transform, the radial, azimuthal, and vertical electric fields generated by an horizontal electric dipole for an uniform sea layer above an uniform layered earth may be written as:

$$E_\rho = \frac{p}{4\pi\sigma_0}\cos\phi \int_0^{\infty x} dk \left\{ J_0(kr)k\beta R_L^{PM} - \frac{1}{\rho}J_1(kr) \times \left[\beta R_L^{TM} + \frac{\gamma_0^2}{\beta} R_L^{PM}\right]\right\} e^{-\beta(z+z')} - \frac{p}{4\pi\sigma_0}\cos\phi \int_0^{x} dk \left\{ J_0(kr)k\beta - \frac{1}{\rho}J_1(kr)\frac{k^2}{\beta}\right\} e^{-\beta|z-z'|} \tag{1.55}$$

$$E_\rho = \frac{p}{4\pi\sigma_0}\sin\phi \int_0^\infty dk \times \left\{ J_0(kr)\gamma_0^2 \frac{k}{\beta} R_L^{TM} - \frac{1}{\rho} J_1(kr) \left[\beta R_L^{TM} + \frac{\gamma_0^2}{\beta} R_L^{PM} \right] \right\} e^{-\beta(z+z')} + \frac{p}{4\pi\sigma_0}\sin\phi \int_0^x dk \times \left\{ J_0(kr)\gamma_0^2 \frac{k}{\beta} + \frac{1}{r} J_1(kr) \frac{k^2}{\beta} \right\} e^{-\beta|z-z'|}$$

(1.56)

$$E_z = -\frac{p}{4\pi\sigma_0}\cos\phi \int_0^\infty dk J_1(kr)k^2 \times \left[R_L^{TM} e^{-\beta(z+z')} \pm e^{-\beta|z-z'|} \right]$$

(1.57)

Where p is the source dipole moment in Am, ϕ is the azimuthal angle measured with respect to the source, r is the horizontal range, z and z' are the receiver and source heights, R_L^{TM} and R_L^{PM} are the seafloor modal reflection coefficients given by equation (A1.16), β is given by equation (A1.17), γ_0 is the induction parameter or propagation constant in the sea-water, characterized by a conductivity σ_0, for the quasi-static case (from equation 1.44):

$$\gamma_0 = \sqrt{i\omega\mu_0\sigma_0} \tag{1.58}$$

and k is the horizontal wave-number.

The lower sign in equation (1.57) holds for $z > z'$ and vice versa. The first terms in equations (1.55)-(1 .57) represent propagation in the underlying rock and along the sea-rock interface, while the second terms, which can be evaluated in closed form, represent the propagation in the

ocean. The electrical conductivity structure beneath the seafloor enters the problem only through the reflection coefficients R_L^{TM} and R_L^{PM}, and equations (1.55)-(1.57) are wavenumber expansions of the fields.

Following Chave et al. 1991 we can obtain an approximate analytic solution modeling the seafloor as a half-space of conductivity σ_1 and obtain approximate analytic solutions to equations (1.55)-(1.57) for $\sigma_1 \ll \sigma_0$. The reflection coefficients, equation (A1.16), are expanded in powers of σ_1/σ_0, and only the lowest order terms are retained. Considering that source and receiver occupy the interface ($z = z' = 0$) and evaluating the Sommerfeld type integrals we have that the horizontal components of the electric field are:

$$E_\rho \approx \frac{p}{2\pi\sigma_0}\cos\phi\left[\frac{(\gamma_0\rho+1)}{r^3}e^{-\gamma_0 r} + \frac{(\gamma_1^2\rho^2+\gamma_1\rho+1)}{r^3}e^{-\gamma_1 r}\right] \tag{1.59}$$

$$E_\phi \approx \frac{p}{2\pi\sigma_0}\sin\phi\left[\frac{(\gamma_0\rho+1)}{r^3}e^{-\gamma_0 r} + \frac{2(\gamma_1\rho+1)}{r^3}e^{-\gamma_1 r}\right] \tag{1.60}$$

where γ_1 is the propagation constant, described by equation 1.58, in the quasi-static case when the conductivity of the rocks is σ_1. To get an expression for the vertical electric field, an additional approximation discussed in Cheesman et al. (1987) and valid at ranges comparable to or larger than a skin depth in the lower medium must be invoked, yields:

$$E_z \approx \frac{p}{2\pi\sigma_0}\cos\phi\,\frac{\sigma_1}{\sigma_0}\frac{\gamma_0(\gamma_1\rho+1)}{r^2}e^{-\gamma_1 r} \tag{1.61}$$

The first terms in equations (1.59) and (1.60) correspond to a disturbance propagating in the ocean and along the seafloor, and vanish rapidly for $r \gg |\gamma_0|^{-1}$. At a 1 Hz frequency, the seawater skin depth is 210 m, and the oceanic component is negligible beyond about 1 km. Instead, the second terms correspond to a similar disturbance below and along the seafloor, and attenuate much more slowly with range, dominating the solution when $r \gg |\gamma_0|^{-1}$. For ranges $r \approx |\gamma_1|^{-1}$, the field decays

slowly (as r^{-1} to r^{-3}), while at larger ranges the exponential term controls the attenuation.

Figure 1.2 shows the radial and vertical electric fields, obtained by integrating equations (1.55) and (l.56) numerically, as a function of source-receiver separation at a frequency of l Hz and for an ocean half-space of conductivity 3.2 S/m overlying rock half-spaces of conductivity 0.05 and 0.005 S/m. The behavior of the azimuthal electric field is similar to that of the radial part except for the different angular dependence seen in equations (1.55) and (l.56). The skin depths in the sea water, as stated before, is 210 m, whereas the skin depth in the more resistive rocks are 2.3 km and 1.1 km respectively for the half-space conductivity of 0.05 S/m and 0.005 S/m.

At off-set (source - receiver distance, r) less than a skin depth in the half-space "near field zone", the source looks like a quasi-static dipole and the horizontal electric field attenuation is largely controlled by the conductivity of the ocean, instead for values of the offset equal to one skin depth, the effect of the lower half-space becomes noticeable, but the conductivity dependence of the field is weak and the attenuation is not sharp. At offset higher than skin-depth, the attenuation becomes exponential as in equations (1.59) and (1.60), so that, as shown in Figure 1.2, the differences between the two models increase as the offset grows. By contrast, the vertical electric field, dotted lines in Figure 1.2, is sensitive to the lower medium conductivity in the quasi-static limit, as seen in equation (1.61), and a smaller rock conductivity results in weaker fields. At even larger ranges, propagation effects yield more rapid attenuation as the seafloor conductivity increases.

From Figure 1.2 we can see that the vertical electric field is always substantially smaller than the horizontal electric field components when the ocean conductivity is higher than the half-space conductivity, but it is sensitive to the conductivity of the half-space at smaller ranges.

Figure 1.2 also shows the radial electric field as a function of frequency for several ranges and a lower half-space of conductivity 0.05 S/m. At frequencies corresponding to skin depths larger than offsets, the behavior

is that of a static dipole, with only small attenuation as the frequency increases. The attenuation and attenuation rate increase at frequencies corresponding to skin depths smaller than the offset. The phase of the electric field (not shown) behaves similarly. Similar relationships exist for the magnetic field components; see Chave and Cox (1982) for details.

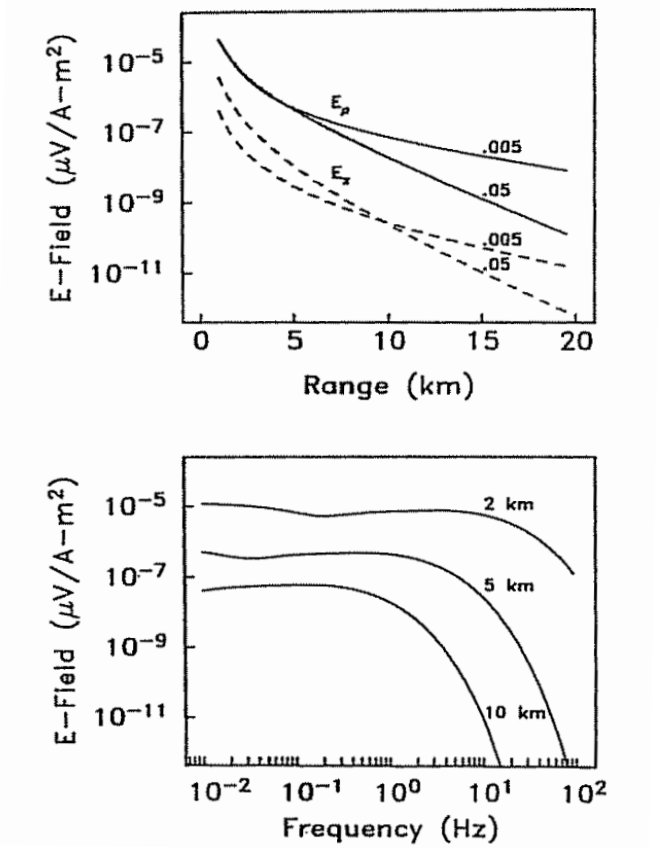

Figure 1.2: *from Chave et al. (1991); the upper panel shows the radial and vertical electric fields per unit of source dipole moment as a function of range at a frequency of l Hz and for lower half-spaces of conductivity 0.05 and 0.005 S/m. The lower pane l shows the radial electric field as a function of frequency at ranges of 2.5 and 10 km for a lower half-space of conductivity 0.05 S/m. The ocean conductivity is taken as 3.2 S/m, and the radial electric field is measured off of the end of the source.*

It is important to examine the behavior of the horizontal electric field for geometric (range-dependent) and parametric (frequency-dependent) soundings in the presence of the simplest structural complication, a buried layer. So, is considered a specific model consisting of a l km thick resistive layer buried in a half-space of conductivity 0.05 S/m. The resistive layer was considered first at a depth of 1.5 km and then at a depth of 5.5 km. Figure 1.3 shows the geometric sounding curves. “The

low conductivity zone behaves as a lossy waveguide, which traps and guides the signal, resulting in slower attenuation with range when compared to the half-space case" (Chave et al. 1991). Conversely, if the buried layer has a higher conductivity than the surrounding material, we will expect a higher attenuation at long ranges, *r*, but we will have an increase in signal strength at intermediate distances due to the low conductivity waveguide created between the seafloor and the layer.

The HED system is preferentially sensitive to relatively low conductivity zones due to the presence of the TM mode.

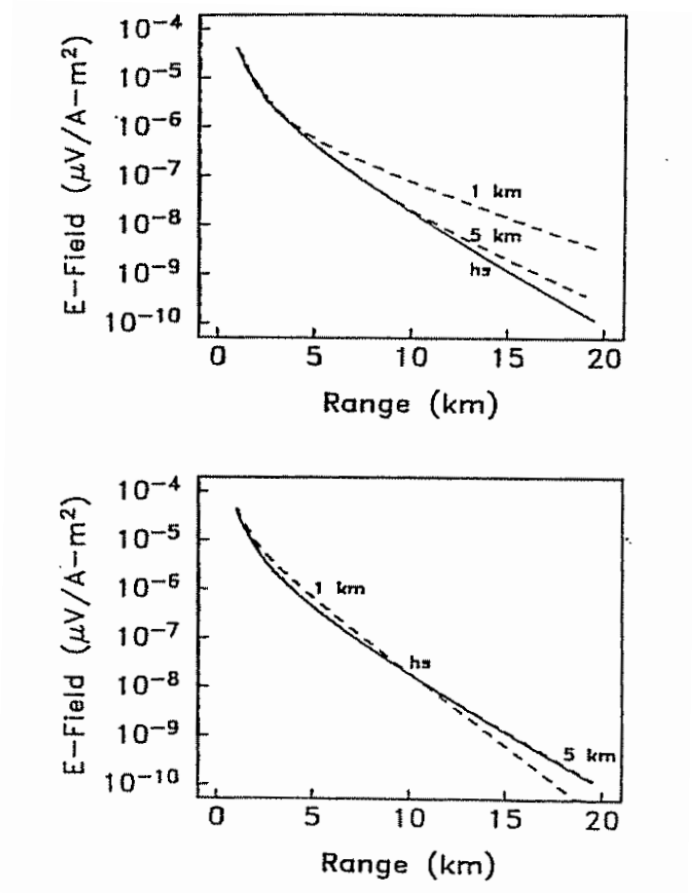

Figure 1.3: *from Chave et al. (1991);the radial electric field as a function of range at a frequency of l Hz for an ocean half-space of conductivity 3.2 S/m and a lower half-space of conductivity 0.05 S/m containing l km thick layers at 1 and 5 km depth. In the upper panel the layers have a low relative conductivity of 0.005 S/m, while in the lower panel the conductivity of the layer is high (0.5 S/m).*

The equations 1.56 and 1.57 given by Chave and Cox (1982), using a Green's function technique, represent the expression of the electric field of an HED in deep water. Andréis and MacGregor (2008) have extended

this work evaluating the analytic expression of the electric field in the general case of an HED in a finite sea-water layer. These equations and the relative considerations are shown in Appendix 2. As shown in Appendix 2 the HED transmitter excites energy throughout the seafloor-seawater-atmosphere system. As said before, the fields decay both geometrically and exponentially with a characteristic *e*-folding distance given by the skin depth so, the tendency is that, for a given offset (*r*), the propagation through one part of the system will dominate the received fields (Constable, 2007). This effect is illustrated in Figure 1.4, where the amplitude and phase curves are shown versus the source-receiver offset for the *canonical oilfield model*. The *canonical oil field model* is a 1D model characterized by a 100 Ωm reservoir 100 m thick, buried at a depth of 1000m, in host sediment having a resistivity of 1 Ωm. The thickness of the water column is 1000 m.

The results of this experiment are shown in Constable (2007).

In order to highlight all the dominant propagation paths in one figure, a 10 Hz transmission frequency was taken and made the calculations through the use of the 1D code of Flosadottir and Constable (1996).

The solid lines in Figure 1.4 represent, respectively, the amplitude and the phase of the radial component of the electric field, that is the component of the field in direction of the axis of the transmitter; the dotted lines represent, respectively, the amplitude and the phase of the azimuthal component of the radiated electric field, that is the component of the field orthogonal to the transmitter axis.

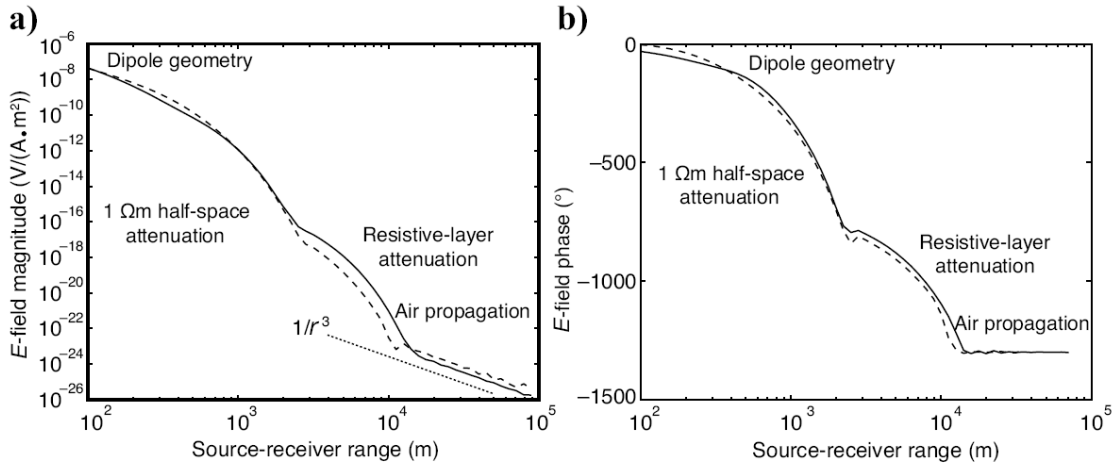

Figure 1.4: *from Constable et al. (2007);radial (solid lines) and azimuthal (dashed lines) amplitude and phase responses over the canonical model for a frequency of 10 Hz and a transmitter altitude of 30 m.*

As we can see from Figure 1.4, close to the transmitter we see the $1/r^3$ amplitude fall-off from a static dipole and nearly constant phase. The r^3 dipole dependence can be seen in equations 1.59 and 1.60 considering the terms associated with exponential attenuation through the water (first term, in γ_0) and through the seafloor rocks (the second term, in γ_1). At ranges between a few hundred meters and 2 km, skin depth in the seafloor sediment (158 m) is larger than in seawater, and we see exponential attenuation dominated by the seafloor resistivity. Up to this point, the mathematics of propagation is reasonably approximated by the double half-space (i.e., infinite water depth and no reservoir layer) solution of Chave et al. (1991) and described by equations 1.59 and 1.60. The dipole azimuth ϕ in equations 1.59 and 1.60 is 0° for the purely radial mode shown in Figure 1.4 and 90° for the purely azimuthal mode. At ranges between 2 and 10 km, can be noted an increasing in the electric-field amplitudes (relative to those that would be measured in the absence of a resistive layer) that is associated with a larger skin depth (1600 m) in the more resistive reservoir layer. This increasing can be seen also considering the phase of the radial and azimuthal components of the electric (Figure 1.4). Then, at off-sets, r, greater than 10 km, propagation through the atmosphere dominates the receiver fields and the amplitude returns to an $1/r^3$ dipole and the phase that become

constant (i.e., the apparent phase velocity is now comparable to the speed of light).

From Figure 1.4 we see that the azimuthal and radial modes have a similar behavior, this because we considered a 10 Hz frequency and then the inductive effects in the reservoir layer produce a significant response also in the azimuthal mode. Instead, at lower frequencies, the CSEM fields are dominated by the galvanic effect generated by the vertical electric fields of the radial mode (that are almost absent in the azimuthal mode) and so the behavior of radial and azimuthal modes are quite different (Constable, 2007).

1.6 Propagation through the atmosphere

In mCSEM sounding the signal coming from the seabed can be masked by the components of the field that have been refracted and reflected off the sea surface.

We call *airwave* the signal component that propagates upward from the source to the sea surface, horizontally through the air with no attenuation, and back down through the water column to the receiver (Admunsen et al., 2006).

From equation 14 of Bannister (1984) and as reported in Constable and Weiss (2006) a good approximation of the amplitude of the radial mode air-wave is given by:

$$E_{AIR} = \frac{e^{-2h/\delta}}{2\pi\sigma r^3} \tag{1.62}$$

where h is the water-depth, $\delta = \sqrt{2/\sigma\omega\mu_0}$ is the skin depth in seawater of conductivity σ and magnetic permeability μ_0 at angular frequency ω, and r is the source-receiver range.

As we can see from equation 1.62, the behavior of the airwave component is independent of the sea-floor resistivity. “Moreover, this equation could be thought of as skin-depth attenuation up ($e^{-h/\delta}$) and down ($e^{-h/\delta}$) through the water column, coupled with the $1/r^3$ geometric spreading associated with a dipole” (Constable and Weiss, 2006).

Taking from Constable and Weiss 2006, in Figure 1.5 we show separately the contributions to the horizontal electric-field magnitude from the seafloor and the atmosphere for various water depths and seafloor resistivity. Although, the propagation through the atmosphere is given only by the $1/r^3$ geometric spreading, the amplitude of the airwave depends on the water depth and in particular decreases as the water gets deeper. As we seen in the previous paragraph, at short ranges the amplitude of the electric field propagating through the seafloor and seawater is similarly given by the $1/r^3$ dipole decay, but at ranges greater than skin depth exponential attenuation in the seafloor rocks dominates the curves (Constable and Weiss, 2006). In particular, "a more resistive seafloor with larger skin depth supports large electric fields to greater source–receiver ranges. It can thus be seen that as the seafloor gets more resistive and the seawater gets deeper, the seafloor signal dominates the atmosphere signal to longer ranges" (Constable and Weiss, 2006). At the range at which the curves cross for a given water depth and seafloor resistivity, the airwave starts to dominate the signal observed on the seafloor. Thus, the curves for a 1 Ωm seafloor and 900 m water-depth cross at a range of 4500 m. Various schemes have been proposed to separate the airwave from the seafloor signal in the vicinity of the crossover (e.g., Admunsen et al. 2006), but as said by Constable and Weiss (2006) the simplest thing to do is just to include the air layer in the modeling and interpretation.

As we can see from Figure 1.5 and as we said before, the problem of the air-wave is more sever in shallow water survey, but in this case the situation is more similar to a land survey than a deep ocean sounding, so in this case in better to work in the time domain rather than in frequency domain as Wright et al. (2001) did for mapping a gas reservoir in France (Constable and Weiss, 2006).

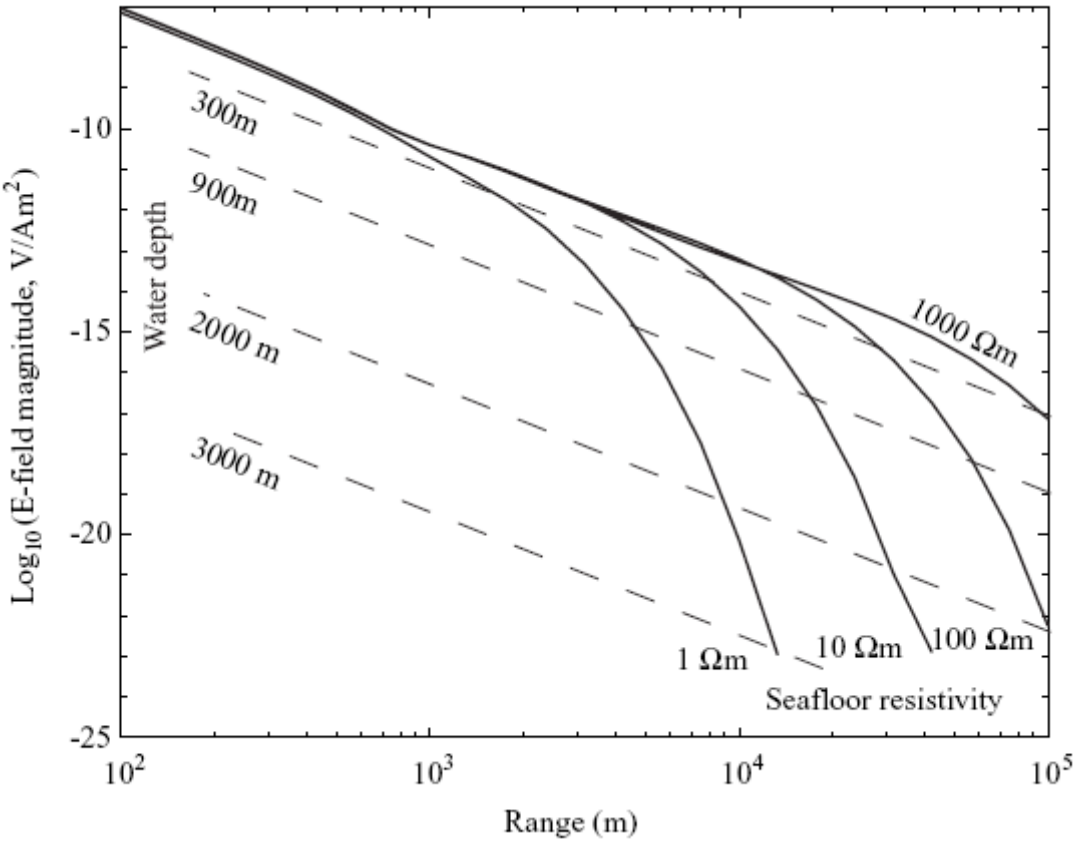

Figure 1.6: *from Constable and Weiss (2006); seafloor 1 Hz CSEM horizontal radial electric-field amplitudes as a function of range and half-space resistivity (solid lines) in the absence of an air layer and the contribution of the electric field that has propagated through the atmosphere (broken lines) for various water depths between 300 m and 3000 m.*

1.7 Anisotropy

"While the assumption of isotropy can prove successful in certain cases, sediment formations are often observed to be electrically anisotropic at several scales" (Ramananjaona et al., 2010). At the grain scale, anisotropy can be caused by mineral alignment, most often due to compaction, for example in shale (Clavaud, 2008). In this case the anisotropy resulting from mineral alignment would be called *micro-anisotropy*. Layering of thin horizontal strata can also create a *macro-anisotropy* effect on electrical measurements (Maillet, 1947). So, we can consider a stack of layers characterized by different resistivities as a vertically anisotropic medium.

In a Cartesian coordinate system where z is pointing upward, the uniaxial anisotropy of a stratified earth is described by the conductivity tensor:

$$\bar{\bar{\sigma}} = \begin{bmatrix} \sigma_h & 0 & 0 \\ 0 & \sigma_h & 0 \\ 0 & 0 & \sigma_v \end{bmatrix} \tag{1.63}$$

Where σ_h and σ_v are respectively the horizontal and the vertical conductivities of the medium (and $\rho_h$and ρ_v their corresponding resistivities).

Moreover, we can define an anisotropy ratio λ as:

$$\lambda = \sqrt{\frac{\sigma_h}{\sigma_v}} = \sqrt{\frac{\rho_v}{\rho_h}}\,. \tag{1.64}$$

The presence of anisotropic structure within the earth can significantly modify the signature observed in the electromagnetic field measured at the sea-bottom. “The degree to which the responses are affected depends strongly on the geometry between the source and the receiver, the resistivity structure of the earth beneath them and the frequency of the transmitted signal” (Ramananjaona et al., 2010).

We have seen in the previous paragraphs that, when the earth is approximated as a one dimensional layered structure, the electromagnetic field can be described by two modes; the toroidal magnetic (TM) and the poloidal magnetic (PM). In particular we have seen also that the PM mode is very insensitive to the horizontal resistivity structure and in particular is very insensitive to thin resistive layer because of its inductive nature, conversely the TM mode is very sensitive to the presence of thin resistive layer such as oil or gas reservoirs. Moreover, we have already said that the in-line component of the electric field (ϕ=0° in equation 1.59) is dominated by TM mode, instead the broad-side component of the electric field (ϕ=90° in equation 1.60) is dominated by TE mode. Therefore, we can say that in-line measurements of the radial electric field will have sensitivity to the anisotropy ratio and the vertical resistivity, whereas broadside measurements of the azimuthal electric field will have more sensitivity to the horizontal resistivity.

While in the case of DC electric field measurements, there exists an equivalent isotropic model for every layer of anisotropic conductivity (σ_h, σ_v) and thickness H, characterized by an average conductivity $\sigma = \sqrt{\sigma_h \sigma_v}$ and a thickness λH, as noted by Mallet (1947), in the non-static case the effects of induction do not allow the derivation of such a simple equivalence relation, although a similar response can be found between isotropic and anisotropic models (Ramananjaona et al., 2010).

As we said in Paragraph 1.5, the information about the resistivity structure in which the field diffuses are expressed by the reflection coefficients R. In particular, Ramananjaona et al. (2010) have shown that, an anisotropic layer of resistivity (ρ_h, ρ_v) and thickness H has an equivalent isotropic layer for each mode (Brown et al., 2012). This can be seen considering the reflection coefficients $R^{TM}_{l-1\to l}$ and $R^{PM}_{l-1\to l}$ (equations A2.6 and A2.7), in the layer l-1 on the interface with layer l underneath, for the anisotropic case:

$$R^{TM}_{l-1\to l} = \frac{\frac{\beta_{1,l-1}\sigma_{h,1} - \sigma_{h,l-1}\beta_{1,l}}{\beta_{1,l-1}\sigma_{h,1} + \sigma_{h,l-1}\beta_{1,l}} + R^{TM}_{l\to l+1} e^{-2\beta_{1,l}H_l}}{1 + R^{TM}_{l\to l+1} \frac{\beta_{1,l-1}\sigma_{h,1} - \sigma_{h,l-1}\beta_{1,l}}{\beta_{1,l-1}\sigma_{h,1} + \sigma_{h,l-1}\beta_{1,l}} e^{-2\beta_{1,l}H_l}} \tag{1.65}$$

$$R^{PM}_{l-1\to l} = \frac{\frac{\beta_{2,l-1} - \beta_{2,l}}{\beta_{2,l-1} + \beta_{2,l}} + R^{PM}_{l\to l+1} e^{-2\beta_{2,l}H_l}}{1 + R^{PM}_{l\to l+1} \frac{\beta_{2,l-1} - \beta_{2,l}}{\beta_{2,l-1} + \beta_{2,l}} e^{-2\beta_{2,l}H_l}} \tag{1.66}$$

where β_1 and β_2 corresponds to the complex wave-number respectively for TM and PM mode and, as reported in (Ramananjaona et al., 2010), given by:

$$\beta_1 = \sqrt{\lambda^2 k^2 - i\omega\mu_0\sigma_h} = \lambda\sqrt{k^2 - i\omega\mu_0\sigma_v} \tag{1.67}$$

$$\beta_2 = \sqrt{k^2 - i\omega\mu_0\sigma_h} \tag{1.68}$$

where k is the horizontal wave-number: $k^2 = k_x^2 + k_y^2$.

In fact, from equations 1.65 and 1.66 we observe that the variation of the reflection coefficients of each mode with respect to conductivity depends only on the associated complex wavenumber, . Moreover, combining these equations with equations (1.67) and (1.68) we have that an equivalent or nearly equivalent isotropic layer for an anisotropic layer of

conductivity (σ_h, σ_v) and thickness H would have a conductivity σ_v and thickness λH in the TM mode and resistivity σ_h and thickness H in the PM mode (Ramananjaona et al., 2010). Hence, for the TM mode we don't have a complete equivalence between the isotropic and the anisotropic model because the thickness of the equivalent isotropic layer would be λH, where λ is the anisotropy ratio (equation 1.64). So, sometimes isotropic modeling can be insufficient for very anisotropic structures.
What has just demonstrated mathematically now will be shown considering the synthetic signals obtained using the DIPOLE 1D code of Key (2009), publicly available at:
http://marineemlab.ucsd.edu/Projects/Occam/1DCSEM/index.html
and already published in Constable (2010).

To demonstrate the importance of the anisotropy effect we now consider the signals obtained starting from two 1D isotropic models characterized by a 1Ω m and 0.51 Ωm sea-floor respectively and a third model characterized by an anisotropic sea-floor composed by alternating 50 m tick layers of 1.7 Ωm and 0.3 Ωm, producing a vertical resistivity equal to that of the first isotropic model and a horizontal resistivity equal to that of the first isotropic model.

In particular, in Figure 1.6 are shown the amplitudes of the radial and azimuthal components of the horizontal and vertical component of the electric field versus the distances antenna-receiver (offset), together with the horizontal component of the induced magnetic field (B) produced starting from the models described above. In particular only positive offsets are considered. The source signals are generated by an HED, with the fundamental frequencies of 0.25 Hz and 1 Hz.

As we can see from Figures 1.6a and c, the anisotropic model for radial fields produces almost identical responses to the 1Ωm model (i.e., the vertical resistivity) for all three components. Instead, for the azimuthal fields, the anisotropic model produces a horizontal electric field and vertical magnetic field that are almost identical to the 0.51 Ωm horizontal resistivity. The horizontal magnetic field in the azimuthal direction is the only component that does not behave simply, but this

component is going through a phase reversal associated with the interaction of the airwave with the seafloor fields (Constable, 2010). Hence, inverting only the radial component of the electric field measured along a profile is possible, but we will have as result the imaging of the vertical resistivity. Instead if we want to consider also the azimuthal component of the field, for example in 3D inversion, we have to consider also the anisotropy.

However, sometimes we can't ignore anisotropy also when we are interpreting only the radial mode; in fact, small differences between anisotropic and isotropic radial fields could not be neglected when we invert multi-component and/or multi-frequency data. For example, the horizontal electric field in the range between 2 and 5 km at 1 Hz (Figures 1.6 c and d) is within about 2% of the anisotropic response, whereas at the frequency of 0.25 Hz (Figures 1.6 a and b) the responses are from 10% to 20% different. The phase differences are about 10° at both frequencies, consistent with the 15% amplitude difference (Constable, 2010).

"In the practice, navigation errors probably limit the accuracy of typical CSEM data to about 10%, so the effects we discuss above might not be significant, but as we collect better quality data, anisotropy effects behave in this way." (Constable, 2010)

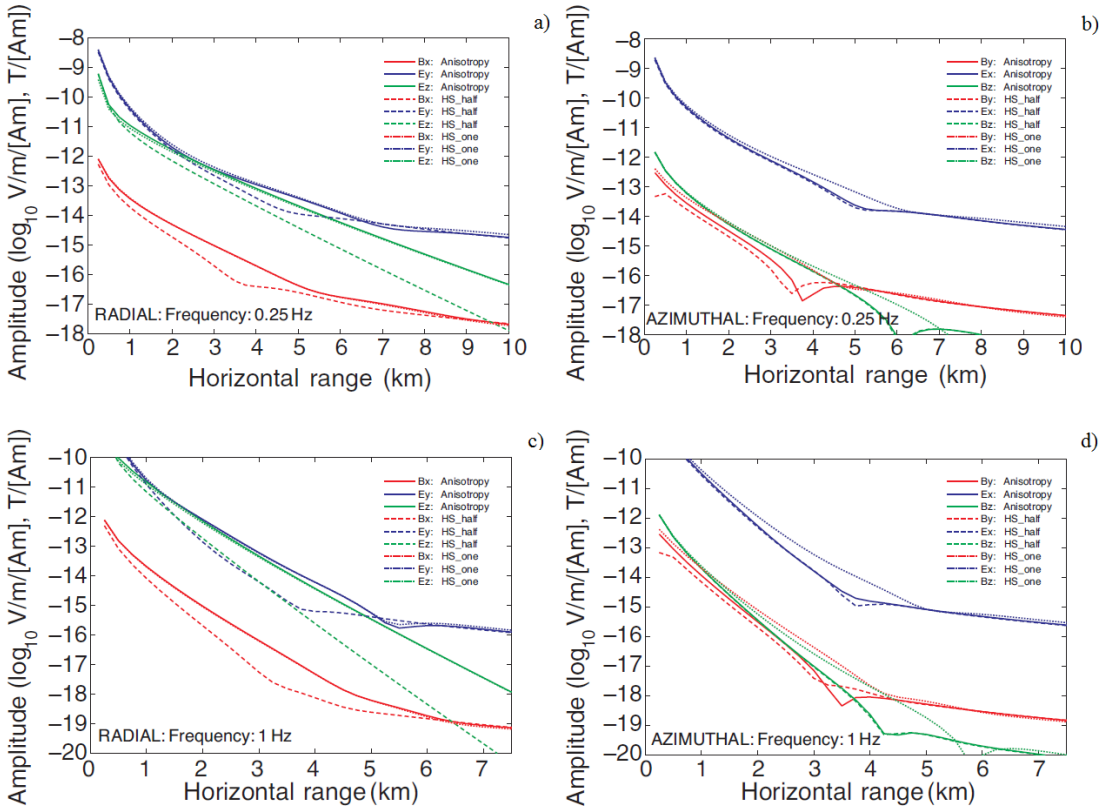

Figure 1.6: *from Constable (2010); Radial (left panels) and azimuthal (right panels) electric (blue) and magnetic (red) field amplitudes as a function of source–receiver distance over a half-space in 1000 m water depth (radial Ez and azimuthal Bz are both shown in green). Three half-space (HS) resistivities are considered, 1 Ωm (dotted lines), 0.51 Ωm (broken lines), and an anisotropic half-space with 1 Ωm in the vertical direction and 0.51 Ωm in the two horizontal directions ("Anisotropy," solid lines). The top panels show responses at 0.25 Hz, and the bottom panels show 1 Hz fields.*

1.8 Equipment

A mCSEM survey is carried out using a long, insulated seafloor transmitting antenna with bared ends, that is energized at frequencies near 1Hz, and a series of magnetic and electric receivers deployed on the sea-floor.

In particular, the antenna is an horizontal electric dipole (HED) and the length is between 100- 300 m.

As we showed in the previous paragraphs, the advantage to use a HED is that the system is sensitive to both low and high conductivity material in different ways due to the presence of both TM and PM modes, and a horizontal electric source in a high conductivity region (the ocean)

couples to a low conductivity region (the sea-floor) better than a vertical electric or magnetic source. The transmitter is connected to a surface power source by an insulated cable. The current circulating in the cable is a high-voltage AC (typically 400 Hz).The antenna is towed close to the seafloor (commonly at a height of 25 to 100 m) to maximize coupling with seafloor rocks and sediments and to minimize coupling with the air. Transmission currents are typically binary waveforms with fundamental and higher harmonics from 0.1 to 0.25 Hz. Square waves, with geometrically decreasing odd harmonics, were used initially (e.g., Ellingsrud et al., 2002), although the present trend is to shape the waveform to have a more desirable frequency content; a similar approach was used early on for academic surveys by Cox et al. (1986) and Constable and Cox (1996) (Constable, 2010).

The electric field and magnetic receivers we describe are the ones developed and used by the SCRIPPS Institute of Oceanography. They consist of a system of low noise and low impedance silver-silver chloride electrodes and an AC-coupled electric field amplifier (Webb et al., 1985), which measures the horizontal electric field at the end of 10 m long dipoles. Electric field noise on the electrode and amplifier system using a 10 m antenna is about 10^{-10} V/m/Hz$^{1/2}$ at 1 Hz. Horizontal magnetic fields are measured using sensitive and low power induction coil magnetometers designed at SCRIPPS Institute of Oceanography. This configuration makes the instrument capable of measuring both electric and magnetic fields in the .01 to 10,000 s period range, although the attenuation of the natural source MT fields through the ocean limits the shortest periods to about .1-10 s, depending on the waterdepth (http://marineemlab.ucsd.edu/instruments/receiver.html).

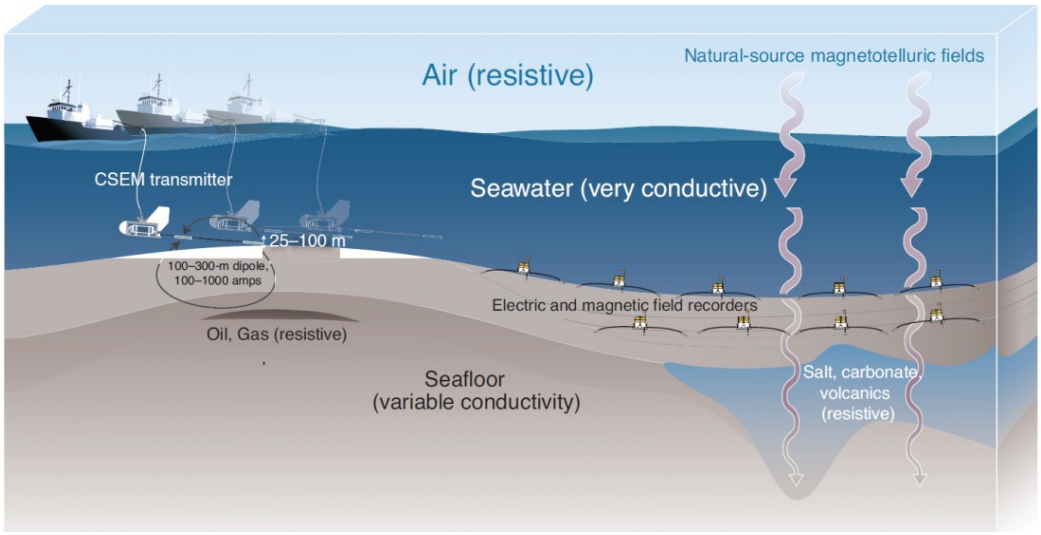

Figure 1.7: *from Constable (2010); marine EM concepts: Electric and magnetic field receivers are deployed on the seafloor to record time-series measurements of the fields, which could be used to compute MT impedances. The seafloor instruments also receive signals emitted by a CSEM transmitter (towed close to the seafloor) at ranges of as much as about 10 km. The MT signals are associated with largely horizontal current flow in the seafloor, and are sensitive only to large-scale structure. The CSEM signals involve both vertical and horizontal current flow, which could be interrupted by oil or gas reservoirs to provide sensitivity to these geologic structures even when they are quite thin.*

Transmitted electric fields are directly proportional to the source dipole moment A, in turn given by the dipole length times the emission current. Data for interpretation are normalized by the dipole moment, so the system noise floor gets lower as A gets larger, allowing larger source-receiver offsets to be recorded and deeper structure to be detected (Constable and Srnka, 2007).

One of the main limitations on CSEM data quality is the navigation of the transmitter (Constable, 2010).

1.9 Modeling

A frequency-domain 1D solution for a horizontal electric dipole transmitter has been available since Chave and Cox (1982) published their analysis of the 1D method. Flosadottir and Constable (1996) made some changes to the Chave and Cox forward code and implemented the regularized Occam's inversion scheme of Constable et al. (1987). Since

then, several other codes have been written, such as the fully anisotropic model of Løseth and Ursin (2007) and the code of Key (2009) mentioned above. The Key code allows any source-receiver geometry and component, includes the Occam's inversion scheme, and is publicly available (Constable, 2010). The relative speed and simplicity of 1D modeling has made it an attractive tool for CSEM interpretation, particularly because, as noted above, the 1D approximation is quite good for tabular bodies when both source and receiver are over the target. Of course, there will be limitations for using 1D modelling over more complicated features (Constable, 2010).

Because of the 3D nature of the source field, the move from one to two dimensions for CSEM modeling is not as easy as it is for MT modeling. Indeed, from an algorithmic point of view, in marine CSEM it is easier to go directly to three dimensions and avoid the complexity of collapsing the along-strike fields in 2D models using a transformation and this is what industry has tended to do (Constable, 2010). Finite-difference algorithms, in which the differential form of Maxwell's equations are approximated by differencing fields between nodes on an orthogonal mesh, have proved particularly attractive for 3D CSEM modeling, and several codes have been written (e.g., Newman and Alumbaugh, 1997; Weiss and Constable, 2006; Commer and Newman, 2008) (Constable, 2010). One disadvantage of finite-difference meshes is that small node spacings, perhaps necessary to capture and accurately model structure in one part of the mesh, propagate in all three directions, making the mesh very large. However, 3D forward modeling using this scheme is quite tractable on modern computers (Constable, 2010).

The data we have used to test the methods developed during this work was obtained, instead, using the finite-element method (FEM) to solve the differential form (PDE) of the Maxwell's equations. The Finite Element Method (FEM) is a powerful numerical technique that has been used to solve a variety of problems in thermal, electromagnetic, fluid and structural mechanics domains. The greatest advantage of FEM is its ability to handle truly arbitrary geometry. Probably its next most important features are the ability to deal with general boundary conditions and to include non-homogeneous and anisotropic materials.

These features alone mean that we can treat systems of arbitrary shape that are made up of numerous different material regions (Akin, 2005). Each material could have constant properties or the properties and could vary with spatial location (Akin, 2005).

The principle of the FEM method is to replace an entire continuous domain by a number of sub-domains in which the unknown function is represented by a simple interpolation function with unknown coefficients (Jin, 2002). Thus, the original boundary-value problem with an infinite number of degree of freedom is converted into a problem with a finite number of degree of freedom, or in other words, the solution of the entire system is approximated by a finite number of unknown coefficients (Jin, 2002). Then a system of algebraic equations is obtained by applying the Ritz variational or Galerkin procedure, and, finally, the solution of the boundary-value problem is achieved by solving the system of equations (Jin, 2002). Therefore, a finite element analysis (FEA) should include the following basics steps:

1. Discretization or subdivision of the domain.
2. Selection of the interpolation functions.
3. Formulation of the system of equations.
4. Solution of the system of equations.

A finite-element forward code for CSEM was written by Li and Key (2007) and has been broadly distributed.

A 2D finite-difference forward and inverse code was published by Abubakar et al. (2008) and used on real data, but this code is proprietary. Other 1D, 2D, and 3D codes have been written and are being used on a proprietary basis also. As already noted by Constable (2010), very different results may be obtained from the same data, as set by different contractors using different inversion codes. This depends on several elements: intrinsic ambiguity of the inverse problem, a priori independent information, specific code limitations and others.

The software we have used to obtain the synthetic data is COMSOL Multiphysics^{TM}, which is commercial software to solve numerically the Maxwell's equations using the FEM method.

Chapter 2

"Singular Function Normalization": a fast interpretation method for CSEM data.

2.1 Introduction

All the electromagnetic (EM) methods are aimed at determining the resistivity distribution in the subsurface. The multitude of the EM methods reflects the multitude of the sources (for example: horizontal electric dipole (HED), magnetic electric dipole (MED)) and the multitude of the generated signals.

The electromagnetic properties of the matter are described by the electrical permittivity, the magnetic permeability and the electric conductivity. All the active electromagnetic methods (the source of the EM field is an antenna) are named "Controlled Source Electromagnetic" (CSEM) methods. Unlike the CSEM methods, the magnetotelluric method (MT), to know the resistivity distribution in the subsurface, uses the natural electromagnetic fields generated by:

1) The interaction of the solar wind with the earth's magnetic field (for the lower frequencies (<1 Hz).
2) The world-wide thunderstorm, usually near the equator (for the higher frequencies).

The method that we are studying is mCSEM method. This method was used first in academia and today is widely used by the oil companies as support to other geophysical method. In fact, generally the oil reservoirs

show higher values of resistivity than the surrounding materials and so this method can be a valid tool to detect the reservoirs and to monitoring them during the extractions activity.

SBL can be very useful especially when there is not a strong acoustic impedance contrast between the sediments oil saturated and the surrounding sediments. Moreover the use of the SBL method is motivated by the particular sensitivity of seismic methods to trace amounts of gas in the pore fluid "Fizz Gas" (Constable, 2010).

This method is a frequency domain method and uses as source a horizontal electric dipole (HED) towed by a ship in the water column; the signal is acquired by receivers array deployed on the seafloor (Eidesmo, 2002). The HED emits a low frequency electromagnetic signal (0.1 Hz – 10 Hz) propagating both in the seafloor and in the water column.

As we have seen in the previous chapter, the decay rate in amplitude and phase of the EM signal is controlled by several mechanisms. The first is geometric spreading from the transmitter, which in the low-frequency limit is simply the characteristic $1/r^3$ dipole decay so familiar to users of DC resistivity sounding. The second is the galvanic effect associate with current flowing across a conductivity boundary (Constable, 2010). The last is the inductive attenuation and phase shift occurring when the skin depths are comparable to the distance over which the EM energy has travelled (Constable, 2010). However, the values of the measured amplitude and phase depend by the subsurface resistivity.

The Figure 2.1 shows the setting of a CSEM survey and the propagation of the signals emitted by the HED.

The signals in the Figure (Loseth, 2006) represent: I) the response of the sea – surface (airwave), II) the direct field, III) the response from the seabed, IV) the wave reflected from the resistive layer and V) the guided wave propagating in the resistive layer. At short offsets (< 2 km) between the source and receiver, the direct field (path II) dominates the received signal. At longer offsets, the dominating contributions are due to the resistor (path V) and sea-surface (path I). These contributions

contain multiple reflections in the water column, which are not illustrated. In deep waters, the response from the sea-surface will lower, due to the heavy damping of the signal in the water column. If the reservoir is not resistive the guiding effect will not be present and in this case the dominating signal from the subsurface will be from the lateral wave along the seabed (path III) (Loseth, 2006).

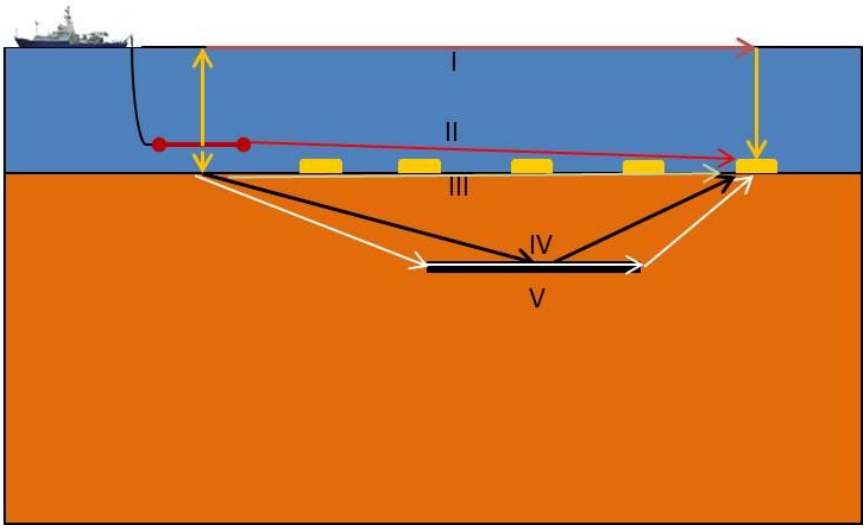

Figure 2.1: *Layout of a CSEM survey. The transmitter antenna is towed by a vessel.*

The Figure 2.2 (green line) shows the signal obtained at the receiver centered in correspondence of the resistive body. In particular, I show the amplitude of the in-line electric field component versus offset (the distance between the source and the receiver) in a semi-logarithmic scale (MVO). As we can note, the signal shows 2 local maximum located at the boundaries of the resistive body. The red prism in the Figure represents the lateral extension of the anomalous body. So, the shape of the MVO function is strongly influenced by the presence of the anomalous body.

In this chapter we propose a fast and low computational cost method to interpret this kind of signals. The electromagnetic inverse problem associated with marine CSEM data is ill-conditioned and ill-posed, and strong non-uniqueness problems can arise. Additional artifacts can be introduced if the mesh used for the forward calculation by finite-difference algorithms is not properly set (Dell' Aversana, 2007). So, some authors have proposed the use of some *attributes*, such as the

normalized anomalous response (NAR) and the asymmetry, to know the areal distribution of the resistor in a fast and easy way.

NAR is the amplitude of the observed electric or magnetic field divided by the amplitude of a reference field (Dell' Aversana, 2012), the asymmetry, instead, is an attribute based on the asymmetry between the in-towing and out-towing responses (Dell'Aversana, 2010). Both attributes have some limitations; in fact, in the first case, the value of NAR is strictly dependent on the used model to obtain the reference field or on the data used as a reference; instead, regarding the symmetry case, this attribute suffers for an intrinsic ambiguity: it is null both when the receiver is far from any resistive boundary and also when the receiver is located above the center of a resistive body (Dell' Aversana, 2012). However Dell'Aversana (2012) proposed to combine the two attributes in order to use jointly them.

Here we propose a method based on the evaluation of new attributes, which can help us to know the areal extension of the resistors. The method is based on the approximation of the MVO signals with singular functions such as the *Lipschitz singularity* and the *exponential singularity* ones. Such attributes will be the exponent of the *Lipschitz singularity* function and the coefficient of the exponent *exponential singularity* function.

We have tested the method on synthetic and real data.

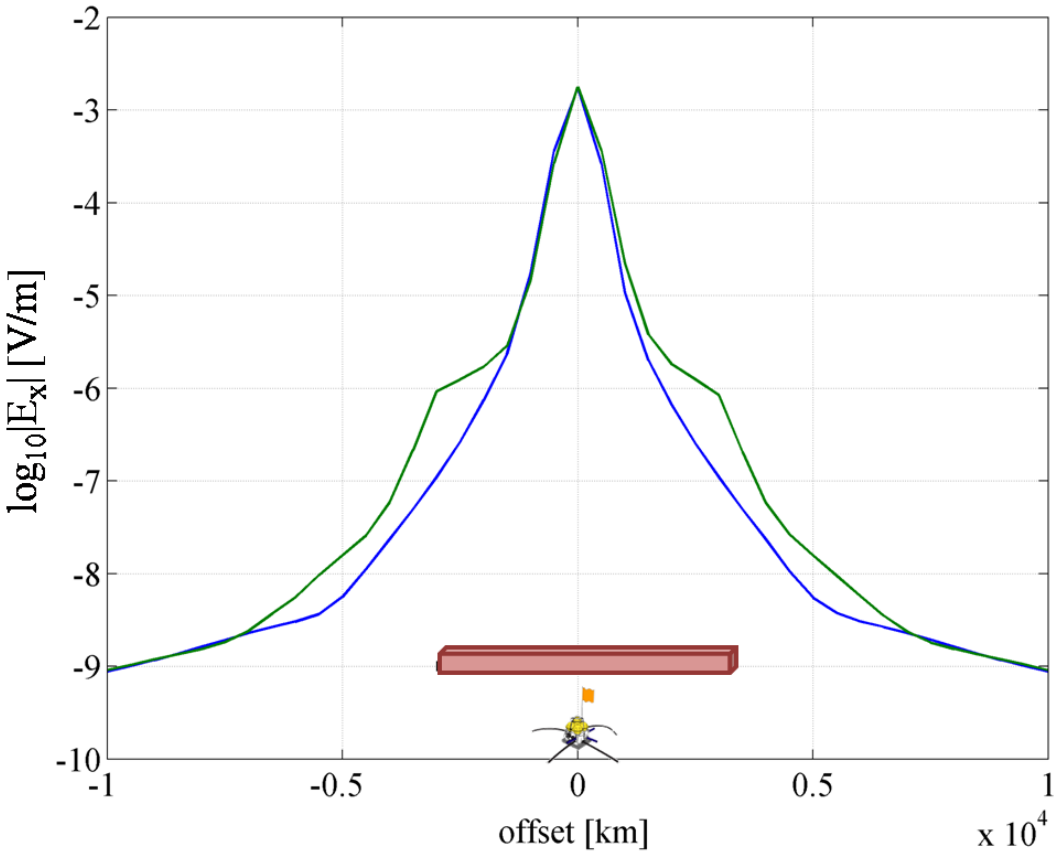

Figure 2.2: *Green function: MVO function obtained at a receiver centered on the resistive body shown in Figure 2.1. Blue function: MVO response of the half-space. The red thin sheet represents the lateral extension of the resistive body.*

2.2 Method

As shown in Figure 2.2 (green MVO), the shape of an MVO depends on the presence of resistive buried bodies. We may then approximate the measured MVO with suitable functions, as the Lipschitz-Hölder singularity and the exponential singularity functions, in order to get information about the areal distribution of the buried resistors.

Assuming as origin of the x-axis (offset) the position of the maximum of the MVO function, the Lipschitz-Hölder singularity function can be written as:

$$y = A|x|^{-b} \tag{2.1}$$

the exponential singularity function, instead, can be written as:

$$y = Ae^{-b|x|} \tag{2.2}$$

The method is based on the estimation of the exponent b of the Lipschitz-Hölder singularity function (equation 2.1) and of the coefficient b of the exponent of the exponential singularity one (equation 2.2). So, in either case, the b coefficient is the attribute helping us to define the areal distribution of the resistors.

Since the receiver can be not centred on the resistive body, we assume separately the ascendant branch ($x<0$) and the descendent branch ($x>0$) of the MVO functions, so we will estimate respectively the b^- and the b^+ coefficients for respectively $x<0$ and $x>0$.

In particular, since the MVO functions present a local maximum in correspondence of resistive bodies, we will expect a b coefficient lower than the value we would expect in the pure half-space case.

2.3 Synthetic test

We first test the method on a synthetic dataset.

The synthetic data were obtained using COMSOL Multiphysics™. This software solves the Partial Differential Equation (PDE) using the Finite Elements Method (FEM). In particular the software solves the Maxwell equations using a variational approach (Ritz method).

The reference model used to obtain the data is a 3D model. In particular we have considered a 1 km tick water column characterized by an electrical conductivity of 2.3 S/m, a half-space of 1.5 S/m conductivity, and a thin prism 6km x 3km x 100m representing an oil reservoir. The array is composed of 21 CSEM receivers spaced 600 m each other, deployed on the seafloor; the HED antenna is 150 m long with a 0.5 Hz fundamental frequency and it is towed by a ship at a h=30 m altitude from the sea-floor.
With just one receiver, as shown in Figure 2.2, the signal is measured at different distances from the antenna (offset), each one corresponding to a transmitter position along a given profile. For computational efficiency,

we used the reciprocity property, thanks to which the system *array of transmitters-single receiver* is replaced by a new system: *array of receivers* (at the transmitter positions) -*single transmitter* (at the receiver position). Numerical tests have demonstrated the efficiency of this procedure, also in agreement with other researches (Newmann et al., 2010).
In Figure 2.3 the MVO curves are shown for all the 21 CSEM receivers. As we can see, the shape of the shown signals is strongly influenced by the presence of the resistor, depending from the receiver position.

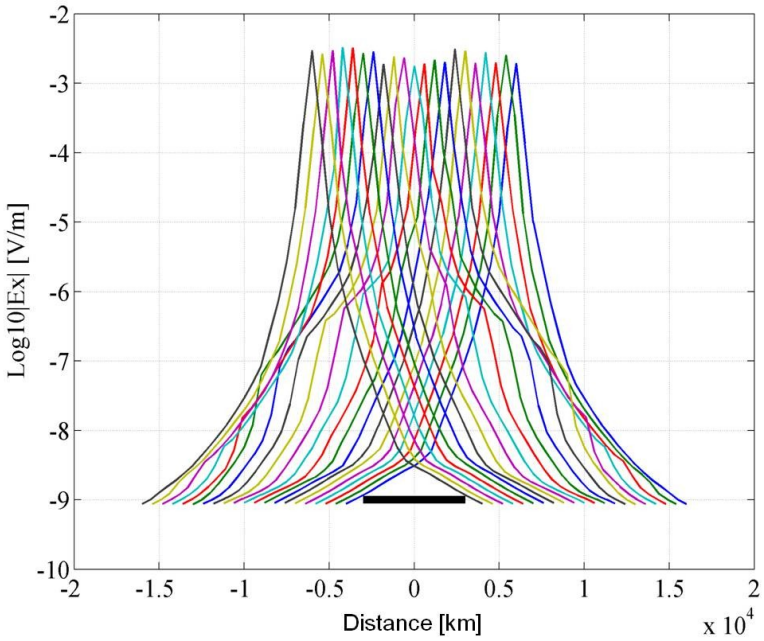

Figure 2.3: *MVO signals obtained starting from the model described in the paragraph, considering 21 receivers spaced 600 m each other.*

We have applied the SFN method to this dataset and have evaluated the b^- and b^+ coefficients, which minimized in a least-square sense the misfit between the MVO signals and the Lipschitz-Hölder singularity function (Figure 2.4). As expected, the *b*-curves in the Figure offer a meaningful description of the position of the resistive body, as described by a sharp transition (a low) at the two main boundary points of the resistive body. In particular, b^- curves (green curves) show a minimum at the right boundary of the resistive body while b^+ curves (blue curves) show the minimum in correspondence of the left boundary of the same body.

Than we done the same using the exponential singularity function (Figure 2.5).

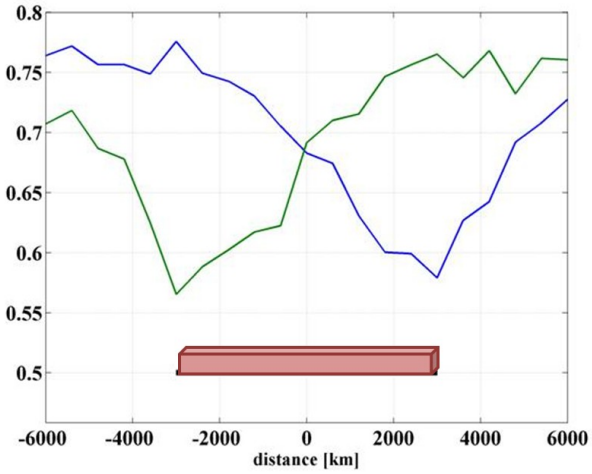

Figure 2.4: *b^- and b^+ coefficients, which minimize in the least-square sense the misfit between the MVO signals and Lipschitz-Hölder singularity functions. The red prism represents the resistive anomalous body.*

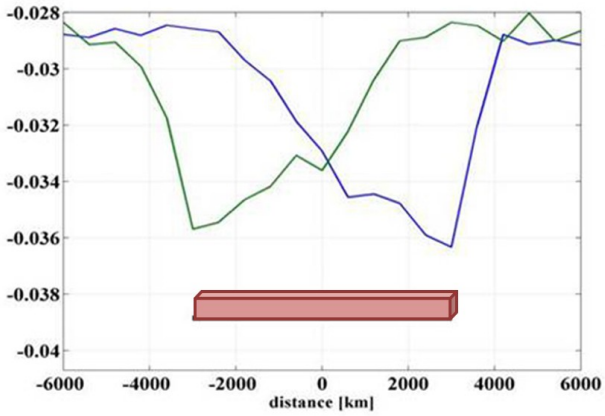

Figure 2.5: *b^- and b^+ coefficients that minimize in the least square sense the misfit between the MVO signals and exponential singularity functions.*

To have a single attribute correlated to the shape and the extension of the resistive body we have considered the mean value between the b^- and b^+ coefficients, b_m, for both Lipschitz-Hölder singularity (LSF) and exponential singularity one (ESF):

$$b_m = \frac{b^- + b^+}{2} \tag{2.3}$$

Figures 2.6 and 2.7 show the b_m functions evaluated for both LSF and ESF functions, respectively. As we can see, the b_m function related to the ESF function shows a shaper minimum than that of the LSF case; however both the functions give a similar information about the extension and the shape of the body.

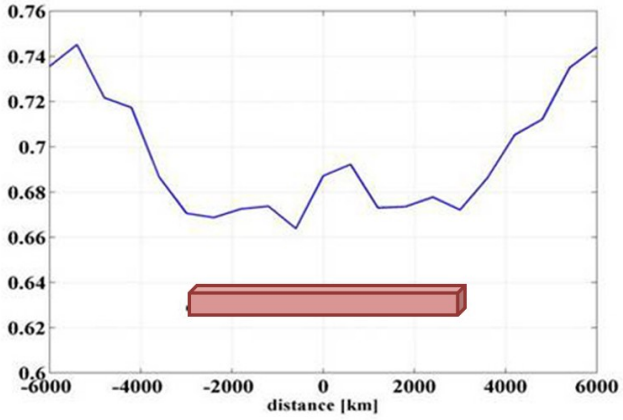

Figure 2.6: *b_m coefficients of the Lipchitz singularity functions having the best fit with the MVO signals.*

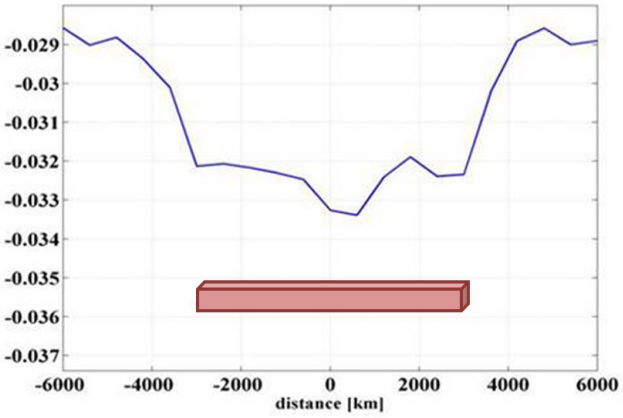

Figure 2.7: *b_m coefficients of the exponential singularity functions having the best fit with the MVO signals.*

2.4 Real case

We tested the developed method on an areal dataset kindly made available by eni e&p.

I established a procedure to process these data (Figure 2.8), which allows removing the noise from data and applying in an easy and automatic way the SFN method.

1. Data loading and outlier removing.
2. Splitting of the MVO separating the ascendant branch (x<0) from the descendent branch (x>0), to avoid problems linked to MVO asymmetry.
3. Find the best fit Lipschitz-Hölder singularity and the exponential singularity functions (with the relative coefficients b) obtained using the least-square method.
4. Plotting the estimated b coefficients on a map.

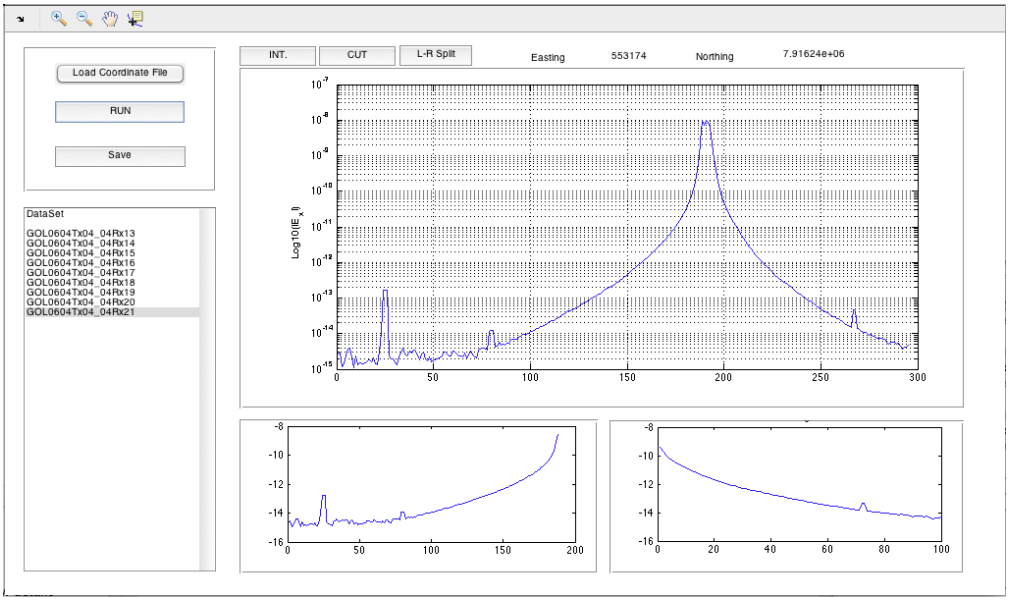

Figure 2.8: *screenshot of the graphic interface of the SFN software.*

So, we used the SFN method to know the areal hydrocarbon distribution in a well-known area explored by extensive 2D and 3D seismic campaigns and by wells penetrating hydrocarbon-bearing rocks of Late, Middle and Early Triassic ages (Dell' Aversana, 2012). The area is characterized by the presence of many faults cutting a roll-over structure and a boundary fault. The water depth varies from 260m to 440mand the seabed has a smooth topography.

We applied the SFN method to the MVO curves acquired by 83 CSEM receivers deployed along six lines (Figure 2.9).We considered the in-line

component (component of the field in direction of the antenna) of the electric field produced by a horizontal electric dipole towed by a ship in direction of the profiles. In particular, the produced field has two fundamental frequencies: 0.5Hz and 0.15Hz. Figures 2.10a and 2.10b show the maps of the b_m coefficients calculated at each receiver for the ESF and LSF, respectively for the 0.15 Hz case and Figures 2.10c and 2.10d show the b_m coefficients maps for the ESF and LSF, respectively for the 0.5 Hz case. As shown previously, the areas characterized by lows of the b_m, represent the areas characterized by the highest values in resistivity and so are probably linked to hydrocarbons or geological structures; in the maps in Figure 2.10 these low resistivity zones are shown in red. All the maps show lows in the central part and in the north-eastern part of the area. Geological studies have demonstrated that in this area there are two superimposed reservoirs (Dell' Aversana, 2012).

Due to the skin-depth effect, we expect an increase in depth resolution for the survey corresponding to the lower frequency, 0.15 Hz so to be, probably, most affected by the presence of the lower reservoir. On the contrary, the maps relative to the higher frequency, 0.5 Hz, are, in principle, more related to the upper one.

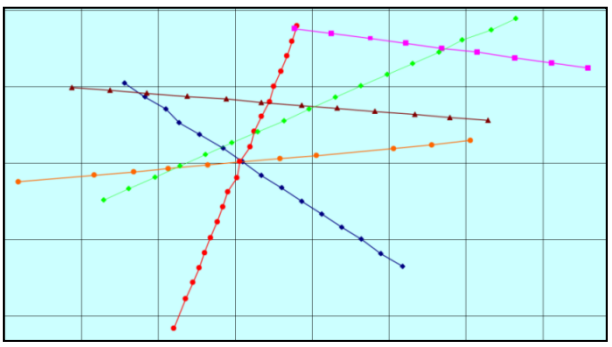

Figure 2.9: *Survey layout*

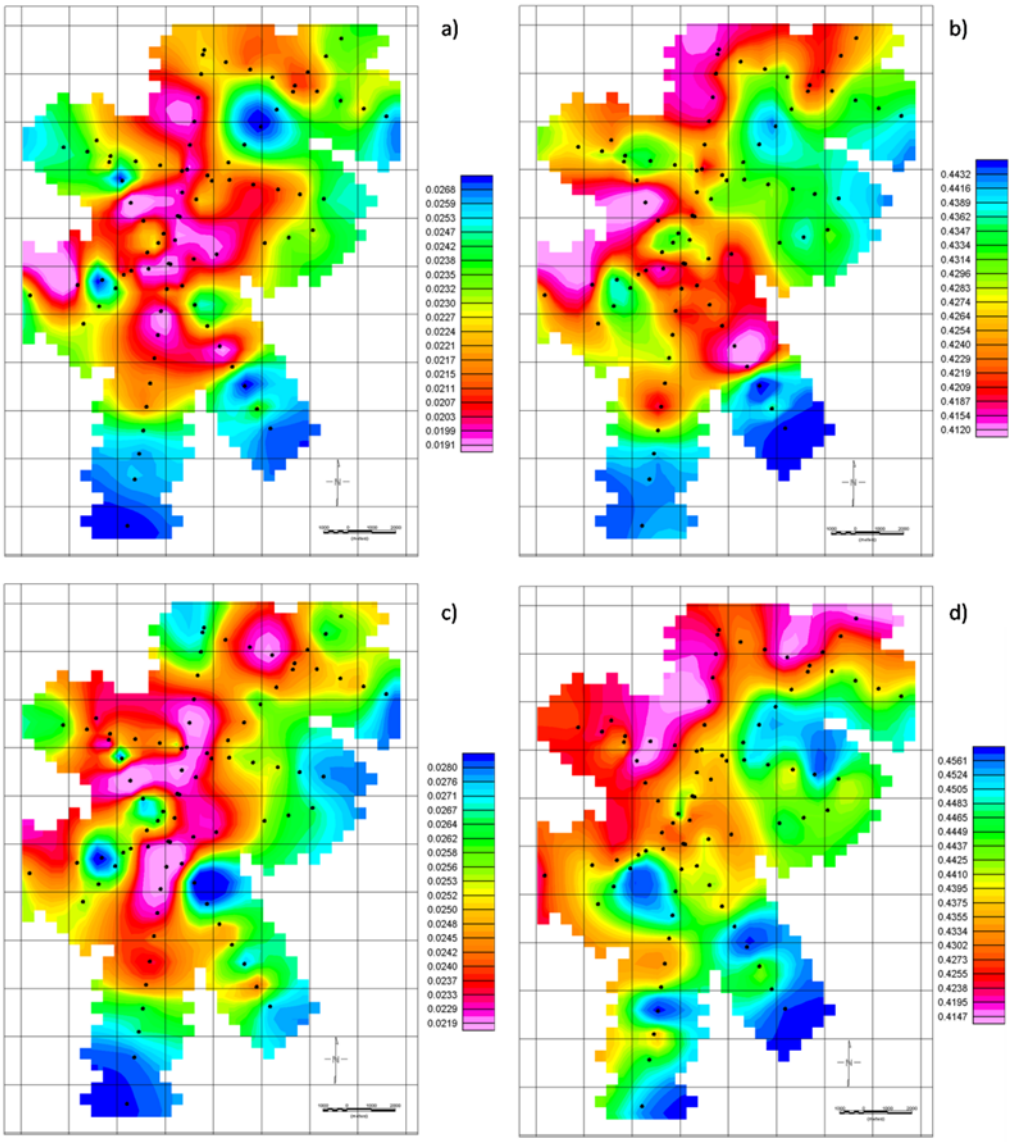

Figure 2.10: *a) Map of the best-fit b_m coefficients estimated using the exponential singularity functions for the 0.15 Hz MVO signals. b) Map of the best-fit b_m coefficients estimated using the Lipschitz-Hölder for the 0.15 Hz MVO signals. c) Map of the best-fit b_m coefficients estimated using the exponential singularity functions for the 0.5 Hz MVO signals. d) Map of the best-fit b_m coefficients of the Lipchitz singularity functions for the 0.5 Hz MVO signals.*

Comparing the maps of the b_m attribute calculated at each receiver with the map of resistor probability attribute, $P(x,y)_{HR}$ (Dell'Aversana, 2012), obtained for the same area, we can see a good agreement (Figure 2.11).

To have a better understanding of the maps, and to distinguish between the low linked to hydrocarbon and the low linked to geological structures, such as faults, we can use some information from seismic,

gravity and magnetic methods. Instead, to know the depth of this source we must use inversion or imaging methods.

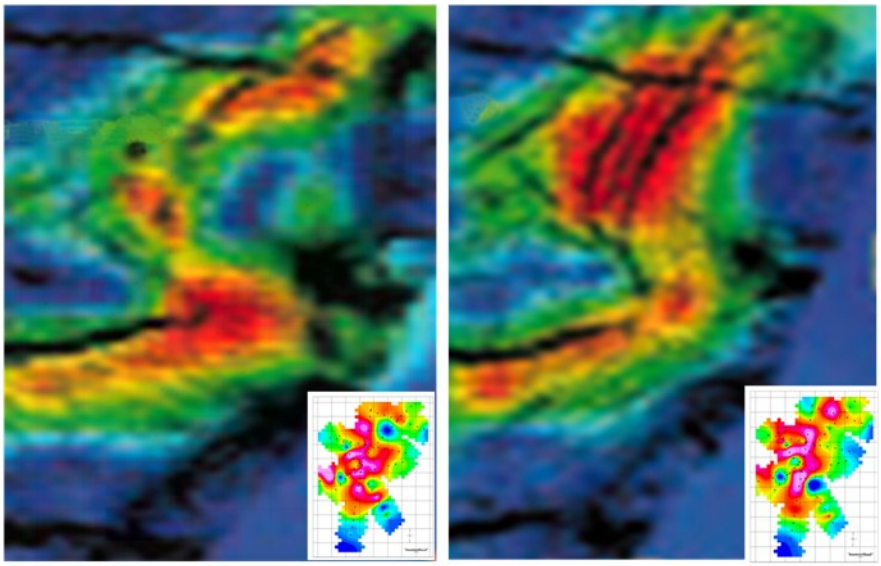

Figure 2.11*: The Figures show the maps of hydrocarbon probability respectively for the lower and upper reservoir (Dell' Aversana, 2012).*

Chapter 3

DEXP imaging technique for CSEM Data.

Introduction

In the last years the interest on "Controlled Source Electromagnetic Methods", in particular mCSEM has grown because it can be a very useful tool to support other geophysical methods as seismic and potential fields for oil reservoir exploration and monitoring.

Moreover, mCSEM methods can be utilized for CO_2 sequestration monitoring. The CO_2 often is stored under the ground to reduce a greenhouse gas, so it is important to develop a technique of monitoring the behavior of CO_2.

So, to interpret this kind of signals, during these years, several methods were developed including inversion (1D, 2D, 3D, anisotropic) and migration (Lee et al., 1987; Zhdanov et al., 1996).

Here, it is proposed a fast and computationally low cost method to get information about the areal extension, the depth and the shape of the anomalous body; this method, unlike the inversion methods, does not require *a priori* information about the source of the anomaly.

As it will be shown, we start from the assumption that a "quasi-static" EM field can be considered static at distances lower than the skin-depth. So, we can apply, with some differences, the methods used to interpret the potential field signals. In particular, we have focused our attention on Multiridge method (Fedi et al., 2009) and Depth from Extreme Points method (DEXP) (Fedi et al., 2007), which are however based on

functions satisfying the Laplace equation. We shall now show that this is indeed the case of the electromagnetic signal in mCSEM exploration.

Starting from the damped wave equations:

$$\nabla^2\mathbf{E} = \sigma\mu\frac{\partial\mathbf{E}}{\partial t} - \varepsilon\mu\omega^2\frac{\partial^2\mathbf{E}}{\partial t^2} \tag{3.1}$$

$$\nabla^2\mathbf{H} = \sigma\mu\frac{\partial\mathbf{H}}{\partial t} - \varepsilon\mu\omega^2\frac{\partial^2\mathbf{H}}{\partial t^2} \tag{3.2}$$

Where t is time, σ is conductivity, varying between 1 and 10^{-6} S/m in typical rocks, μ is magnetic permeability (usually taken to be the free space value of $4\pi10^{-7}$ H/m in rocks lacking a large magnetic content) and ε is electric permittivity (between 10^{-9} and 10^{-11} depending on water content) (Constable, 2010). The first term in the second member of the equations, named *loss term*, tends to 0 when $\sigma \approx 0$, that is in the free space case. In this case, the equations become wave equations and the wave carries information accumulated along its entire ray-path and so, as a seismic wave, the electromagnetic wave carries similar resolution at depth as it does near the surface (Constable, 2010). In rocks where σ is about 10^9 times bigger than ε, the loss term will not be negligible although the frequency value is considerable; this is the ground-penetrating radar case where, despite of the high frequencies used, of the order of MHz – GHz, the loss term will be so important to prevent penetration of more than a few meters even in resistive ground.

In our case, marine CSEM method, the used frequencies are extremely low (0.1 Hz to 10 Hz) and the conductivity values are not negligible, so the most important term of the Helmoltz equations will be loss term, whereas the second derivative term will be negligible. In this case the equations 3.1 and 3.2 will be reduced to diffusion equations:

$$\nabla^2\mathbf{E} = \sigma\mu\frac{\partial\mathbf{E}}{\partial t} \tag{3.3}$$

$$\nabla^2\mathbf{H} = \sigma\mu\frac{\partial\mathbf{H}}{\partial t} \tag{3.4}$$

In most cases we shall be dealing with alternating fields, and we may therefore assume for **E** and **H** a time dependence which is of the form:$\mathbf{E}(\mathbf{r},t) = Re\left(\mathbf{E}(\mathbf{r},\omega)e^{i\omega t}\right)$, where ω is the angular frequency of the field (i.e., ω=2π*f*) (Grant and West, 1965). In this case equations 3.3 and 3.4 become:

$$\nabla^2\mathbf{E} = i\sigma\mu\omega\mathbf{E} \tag{3.5}$$
$$\nabla^2\mathbf{H} = i\sigma\mu\omega\mathbf{H} \tag{3.6}$$

The solution of these equations has the form:

$$\mathbf{E} = \mathbf{E}_0 e^{-i\beta z} e^{-\alpha z} \tag{3.7}$$
$$\mathbf{H} = \mathbf{H}_0 e^{-i\beta z} e^{-\alpha z} \tag{3.8}$$

where α and β are the phase lag and exponential attenuation terms over distance z ofthe propagation constant k (equations 1.34; 1.44) related to the skin depth δ,

$$\delta = \frac{1}{\beta} = \sqrt{2/(\sigma\mu_0\omega)} \approx 503\sqrt{\frac{\rho}{f}}\ m \tag{3.9}$$

where we made use of equation 1.50.The skin depth is the distance over which the field amplitude is reduced to 1/e in a uniform conductor, or about 37% (given by β), and the phase progresses one radiant, or about 57^o (given by α).

So, in this last case, for a harmonic excitation, the entire earth/sea/air system is excited by EM energy, and what is measured at the receiver is a kind of average of the whole system weighted by the sensitivity to each part of the system, which decreases with increasing distance from the observer. Thus a 1-m object is easy to detect when buried 1 m below the seafloor, but impossible to see when buried 1000 m deep (Constable, 2010).

Consider now the diffusion equations 3.5 and 3.6. It is straightforward to see that in the limit $\omega \rightarrow 0$, these equations reduce to the Laplace equations:

$$\nabla^2\mathbf{E} = 0 \tag{3.10}$$

$$\nabla^2 \mathbf{H} = 0 \tag{3.11}$$

which are typical of potential field methods.

It is interesting to note that we can obtain the same result of equation 3.10 when considering not only the low value of angular frequency used for a mCSEM survey (i.e. ω=0.1 Hz), but also the common values of σ, μ of the rocks (i.e. σ=1 S/m, $\mu=4\pi 10^{-7}$ H/m) (Grant and West, 1965) so that equation (3.5) reduces to:

$$\nabla^2 \mathbf{E} \approx [(10^{-8} i) m^{-2}] \mathbf{E} \approx 0 \tag{3.12}$$

A similar reasoning can be done for the magnetic field. So, we have seen that Laplace equation occurs as a valid approximation for the electromagnetic signal as far as the mCSEM is involved. This implies that methods commonly developed for potential fields, such as DEXP and Multiridge analysis can be used also for electromagnetic data gathered in a CSEM survey.

We must however be now a little bit more precise, in order to explore in detail the zones where Laplace equation actually occurs. In order to do this, we come back to the wave equations 3.1 and 3.2 and, and consider the source sounding separation (r) and the skin-depth δ from the source of the EM field. We can distinguish three different zones, in which the electric and magnetic fields show different behaviors. In particular, using equations 1.44 and 3.9 we see that the modulus of the wave-number k can be written as:

$$|k| = \frac{\sqrt{2}}{\delta} \tag{3.13}$$

and therefore

$$|kr| = \left(r\sqrt{2}/\delta\right) \tag{3.14}$$

Where $|kr|$ is commonly referred to as the *induction number* (Zonge and Hughes, 1991).

The region electrically near the source of the field is characterized by small induction numbers ($|kr| \ll 1$, $r \ll \delta$) and is known as the "near-field" zone. The region electrically far from the source of the field is

characterized by large induction numbers ($|kr|$>>1,$r \gg \delta$) and is known as the "far-field" zone or "plane-wave" zone. The region between these zones is named "transition" zone (Zonge and Hughes, 1991). These three zones are illustrated in Figure 3.1.

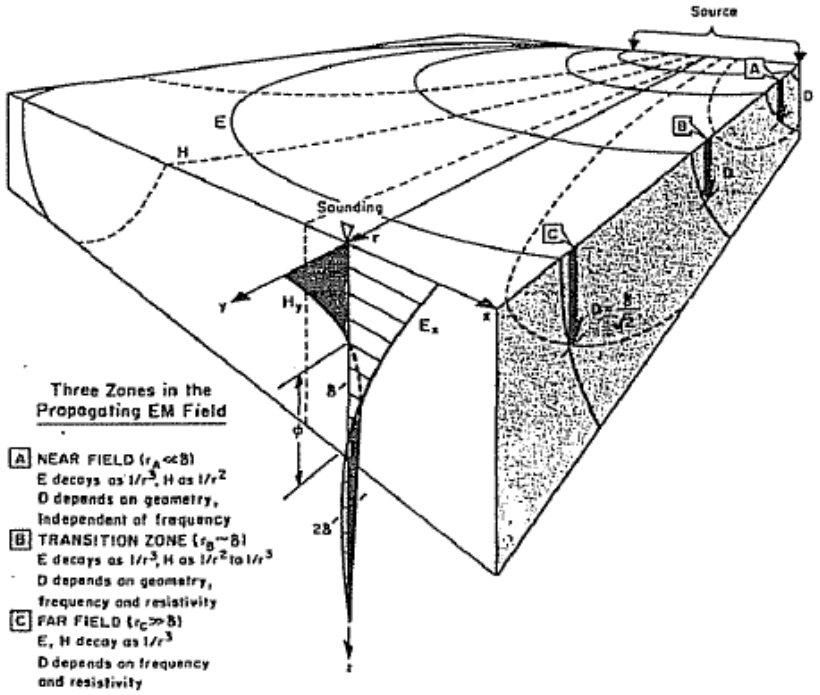

Figure 3: *from Zonge and Hughes (1991), Three zones in the propagating EM field: (a) Near field ($r_A \ll \delta$), **E** decays as $1/r^3$, **H** as $1/r^2$, the depth of investigation D depends on geometry, independent of frequency; (b) Transition zone ($r_B \sim \delta$) **E** decays as $1/r^3$, **H** as $1/r^2$ to $1/r^3$, D depends on geometry, frequency, and resistivity; (c) far field ($r_C \gg \delta$), **E**, **H** decay as $1/r^3$, D depends on frequency and resistivity .*

In particular, in the near-field zone the expressions of the electric and magnetic components of the electromagnetic field, produced by a horizontal electric dipole in the quasi-static approximation ($\sigma \gg \varepsilon$ and $r \ll \lambda_0$ where λ_0 is the free-space wavelength), expressed in a cylindrical coordinates (shown in Zonge and Hughes, 1991) become:

$$E_r \approx \frac{Idl\cos\phi}{\pi\sigma r^3} \tag{3.15a}$$

$$E_\phi \approx \frac{Idl\sin\phi}{2\pi\sigma r^3} \tag{3.15b}$$

$$E_z \approx \frac{i\mu_0\omega Idl\cos\phi}{4\pi r} \tag{3.15c}$$

$$H_r \approx \frac{Idl \sin \phi}{4\pi r^2} \tag{3.15d}$$

$$H_\phi \approx -\frac{Idl \cos \phi}{4\pi r^2} \tag{3.15e}$$

$$H_z \approx \frac{Idl \sin \phi}{4\pi r^2} \tag{3.15f}$$

As we can see from these equations for a homogeneous half-space, **E** is directly proportional to ground resistivity in the near field, and is independent of frequency. In contrast, **H** is independent of both resistivity and frequency in the near field. Under such conditions, **H** is said to be "saturated." (Zonge and Hughes, 1991).
Moreover, a very suitable consideration for us is that, as we can see from the equations 3.15*a,...,f,* the decay rate of the electric component of the electromagnetic field produced by a dipolar source in the near field zone in the quasi-static limit is $1/r^3$, instead for the magnetic field the decay rate is $1/r^2$. Therefore, as already noted by Zonge and Hughes (1991), the behavior of the electric and magnetic fields in the near zone are equivalent to those that we have in a dc resistivity survey and therefore of a static field.

In the *transition zone* the electric field decays at a rate of $1/r^3$ and the magnetic field decays at a rate between $1/r^2$ and $1/r^3$. In this case, the depth of penetration is a complex function of array geometry and frequency.

In the *far-field zone*, the impinging source field approximates a plane wave, as assumed in magnetotelluric theory. Here, the electric and the magnetic field decay at the same rate ($1/r^3$), and the depth of penetration are independent of array geometry. Moreover the horizontal **H**-field components are frequency-dependent and are also a function of the square root of ground resistivity. Hence, **H** does not “saturate” like it does in near-field zone (Zonge and Hughes, 1991).

Therefore, the electromagnetic field at extremely low frequencies, as the frequencies used in CSEM surveys, and at distances less than the skin-depth can be studied as a static field.

We must not confuse these near-field/far-field discussions with the near-field/far-field usage in antenna theory. In antenna theory, when discussing EM propagation by radiation, far-field is used to indicate the realm where the separation between transmitter antenna and receiver antenna is much larger than the free-space wavelength or $r \gg \lambda_0$. Conversely, the near-field zone is where $r \ll \lambda_0$ (Zonge and Hughes, 1991)). For the quasi-static assumptions used for CSEM calculations, near-field and far-field notations take on an analogous meaning with the substitution of the wavelength (or skin depth) in conductive earth for the free-space wavelength.

Starting from this assumption we can apply the interpretation techniques used in potential field to CSEM data.

3.1 Continuation of quasi-static electromagnetic fields.

The fact that gravity field, magnetic field and, under the conditions mentioned in the previous paragraph, the low frequency EM field obey Laplace's equation permits us to determine the field over an arbitrary surface if the field is well known completely over another surface and no masses are located between the two surfaces (Telford, 1990). This process is called *continuation*.

Following Grant and West (1965), Green's theorem states that if U and W are continuous functions within a volume V, with the first and second derivatives that are continuous and integrable, then:

$$\int_V (U\nabla^2 W - W\,\nabla^2 U)dv = \int_S \mathbf{n}\cdot(U\boldsymbol{\nabla}W - W\boldsymbol{\nabla}U)ds \tag{3.16}$$

where the surface S encloses the volume V. The restrictions on U and $W$are satisfied if we let U be the gravitational potential due to the masses within the volume V and let W be the function: $1/|\mathbf{r}-\mathbf{r_0}| = 1/R$, where $\mathbf{r}$ is the position vector of a point P outside V and $\mathbf{r_0}$ is the position vector of a point Q within V (Figure 3.1).

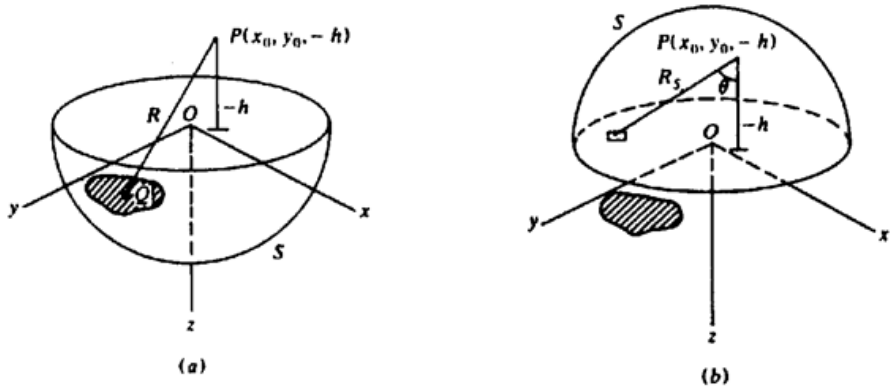

Figure 3.1: *The continuation theorem. a) Hemisphere S on positive side of xy plane. b) Hemisphere on negative side of xy plane.*

As well known the gravitational potential at a generic point *P* outside the volume *V* is:

$$U_P(\mathbf{r}) = -G \int_V \frac{\rho(\mathbf{r_0})}{|\mathbf{r} - \mathbf{r_0}|} dv \tag{3.17}$$

where *G* is the gravity constant.

Instead, inside the volume *V*, at the point *Q*, is valid the equation:

$$\nabla^2 U_Q(\mathbf{r_0}) = 4\pi G \rho(\mathbf{r_0}) \tag{3.18}$$

eliminating ρ, we have:

$$U_P(\mathbf{r}) = -(1/4\pi) \int_V (1/R) \nabla^2 U_Q(\mathbf{r_0}) dv \tag{3.19}$$

Let us apply now the Green's theorem (eq. 3.16) to the hemisphere in Figure 3.1a, and consider $U=U_S$ on the surface *S*, R_S the distance between a point of the surface *S* and *P*. Since *P* is outside the volume *V* is valid the equation $\nabla^2 W = \nabla^2 \left(\frac{1}{\mathbf{R}}\right) = 0$, we get:

$$\begin{aligned} -\int_V (1/R_S) \nabla^2 U_Q(\mathbf{r_0}) dV \\ = \int_S \left[U_S \frac{\partial}{\partial n}\left(\frac{1}{R_S}\right) - \left(\frac{1}{R_S}\right) \frac{\partial U_s}{\partial n} \right] ds \end{aligned} \tag{3.20}$$

Considering equation 3.19, the equation 3.20 can be reduced to:

$$U_P(r) = \frac{1}{4\pi}\int_S \left[U_S \frac{\partial}{\partial n}\left(\frac{1}{R_S}\right) - \left(\frac{1}{R_S}\right)\frac{\partial U_S}{\partial n}\right] ds. \tag{3.21}$$

The derivatives in the equation 3.21 are the components of the gradients normal to the surface *ds*.

If the radius of the hemisphere is made large enough, the integrand in equation 3.21 vanishes because of the factor $1/R_S$, so equation 3.21 become:

$$4\pi U_P = \int_x \int_y \left[U_S \frac{\partial}{\partial n}\left(\frac{1}{R_S}\right) - \left(\frac{1}{R_S}\right)\frac{\partial U_S}{\partial n}\right] dxdy \tag{3.22}$$

The integration is taken over that portion of the *xy* plane where the anomalous field is significantly large than 0 (Telford, 1990).

Referring, instead, to the Figure 3.1b, since in this region there are no masses, is valid: $\nabla^2 U_Q = 0$ and so the equation 3.20 becomes:

$$0 = \int_x \int_y \left[U_S \frac{\partial}{\partial n}\left(\frac{1}{R_S}\right) - \left(\frac{1}{R_S}\right)\frac{\partial U_S}{\partial n}\right] dxdy \tag{3.23}$$

The second members of the equations 3.22 and 3.23 are not the same because the unit vector **n** normal to the surface *S,* is upward (-*z* direction) in the first case and downward (+*z* direction) in the second one. For this reason, in the equation 3.22 we have: $\frac{\partial U_S}{\partial n} = -g$and in the equation 3.23 we have: $\frac{\partial U_S}{\partial n} = +g$. Moreover, because $R_S^2 = (x - x_0)^2 + (y - y_0)^2 + (z + h)^2$, on the *xy* plane is valid the equation:

$$\begin{aligned} \frac{\partial}{\partial n}\left(\frac{1}{R_S}\right) &= \lim_{x\to 0} \frac{\partial}{\partial z}\left(\frac{1}{R_S}\right) \\ &= \lim_{x\to 0}\left[\frac{-(z+h)}{R_S^3}\right] = -\frac{h}{R_S^3} \end{aligned} \tag{3.24}$$

which is independent of the direction of **n**(Telford, 1990).

Subtracting equation 3.23 from equation 3.24 we get:

$$U_P = \left(\frac{1}{2\pi}\right)\int_x\int_y \frac{g}{R_S}dxdy \tag{3.25}$$

where $R_S^2 = (x-x_0)^2 + (y-y_0)^2 + h^2$. To get $\partial U_P/\partial z$ at P, we replace h^2 in R_S^2 with z^2, differentiate and then replace z with $-h$ (note that g on xy plane is not a function of z) (Telford, 1990). So we obtain:

$$\partial U_P/\partial z = g_n = (1/2\pi)h\int_x\int_y (g/R_S^3)dxdy \tag{3.26}$$

Equation 3.26 is the *upward continuation equation* that allows us to calculate the gravitational acceleration anywhere in free-space from knowledge of its values over the surface (Telford, 1990). It is still valid for any-order derivative of g, for the magnetic field and for any-order of its derivatives.

Upward continuation can be done in more efficient and intuitive way in the Fourier domain. In fact, starting from equation 3.26, we can write:

$$U_P = (1/2\pi)h\int_x\int_y (U_S/R_S^3)dxdy \tag{3.27}$$

which represent a two-dimensional convolution:

$$U_P = \iint_{-\infty}^{+\infty} U_S(x_0, y_0, 0)\psi_U(x-x_0, y - y_0, h)\, dx_0 dy_0 \tag{3.28}$$

Where $U_S(x_0, y_0, 0)$represent the potential at the surface xy and $\psi_U$is:

$$\psi_U(x, y, h) = \frac{h}{2\pi}\frac{z}{R_S^2} \tag{3.29}$$

Applying the convolution theorem[1] to the equation 3.27 we get:

$$\mathcal{F}[U_U] = \mathcal{F}[U]\mathcal{F}[\psi_U] \tag{3.30}$$

Where $\mathcal{F}[U_U]$ is the Fourier transform of the upward-continued field and $\mathcal{F}[U]$ is the Fourier transform of the field. Note that:

[1] The convolution theorem states that, under suitable conditions, the Fourier transform of a convolution is the point-wise product of the Fourier transforms.

$$\psi_U(x,y,h) = -\frac{1}{2\pi}\frac{\partial}{\partial h}\frac{1}{R_S} \tag{3.31}$$

The Fourier transform of equation 3.31 is given by:

$$\mathcal{F}[\psi_U] = -\frac{1}{2\pi}\frac{\partial}{\partial h}\mathcal{F}\left[\frac{1}{R_S}\right] = -\frac{\partial}{\partial h}\frac{e^{-|k|h}}{|k|} = e^{-h|k|} \qquad h>0 \tag{3.32}$$

Where k is the wave-number ($k = \sqrt{k_x^2 + k_y^2}$, $k_x = \frac{2\pi}{\Delta x}$, $k_y = \frac{2\pi}{\Delta y}$, where Δx and Δy are the sampling step along x axis and y axis). So a level to level continuation can be achieved by Fourier transforming the measured data, multiplying by the exponential term of equation 3.32, and inverse Fourier transforming the product (Blakely, 1995). Some problems can occur using the upward continuation in frequency domain, in fact in this case can arise frequency-aliasing errors affecting the low-frequency content of the upwardly continued data at high altitudes (Fedi, 2007). However we can limit this problem performing Fourier transform on a larger area than that of interest.

It is important to observe that the upward continuation can be applied to a low-frequency electromagnetic field, under the conditions mentioned in the previous section and if the polarization direction may be considered constant. This last feature is likely to occur in CSEM prospecting. Besides, both the real and imaginary parts behave as harmonic functions in the near-field zone, since the electromagnetic field will there satisfy Laplace Equation (equations 3.10 and 3.11), and the continuation formula may be then applied to each of them. To test our interpretation methods based on upward continuation, we will apply the algorithm to the real and imaginary parts of the electromagnetic field scattered by simple shape bodies.

3.2 The Multiridge method

Starting from the assumption that an electromagnetic (EM) field can be considered static at distance lower than the skin depth, we can apply the

methods used to interpret the static fields (potential fields) to CSEM data.

Potential fields and, under the mentioned assumptions, EM fields of simple sources are homogeneous functions of degree n, expressing for some of them, but not for all, the fall-off rate of the field (Thompson, 1982). A more general relation to the field is given as follows. The homogeneity degree may be expressed as $n=v-p$, where p is the order of the field (i.e. electric field $p=3$) and v is an integer ranging from 0 to 3, depending on type of homogeneous or 'ideal' source (sphere (0),bottomless vertical cylinder, infinite horizontal line mass (1);bottomless dike, semi-infinite horizontal sheet (2), contact (3)) (Fedi, 2007). For instance, the scattered electromagnetic field by a homogeneous sphere have $v=0$, $p=3$ and then $n=-3$.

The Multiridge method (Fedi et al, 2009) is a purely graphic method that starting from the concept mentioned above and from the upward continuation of the field allows estimating the 3D position of the source in a very simple way. In particular, the method is based on the evaluations of the ridges from the upward continued field or his derivatives. For homogeneous and isolated sources the ridges are straight lines (in the near field zone) defined by the zeros of a potential field and its horizontal and vertical derivatives at all measured or computed levels (Fedi et al, 2009).

The number of ridges depends on the order of partial derivative of the field, and their intersection occurs in the source region at the source position. In our specific case we consider the EM field generated by a horizontal electric dipole and scattered by simple shape bodies buried in a half-space (mCSEM case). Then, we demonstrate empirically the validity of the method testing it on synthetic data under the condition mentioned above.

There are several way to draw the ridges automatically, but one of the most efficient way is to use the Canny's algorithm (1986), as proposed by Fedi et al. (2009), which permits to search for the maxima and minima of a generic function F. Considering a function $F(x,y)$ and its

gradient ∇F the algorithm searches for the maxima and minima of F as the points where Mf is locally maximum in the Af direction, where:

$$Mf = \sqrt{\left(\frac{\partial F}{\partial x}\right)^2 + \left(\frac{\partial F}{\partial y}\right)^2} \tag{3.33}$$

and

$$Af = \tan^{-1}\left(\frac{\frac{\partial F}{\partial y}}{\frac{\partial F}{\partial x}}\right) \tag{3.34}$$

So, we have the extreme points at different altitudes and we can obtain the ridges linking each of them, at a given altitude, to the nearest one computed at the altitude just above.

A mathematical demonstration of the validity of the method is reported, for the magnetic field, in Fedi et al (2009), but the same is valid also in the electromagnetic case at distances lower than skin-depth.

Using a Cartesian coordinate system with the z-axis directed downward, the magnetic field at a point $P(x,y,z)$ generated by a magnetic dipole at a point $Q(x_0,y_0,z_o)$ is:

$$F_3 = k\mathbf{f} \cdot \nabla \left[\mathbf{t} \cdot \nabla \frac{|\mathbf{M}|}{\|r - r_0\|_2}\right], \tag{3.35}$$

Where $\mathbf{r}$ and $\mathbf{r_0}$ are the position of the points P and Q respectively, $\mathbf{M}$ is the dipole moment, $k = \mu_0/4\pi$, where μ_0 is the magnetic permeability of the free-space, $\mathbf{f}$ is the unit vector in the local direction of the geomagnetic field and $\mathbf{t}$ is the unit vector in the $\mathbf{M}$ direction.

Considering the ridges formed by the zeros of the first-order horizontal derivative of the field, considering the cross-section $y=y_0$ and assuming $|\mathbf{M}| = 1$, we get:

$$\frac{\partial F_3(r,r_0)}{\partial x} = C_m\left(\frac{(X^3+XZ^2)t_yf_y+(3XZ^2-2X^3)t_xf_x+(Z^3-4X^2Z)t_zf_x+(Z^3-4ZX^2)t_xf_z+(X^3-4XZ^2)t_zf_z}{(X^2+Z^2)^{7/2}}\right) \quad (3.36)$$

where $X=x-x_0$ and $Z=z-z_0$.

From this equation we can see that the ridges are straight lines expressed by the form:

$$x - x_0 = v(z - z_0) \quad (3.37)$$

where $v = \tan(\phi)$ and ϕ is the angle that the ridge form with the vertical axis z. Assuming that the inclination and the declination of the geomagnetic field is 0^o and 90^o respectively and **f**=**t**, the solutions of equation 3.36 are:

$$\begin{aligned} x &= x_0 \\ x - x_0 &= 2(z - z_0) \\ x - x_0 &= 2(z - z_0) \end{aligned} \quad (3.38)$$

These three solutions are the equation of three straight lines intersecting at the point x_0, z_0 which is the position of the center of the sphere. So it is demonstrated mathematically the validity of the method. The same can be done considering the vertical derivative of the field or higher order derivative.

As said previously, the method is tested on synthetic mCSEM data to demonstrate empirically its validity. The synthetic mCSEM data was obtained using the software COMSOL Multiphysics™ , which uses the finite elements method (FEM) to solve the Maxwell equations.

The first and simplest case we consider is that of the electromagnetic field scattered by a homogeneous resistive (100 Ω/m), small (radius= 10 m) **sphere** positioned at *Q*(100 m,0 m,-200 m), buried in a conductive (1 Ω/m) half-space (Figure 3.2).The primary source of the field is a horizontal electric dipole (HED) having similar characteristics to the

antenna used in mCSEM prospecting and having as fundamental source frequency 0.3 Hz. The model is a 3D model with just one receiver positioned at *P*(-1000 m, 0 m, 0 m) (Figure 3.2). The off-set (distance antenna-receiver) varies to simulate a mCSEM survey with a step of 10 m both in the *x* and *y* direction.

Overlapped to the half-space is considered a 1 km thick water column characterized by an electrical conductivity of 3 S/m. In particular, to have the radiated field from the sphere are calculated the total field and the field given by the only homogeneous half-space and then are subtracted each other. It is considered the component of the scattered electric field along *z* direction (E_z). Figure 3.3 show the amplitude of the E_z component measured at each off-set.

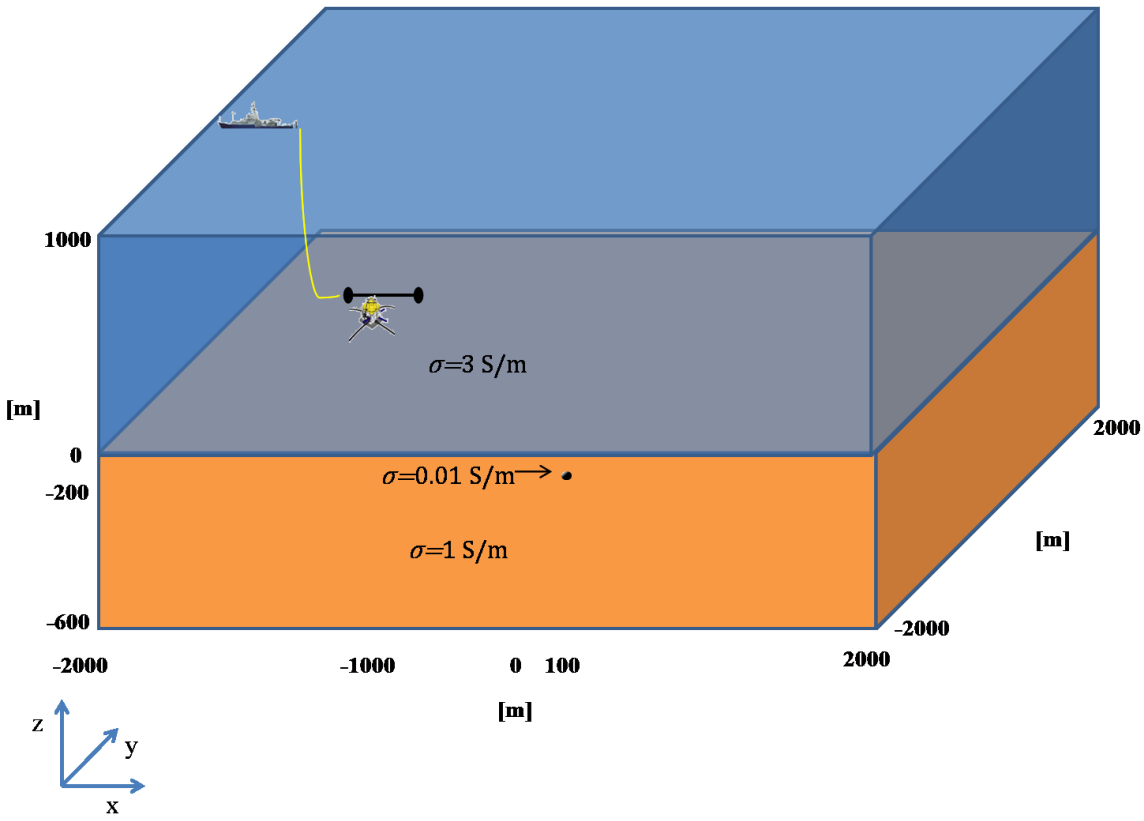

Figure 3.2: *starting model for a homogeneous resistive sphere used to solve the forward problem.*

The real part of the simulated E_z is continued (using a 3D static continuation), in the frequency domain, using a step ΔZ=10 m until the height 2000 m. The ridges (lines in Figure 3.4 and 3.5 are drawn using

the method described above (Canny's method). To avoid problems linked to frequency-aliasing errors which can arise performing upward continuation in frequency domain, the input data sequences are extended to a greater length by mathematical extrapolation using zero-padding.

In Figure 3.4 is shown the upward-continued field of the real part of E_z at $y=0$ and in Figure 3.5 is shown the second vertical derivative of the upward-continued field evaluated at $y=0$. In both Figures are shown two subsets of ridge. The ridges in pink are referred to the zeros of the first vertical derivative of the field in the first case (Figure 3.4) and to the zeros of the third vertical derivative of the field (Figure 3.5); the yellow ridge subset is referred to the zeros of the first horizontal derivative in the first case (Figure 3.4) and to the zeros of the third horizontal derivative of the field (Figure 3.5).

As we can see from the Figures 3.4 and 3.5, the ridges are not straight lines at all the altitudes, but can be considered straight near the source (the resistive sphere); in fact, as we have mathematically demonstrated previously, they are expected to be straight at distances lower than skin-depth (δ), because there the scattered electromagnetic field satisfies the Laplace equation. In this specific case, the skin depth is about 900 m. In particular, as we can see from these Figures and as expected, the number of ridges increases increasing the derivative order (the number of ridges in Figure 3.5 is higher than in Figure 3.4), so that deriving the field we can better locate the anomalous body. Moreover, as typical for potential fields, the ridges evaluated from the derived field (Figure 3.5) are better defined and straight, due to the resolution improvement caused by the derivation operation.

We may see as the near-field zone is very well defined by joining the ends of the straight part of the several ridges (dashed green curve). Since the near-field zone depends on skin depth and this in turn on the resistivity of the source, this analysis allows one to obtain, thanks to equations 3.9 and 3.15, an approximate estimate of the resistivity. For instance, as we can see from Figure 3.4 the straight part of the ridges, which are strictly linked to the skin depth, is about 850 m long (see red dotted line in Figure 3.4), so applying the 3.9 we can calculate the

resistivity contrast, which is in this case: $\Delta\rho = 0.86\ \Omega$m. Being the real resistivity contrast: $\Delta\rho = 0.99\ \Omega$m, the error is about of 13%.

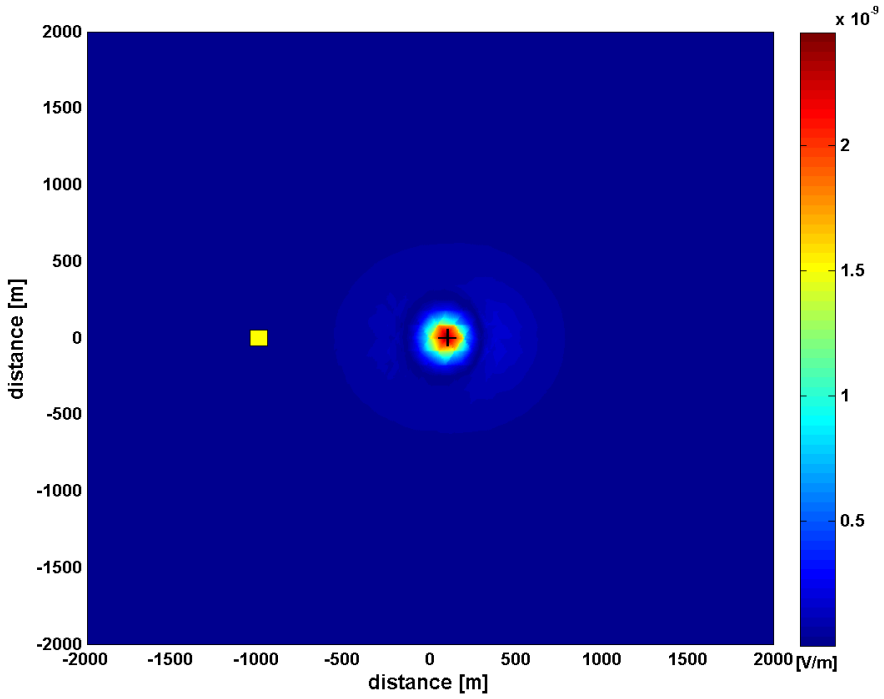

Figure 3.3: *Amplitude of the E_z component of the electromagnetic field scattered by a homogeneous resistive sphere obtained starting from the model described in the paragraph. The yellow square represent the receiver position.*

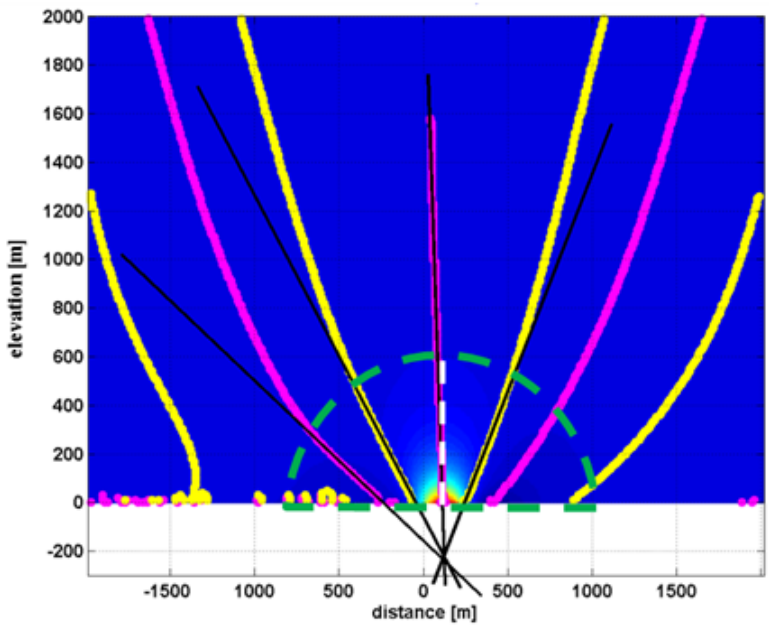

Figure 3.4: *upward-continuation of the real part of E_z scattered by a homogeneous resistive sphere at y=0. The pink lines are referred to the zeros of the first vertical derivative of the field; the yellow lines are referred to the zeros of the first horizontal derivative of the field. The dotted white line represents the portion of ridge that we have taken into account for the structural index estimation (see Paragraph 3.3.3).*

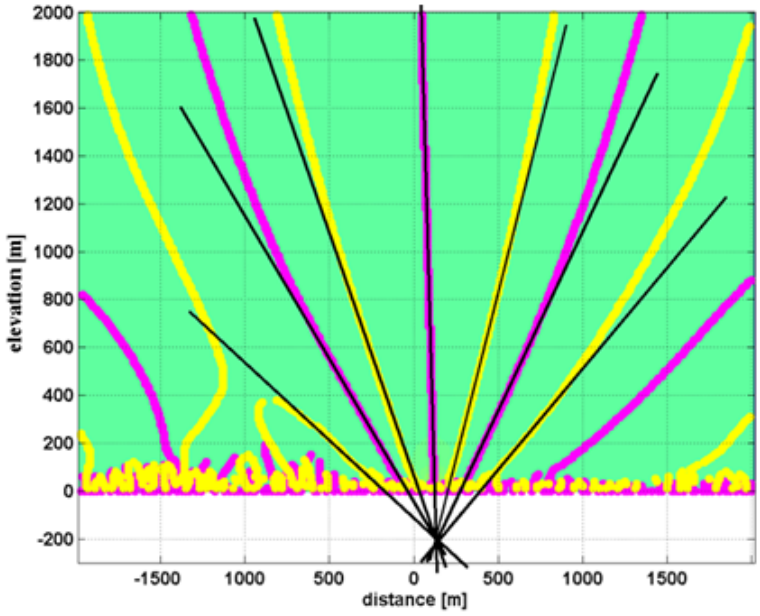

Figure 3.5: *second order vertical derivative of the upward-continuation of the real part of E_z scattered by a homogeneous resistive sphere at y=0. The pink lines are referred to the zeros of the third vertical derivative of the field; the yellow lines are referred to the zeros of the third horizontal derivative of the field.*

Another simple shape body we consider is a ***horizontal infinite cylinder*** outstretched in *y* direction, having a 10 m radius (black rectangle Figure 3.5), 100 Ω/m resistivity and buried at 200 m depth in a homogeneous conductive (1 Ω/m) half-space. The center of the cylinder is located at the point *Q* (100 m, 0 m, -200 m*)*. All the others parameters of the model are the same of the previous case (homogeneous resistive sphere) (Figure 3.6).

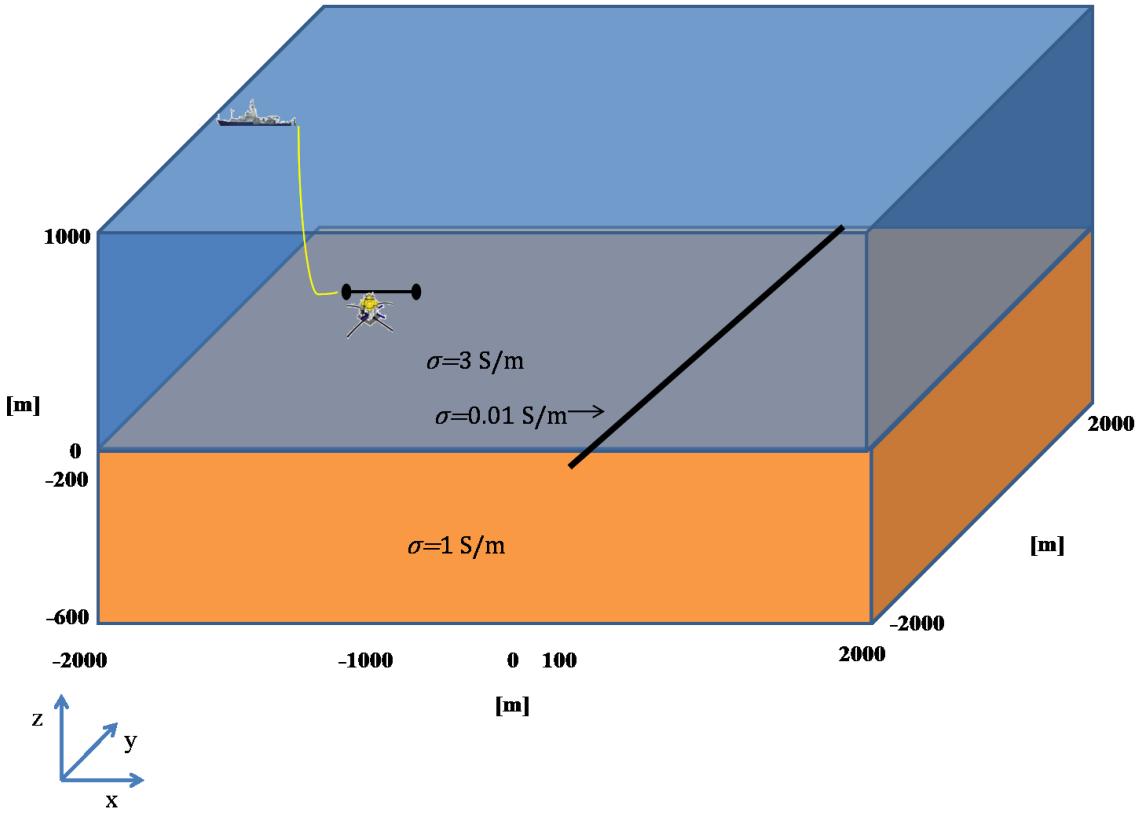

Figure 3.6: *starting model for a horizontal infinite resistive cylinder used to solve the forward problem.*

Figure 3.7 shows the amplitude of the horizontal component of the scattered E_z component of the electromagnetic field. In particular the yellow square represents the position of the receiver and the black rectangle indicates the position and the extension of the anomalous resistive body scattering the field (horizontal cylinder). The maximum of the field is located in-line with the receiver position, so, unlike what happens in potential field, the anomalous body doesn't contribute totally to the field but, most of the field is due only to a part of the body, the part closest to the receiver; so we see the infinite body as a finite, small body.

The Figure 3.8 shows the upward continued field of the real part of the E_z component of the field at $y=0$ and the relative ridges. The upward-continued field is obtained using the continuation frequency domain algorithm using the wariness mentioned above. The pink lines represent the ridges evaluated starting from the zeros of the first order vertical derivative of the field, the yellow in the Figure are the ridges obtained

starting from the zeros of the first order horizontal derivative of the field represented in each Figure. As we can see from this Figure and as it happens also in the sphere case, the ridges are not straight lines at all the altitudes. Differently then in potential fields the field is not perceived as the field of a infinitely extended sources along the strike direction (Figure 3.7). In fact, due to finite energy of the emitting antenna system, the scattered field comes just from the "lightened" part of the source (approximately from -1000<y<1000 m) so that the resulting effects is that from a finite horizontal cylinder instead. As a result, ridges are not straight lines, as in the field from a perfectly lightened infinite source.

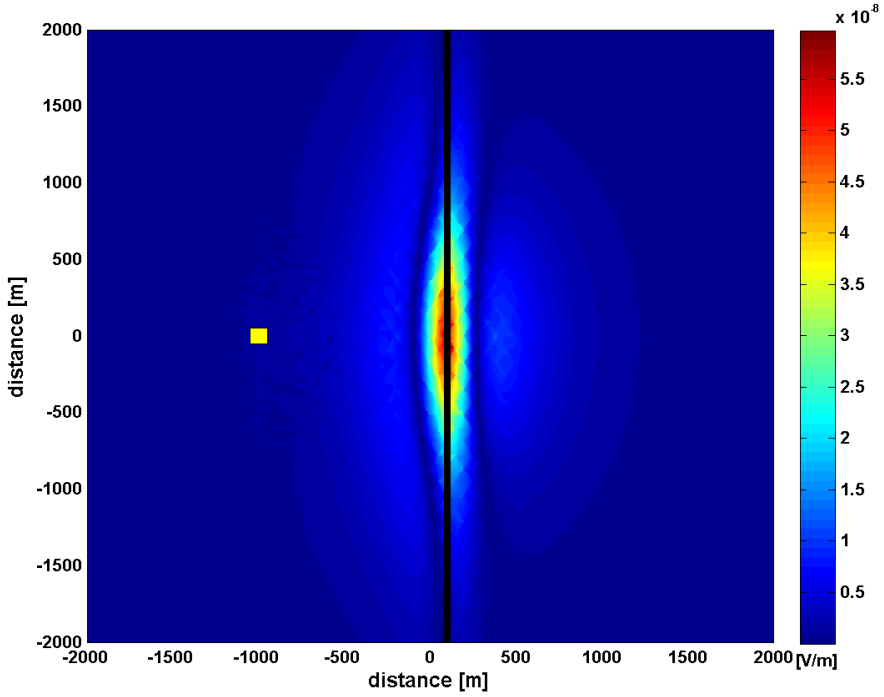

Figure 3.7: *Amplitude of the E_z component of the electromagnetic field scattered by a homogeneous resistive horizontal cylinder, represented by the black line in the Figure, obtained starting from the model described in the section. The yellow square represent the receiver position.*

Also in this case we can improve the problem using higher order derivative of the continued field, because deriving the field we can minimize the role of the end-source effects. In this specific case we have considered the second order vertical derivative of the continued field and the relative ridges (Figure 3.9). As we can see from the Figure 3.9, the straight portion of the ridges is greater than in Figure 3.8 and therefore

we can locate geometrically the portion of the body closest to the receiver in a more accurate way. However we can improve our ridge analysis also using lower frequencies. In fact, decreasing the frequency, increase the skin-depth and consequently the straight portion of the ridges. For instance, using as fundamental source frequency 0.1 Hz, the skin-depth will be: δ=1600 m and then, as we can see from Figure 3.10, we have a more extended straight portion of the ridges.

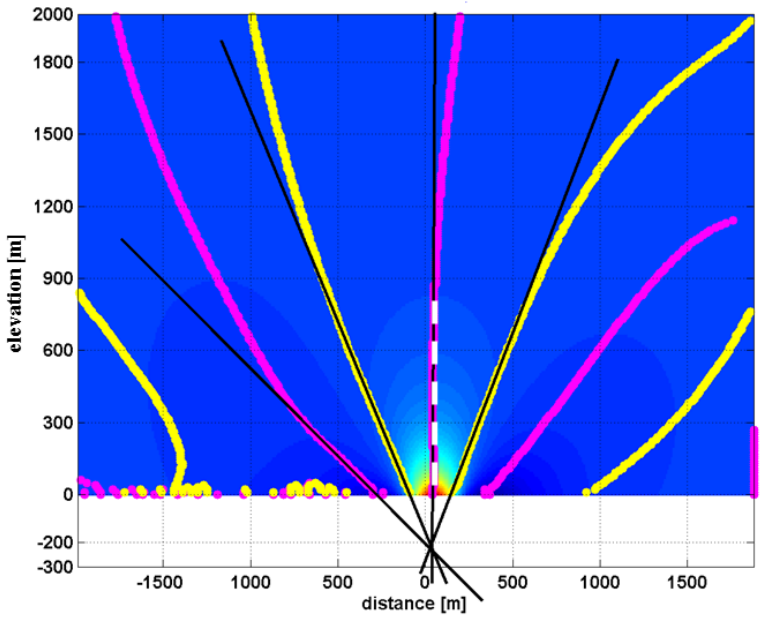

Figure 3.8: *upward-continuation of the real part of E_z scattered by an infinite horizontal resistive cylinder at y=0. The pink lines are referred to the zeros of the first vertical derivative of the field; the yellow lines are referred to the zeros of the first horizontal derivative of the field. The dotted white line represents the portion of ridge that we have taken into account for the structural index estimation (see Paragraph 3.3.3).*

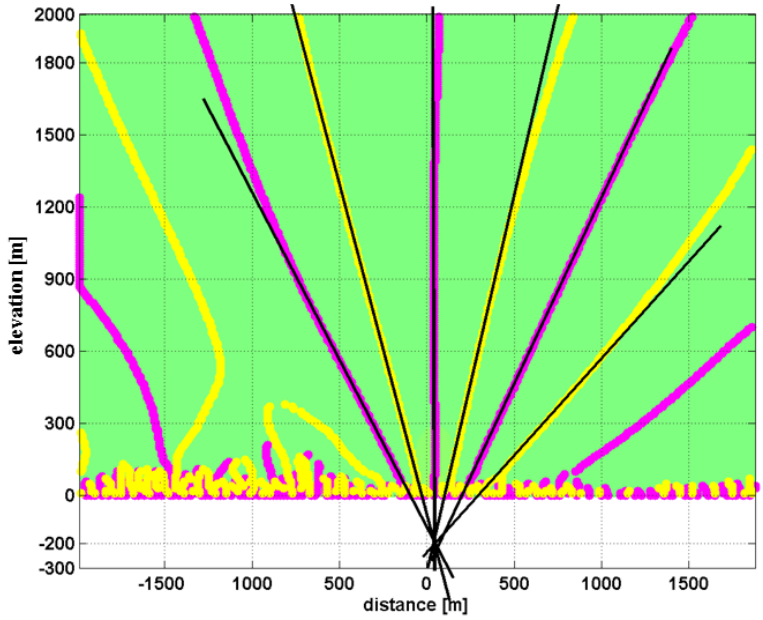

Figure 3.9: *second order vertical derivative of the upward-continuation of the real part of E_z scattered by an infinite horizontal resistive cylinder. The pink lines are referred to the zeros of the third vertical derivative of the field; the yellow lines are referred to the zeros of the third horizontal derivative of the field.*

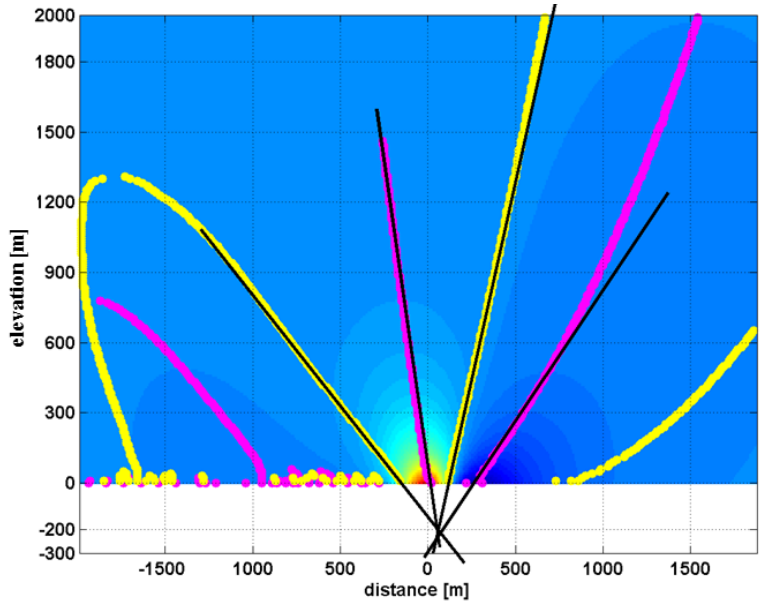

Figure 3.10: *upward-continuation of the real part of E_z scattered by an infinite horizontal resistive cylinder at y=0at 0.1 Hz. The pink lines are referred to the zeros of the first vertical derivative of the field; the yellow lines are referred to the zeros of the first horizontal derivative of the field.*

The last simple shape body we consider is a *semi-infinite plane*. This model is also the most useful for oil exploration. In fact, a hydrocarbon

reservoir can be often sketched as a thin layer. In our case the thickness of the layer is 50m. All the physical parameters of the model are the same of the previous cases. The considered fundamental source frequency emitted by the transmitting antenna is 0.3 Hz, the only one receiver positioned on the sea-floor at a distance of 1000 m from the right boundary of the semi-infinite resistive layer (Figure 3.11). The anomalous body is buried at 200 m depth from the sea-floor. In Figure 3.12 is showed the amplitude of the E_z component of the electromagnetic field. As we can see from this Figure, also in this case, as for the horizontal cylinder one, only the closest part of the source is lightened by the source placed at the receiver position, thanks to the reciprocity property. Then, also in this case, the simple shape body assumption is not completely valid because the body is as a finite layer.

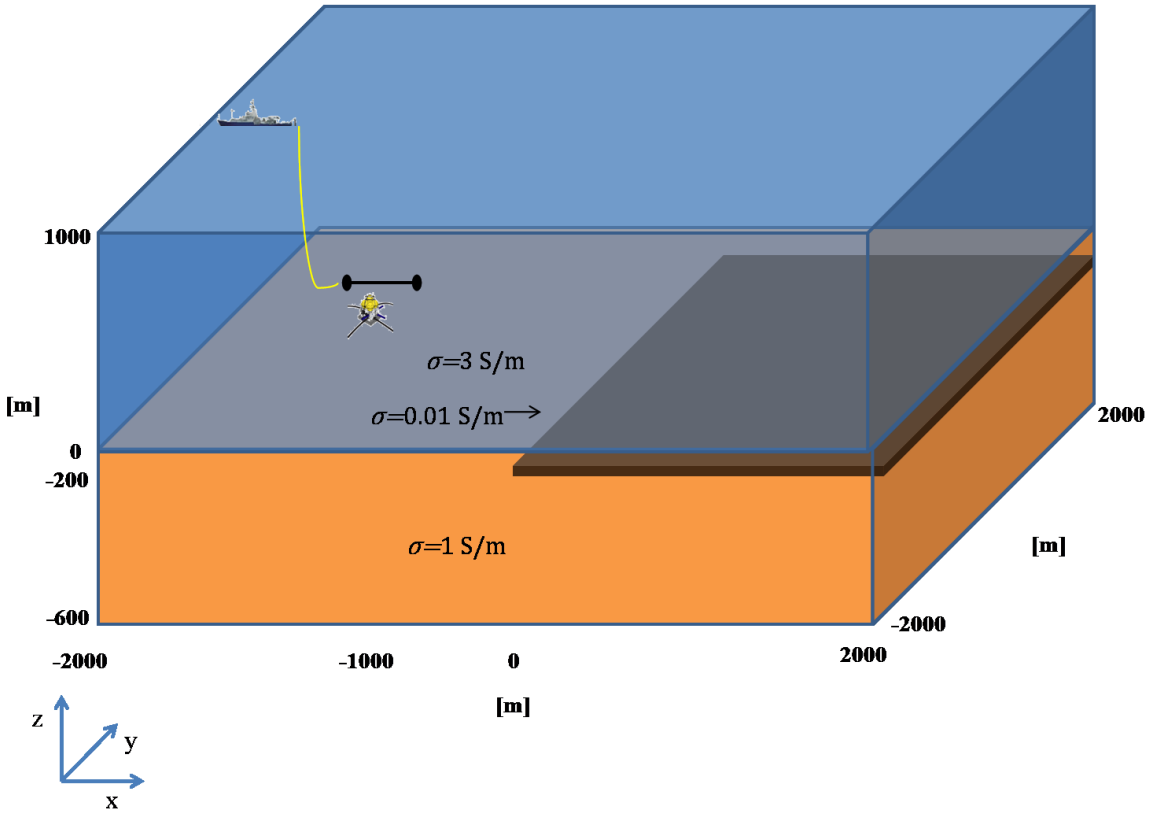

Figure 3.11: *starting model for a horizontal semi-infinite resistive layer used to solve the forward problem.*

As in the previous cases, we have upward-continued the real part of the field E_x obtaining a 3D data volume of the field. Then we show the ridges relative to the zeros of the first order vertical derivative of E_z (pink

lines) and to the zeros of the first order horizontal derivative of E_z (yellow lines) evaluated at $y=0$. Even more than in the previous case, from Figure 3.13, we can see the effects due to the fact that the body cannot be approximated completely to a simple shape body having only one fall-off rate; the ridges show a curvature also at distances from the source less than the skin depth (900 m). To minimize this problem and consequently improve our solution is done the Multiridge analysis considering the higher order vertical derivative of the continued field. In particular, we have considered the ridges evaluated starting from the second order vertical derivative of the continued field (Figure 3.14) and the ones evaluated starting from the third order vertical derivative of the continued field (Figure 3.15). In both cases (Figure 3.14 and 3.15), we can see an improvement of the solution due to the enhancement of the resolution caused by the derivation operation. In particular the result in Figure 3.15 seems to be the best solution.

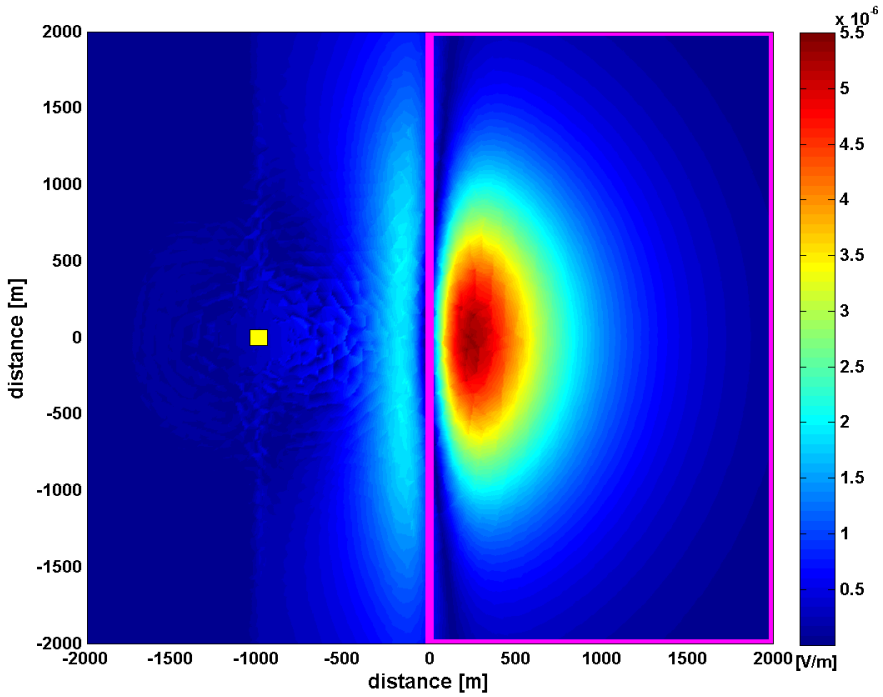

Figure 3.12: *Amplitude of the E_z component of the electromagnetic field scattered by a homogeneous resistive semi-infinite thin layer, represented by the pink rectangle in the Figure obtained, starting from the model described in the paragraph. The yellow square represents the receiver position.*

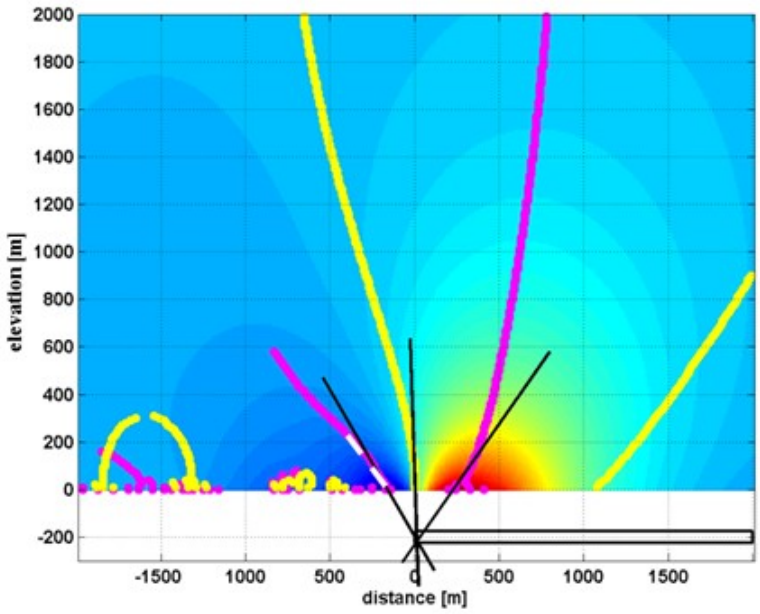

Figure 3.13: *upward-continuation of the real part of E_z scattered by the homogeneous resistive semi-infinite thin layer, represented in Figure 3.9, at y=0. The pink lines are referred to the zeros of the first vertical derivative of the field; yellow lines are referred to the zeros of the first horizontal derivative of the field. The dotted white line represents the portion of ridge that we have taken into account for the structural index estimation (see Paragraph 3.3.3).*

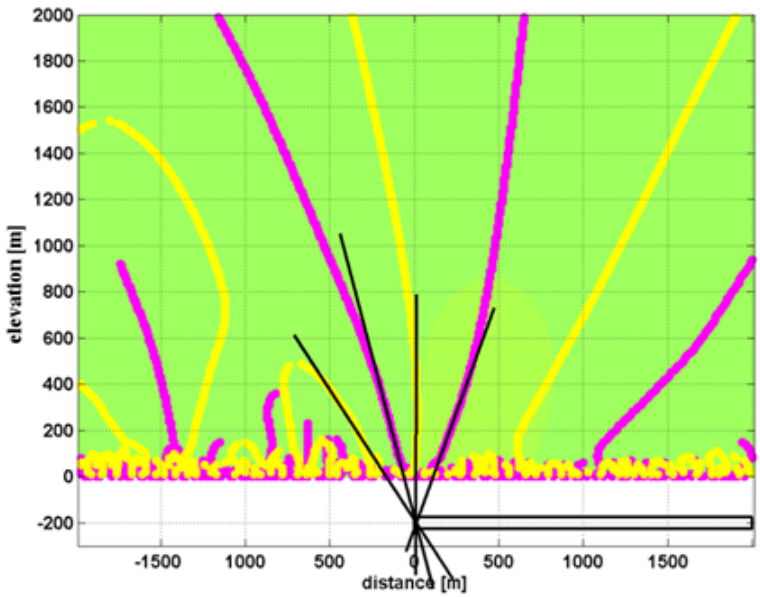

Figure 3.14: *second order vertical derivative of the upward-continuation of the real part of E_z scattered by the homogeneous resistive semi-infinite thin layer, represented in Figure 3.9, at y=0. The pink lines are referred to the zeros of the third vertical derivative of the field; the yellow lines are referred to the zeros of the third horizontal derivative of the field.*

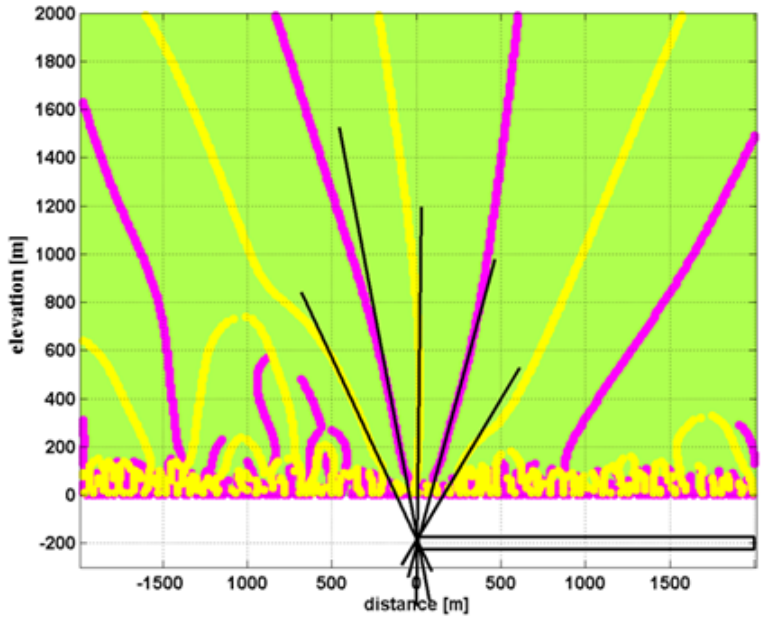

Figure 3.15: *third order vertical derivative of the upward-continuation of the real part of E_z scattered by the homogeneous resistive semi-infinite thin layer, represented in Figure 3.9, at y=0. The pink lines are referred to the zeros of the fourth vertical derivative of the field; the yellow lines are referred to the zeros of the fourth horizontal derivative of the field.*

3.3 The DEXP method

The Depth from Extreme Points (DEXP) method is a method used in potential field to have information about the tri-dimensional position of the source, his extension and his shape developed by Fedi (2007). In particular, this method fits in the landscape of semi-automatic methods, as Euler Deconvolution method, used in potential field to estimate the source position and a characteristic parameter of the source, the Structural Index (S.I), (Reid el al, 1990). The S.I. is linked to the fall-off rate of the field with distance.

Since the electromagnetic field due to homogeneous sources (as the anomalous resistive bodies studied above) has a specific and distinct fall-off rate at distances lower than skin-depth (δ), as demonstrated in the previous paragraph, the estimation of N can be useful to detect and define the kind of anomalous bodies; in this way, we can build schematic models of the subsurface.

The DEXP method is a very stable method respect to noise and can be applied to the field and his derivatives. The DEXP method for the quasi-static electromagnetic field can be applied in three steps:

- *Continuation of the field*: starting from a map of the electromagnetic field scattered from an anomalous resistive source, we have to create a 3D data volume upward-continuing the field at height lower than skin-depth. Or in 2D case, from a profile of data we have to create a section upward-continuing the field using 1D algorithm continuation. To have the scattered electromagnetic field from an anomalous source we have to subtract to the observed data the background field (the field that we should obtain if our target, the anomalous body of interest, is not present); in our synthetic tests we assume the background field as the field due to a homogeneous half-space, in the real case we assume as background field the field acquired by a receiver situated far away the anomalous body.
- *Scaling the field*: we have to scale the 3D field using specific laws. So, if the 3D field originated by a source at $\mathbf{r_0}$ is expressed by the function $f(\mathbf{r}\text{-}\mathbf{r_0})$, we have to obtain a scaled field $W(\mathbf{r}\text{-}\mathbf{r_0})$.
- *Estimating the source depth:* we have to determine the position of the source searching for the extreme points $\mathbf{r}(x,y,z)$ of $W(\mathbf{r}\text{-}\mathbf{r_0})$. As will be shown the points $\mathbf{r}(x,y,z)$ are symmetrical to $\mathbf{r_0}(x_0,y_0,z_0)$.

3.3.1 Theory of the DEXP method

In this paragraph we will show mathematically the validity of DEXP method following the demonstration given by Fedi (2007) for the gravity field of a pole source. Then, will be examined the case of the electromagnetic field scattered by a dipolar source.

Considering the gravity field $f_1(\mathbf{r})$ due to an homogeneous sphere at $\mathbf{r_0}(x_0,y_0,z_0)$ with density M=1 and normalizing by the gravity constant k we have:

$$f_1(\mathbf{r}) = \frac{(z - z_0)}{\|\mathbf{r} - \mathbf{r_0}\|_2^3} \tag{3.39}$$

If the source is at $\mathbf{r_0}(0,0,z_0)$ and the field is measured at $x=x_0$, $y=y_0$ we have:

$$f_1(z) = \frac{1}{(z - z_0)^2}. \tag{3.40}$$

The scaling function used to scale the continued field is defined as:

$$\tau(z) = \frac{\partial \log[f_1(\mathrm{z})]}{\partial \log(\mathrm{z})} \tag{3.41}$$

so, in this case, naming the scaling function for the gravity field τ_1, we get:

$$\tau_1(z) = -\frac{2z}{z - z_0}. \tag{3.42}$$

From the equation 3.42 we can see that $\tau_1(z)$ is singular at $z = z_0$, but at $z=-z_0$ we have:

$$\tau_1(-z_0) = -1 \tag{3.43}$$

it follows that

$$\left.\frac{\partial\{\log[f_1(z)] + \log(z)\}}{\partial z}\right|_{z=-z_0} = 0 \tag{3.44}$$

that can be written also as:

$$\left.\frac{\partial z f_1}{\partial z}\right|_{z=-z_0} = 0 \tag{3.45}$$

As we can see from this equation, the function zf_1 has a maximum at $z=-z_0$. This means that, scaling the gravity field with a power law of the altitude z and exponent equal to 1, we can have a scaled gravity field, W_g:

$$W_g = f_1 z \tag{3.46}$$

having a maximum at $x=x_0$, $y=y_0$ and $z=-z_0$. Obviously, the maximum is due to the fact that we have assumed a positive density contrast. If we

choose a negative density contrast we will have a minimum at the point $\mathbf{r}(x=x_0,\ y=y_0,\ z=-z_0)$. Moreover, instead to express the function W_g as function of $\mathbf{r}$, we can express W_g as function of (x_0,y_0,z_0).

We can generalize the scaling function formula to any p-th order vertical derivative of the field, f_p and to any kind of homogeneous source; in fact, starting from the p-th order derivative of the gravity field, of homogeneity degree n, $f_p\left(x=x_0, y=y_0, z\right)=\frac{1}{(z-z_0)^{N+p}}$,where $N=-n$. So we get:

$$\tau_p=\frac{\partial \log\left[f_p(z)\right]}{\partial \log(z)}=-\frac{(N+p)z}{z-z_0}. \tag{3.47}$$

At $z=-z_0$ we will have:

$$\tau_n(-z_0)=-\frac{N+p}{2} \tag{3.48}$$

Hence, the general scaled function, W_p, having as extreme point the point $x=x_0$, $y=y_0$ and $z=-z_0$, can be expressed as:

$$W_p=f_p z^{\frac{N+p}{2}} \tag{3.49}$$

Let us now consider the electromagnetic field case. The z-component of the electric field radiated by a x-directed electric dipole at a generic point $\mathbf{r}$ located in the near zone has the form:

$$E_z(\mathbf{r})=k\int_V \frac{\partial^2}{\partial z^2}\frac{\rho(\mathbf{r_0})}{\|\mathbf{r}-\mathbf{r_0}\|_2}d^3\mathbf{r_0} \tag{3.50}$$

where $k=\frac{1}{4\pi\varepsilon_0}$, ρ is the resistivity of the source of the field and $\mathbf{r_0}$ is the position of the source of the field. $\|\cdot\|_2$ denotes the vector two-norm. Also in this case for simplicity we consider ρ equal to 1 Ωm and normalize the field by k. So considering the source of the field located at $\mathbf{r_0}(0,0,z_0)$, for $y=0$ we have:

$$E_z(x,z) = \frac{k(x^2+(z-z_0)^2)\sin\alpha - 3k(z-z_0)(\cos\alpha\cdot(x-x_0)+\sin\alpha\cdot(z-z_0))}{[x^2+(z-z_0)^2]^{5/2}} \tag{3.51}$$

where α denotes the dipole orientation.

It is simple to find that the scaling function (equation 3.41) takes the form:

$$\tau(z) = -3\frac{z}{z-z_0}. \qquad \forall\alpha \neq 0 \tag{3.52}$$

As at $z=-z_0$ the scaling function will be: $\tau(-z_0) = 1.5$, the DEXP scaled electric field for a dipole source, W, will be:

$$W = E_z z^{3/2} = \frac{k(x^2+(z-z_0)^2)\sin\alpha - 3k(z-z_0)(\cos\alpha\cdot(x-x_0)+\sin\alpha\cdot(z-z_0))}{[x^2+(z-z_0)^2]^{5/2}} z^{3/2}. \tag{3.53}$$

Similarly to the gravity case, we can generalize the scaling function formula for any p-th order vertical derivative of the field, E_p , and for any kind of homogeneous source; in fact, starting from the p-th order derivative of the electric field, of homogeneity degree n, $E_p(x=x_0, y=y_0, z) = \frac{1}{(z-z_0)^{N+p}}$, where $N=-n$. So we get:

$$\tau_p = \frac{\partial \log[E_{zp}(z)]}{\partial \log(z)} = -\frac{(N+p)z}{z-z_0} \tag{3.54}$$

And at $z=-z_0$ we will have:

$$\tau_p(-z_0) = -\frac{N+p}{2} \tag{3.55}$$

Hence, the general DEXP-scaled function of the electric field, W_p, having as extreme point the point $x=x_0$, $y=y_0$ and $z=-z_0$, can be expressed as:

$$W_p = E_{zp} z^{\frac{N+p}{2}} \tag{3.56}$$

3.3.2 DEXP of simple sources

Real sources may be defined as source distributions within finite volumes with arbitrary shapes (Fedi, 2007). However, often we can approximate the complexity of the real source to semi-infinite volume-less shapes. For example we can see ridges, valleys, volcanic necks as cylinders or we can see a petroleum reservoir as a plane.

These simple shape bodies are named one-point sources, meaning that we need the coordinates of just one singular point to define them (Stavrev, 1997; Fedi, 2007).

We have seen that, also in the case of the electromagnetic field scattered by one-point sources, we can find a scaling law to scale the continued field and obtain the position of the source; in particular the scaled field, obtained through the DEXP transformation in eq. 3.56, will show a maximum/minimum in correspondence of the "one point" of the anomalous resistive body, if the resistivity contrast between the source and the background is positive or negative; in the CSEM case, however, as we showed in Figures 3.5 and 3.9 and as we will see in the next paragraphs, the maximum of the scaled field will be generally located in the part of the anomalous body resulting closer to the receiver.

A typical one point source is the horizontal infinite cylinder. The E_z component of the electric field radiated by this kind of source located at $\mathbf{r_0}(0,0,z_0)$ and measured at a generic point $\mathbf{r}$ located in the near zone can be expressed, normalizing by k and ρ as:

$$E_z = \frac{k(x^2 + (z - z_0)^2)\sin\alpha - 2k(z - z_0)(\cos\alpha \cdot (x - x_0) + \sin\alpha \cdot (z - z_0))}{[x^2 + (z - z_0)^2]^2} \tag{3.57}$$

So, the decay rate of this kind of field is $1/r^2$ and then the structural index, *N*, we have to use to scale the upward-continued electromagnetic field scattered by a horizontal infinite cylinder is 2, as shown in Table 3.1.

Using the finite element method to compute the electromagnetic field radiated by any kind of source we can obtain the respective scaling functions, by using equation 3.54.

	Scaling function at z=-z_0 (-α)	Structural index (N)
Spheres	-1.5	3
Bottomless Vertical Infinite / Horizontal infinite cylinders	-1	2
Bottomless thin vertical dyke, Semi-infinite horizontal sheet	-0.5	1

Table 3.1: *Structural indexes obtained for the most common one-point source bodies*

3.3.3 Determining the scaling exponent from the data

In the previous case, the technique of source distribution imaging by the DEXP method was successful, but we used as a priori information, the exact structural index for the several sources. In real case, this information is not available, in principle, so we need specific methods to retrieve this information before performing the DEXP transformation.

To this end we will describe now two methods, developed by Fedi (2007), for the estimating the scaling exponent, α, directly from the data. In this way, we can estimate the scaling exponent, α, to scale the continued field and we can apply the DEXP method also to investigate about more complex bodies than the simple shape bodies described above.

Criterion of extreme point invariance versus derivative order

As we have seen in the previous paragraph, changing the derivation order, *n*, does not change the position of the extreme points in the scaled transformed fields, *W*. We can use this property to estimate the scaling exponent, α.

Considering the equations 3.47, that is the general scaling function equation for a pole source: $\tau_p = \frac{\partial \log[f_p(z)]}{\partial \log(z)} = -\frac{(N+p)z}{z-z_0}$, and since: $\alpha_p = -\tau_p(z=-z_0) = 0.5(N+p)$, we have that the DEXP-transformed field $W_p = z^{\alpha_p} f_p$ has a maximum at: $z = -z_0,\ \forall p>0$.

If we use as scaling exponent a wrong scaling exponent, $\bar{\alpha}_p$, we have that the extreme point of the new scaled field $\bar{W}_p = z^{\bar{\alpha}_p} f_p$ will be at:

$$\bar{z}_p = -\frac{\bar{\alpha}_p z_0}{N+p-\bar{\alpha}_p} \tag{3.58}$$

so, we have that $\bar{z}_p = z_0$ only when $\bar{\alpha}_p = \alpha_p = (N+p)/2$.

Therefore, if we change the derivation order of the field and we are using the true scaling exponent $\alpha_p$we will have always the exact position of the source (invariance rule showed above), but if we are using a wrong exponent, $\bar{\alpha}_p$,varying the derivation order we have different positions of the extreme point, according to equation 3.60.

Criterion of DEXP scaling function intercept.

This second method allows us to estimate the scaling exponent directly from the scaling function. In fact starting from the general scaling function equation 3.47: $\tau_p = -\frac{(N+p)z}{z-z_0}$, putting z=1/q, we get:

$$\tau_p(q) = -\frac{N+p}{1-z_0 q} \tag{3.59}$$

so, as q tends to 0 we have:

$$\lim_{q\to 0} \tau_p = -N+p. \tag{3.60}$$

Hence, the intercept of τ_p versus q will give an estimate of the structural index N plus the order of differentiation, and as we can note the estimation of N does not depend on the vertical position of the source z_0.

As proposed by Fedi and Florio (2006), we can also consider the rescaled scaling function:

$$\tau_p(q, \hat{z_0}) = -(N + p)\frac{1 - \hat{z_0}q}{1 - z_0 q} \tag{3.61}$$

where $\hat{z_0}$ is a guess depth. In this case we can obtain an estimation of N+p by the value assumed by $\tau_p(q, \hat{z_0})$ when $\hat{z_0} = z_0$.

3.3.4 Synthetic tests

In this paragraph we will apply the DEXP method to the quasi-static electromagnetic fields scattered by the one-point sources described above. We have generated synthetic data by using the software COMSOL Multiphysics™.

The first case we consider is that of the electromagnetic field scattered by a *homogeneous resistive sphere*. The starting model used to obtain the data is the same of the one described in the Figure 3.2. Therefore, we consider a 100 Ωm homogeneous, small (radius= 10 m) sphere located at *Q* (100 m, 0 m,-200 m), black cross in Figure 3.2, buried in a conductive (1 Ωm) half-space. The primary source of the field is a horizontal electric dipole (HED) having similar characteristics to the antenna used in mCSEM prospecting and having as fundamental source frequency 0.3 Hz. The model is a tri-dimensional model with just one receiver positioned at *P* (-1000 m, 0 m, 0 m), indicated by a yellow square in Figure 3.3. The off-set (distance antenna-receiver) varies to simulate a mCSEM survey with a step of 10 m both in the *x* and *y* direction. Overlapped to the half-space is considered a 1 km tick water column characterized by an electrical conductivity of 3.3 S/m. To obtain the scattered field, we have simulated the field of a 1 Ωm homogeneous half-space and then we have subtracted it to the field obtained from the model described above.

The first step to perform the DEXP method is to form a 3D dataset upward-continuing the data. Figure 3.16 shows a section of the obtained 3D data volume. In particular is showed the real part of the scattered E_z component of electromagnetic field at $y= 0$ upward-continued until the skin–depth (900 m). The field is continued using an upward-continuation algorithm working in the frequency domain. And as we said in Paragraph 3.2, to avoid problems linked frequency-aliasing errors, the input data sequences are extended to a greater length by mathematical extrapolation using zero-padding.

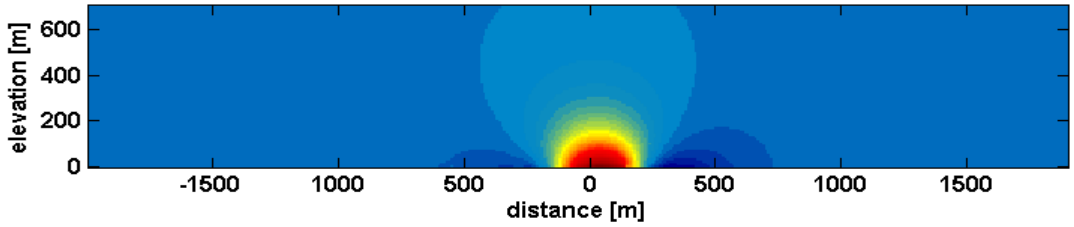

Figure 3.16: *upward continuation of the E_z component of the electromagnetic field scattered by a sphere obtained starting from the model in Figure 3.2 evaluated at $y=0$.*

Then, we have to scale the continued field inserting the appropriate structural index in equation 3.56 (in this case the derivation order p is equal to 0, because we do not consider any derivative of the field). In this case, we applied the criterion of equation (3.61) for estimating the structural index to the white signed portion of the ridge in Figure 3.4. The result, shown in Figure 3.17a, is: N=3. The scaled field, $\boldsymbol{W}$, is shown in Figure 3.17b.

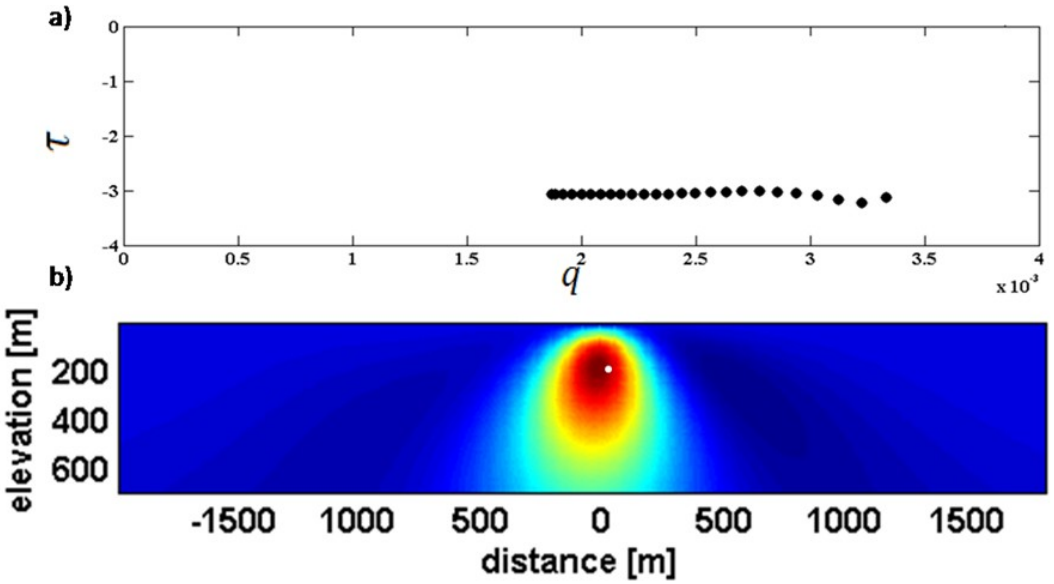

Figure 3.17: *a) estimation of the structural index obtained using the criterion of DEXP scaling function intercept (Fedi, 2007); b) DEXP imaged field obtained starting from the upward-continued field in Figure 3.13 using as structural index 3. The white circle represents the source position.*

As we can see from Figure 3.17, the transformed field, *W*, shows very clearly the occurrence of a high at the correct source position. In other words, the appropriate scaling of the field versus depth is enough to disclose the depth to source of the considered potential field by a simple inspection of the extreme points of *W* (Fedi, 2007). Therefore, the position of the extreme points of the scaled function gives us the position of the anomalous body, but as we can see from Figure 3.17 there is a spreading around the extreme point. The spreading is due to the resolution of the field and, therefore, to the depth of the source and to the fundamental frequency emitted by the antenna. To improve the resolution of the DEXP transformed field we can scale the vertical derivative of the continued field. To this end in Figure 3.18, we show the scaled field obtained using the second order vertical derivative of the upward-continued E_z and as scaling exponent 2.5 ($N/2+p/2$, where $p=2$ is the derivation order) we can see a more resolved result with a less extended spreading area.

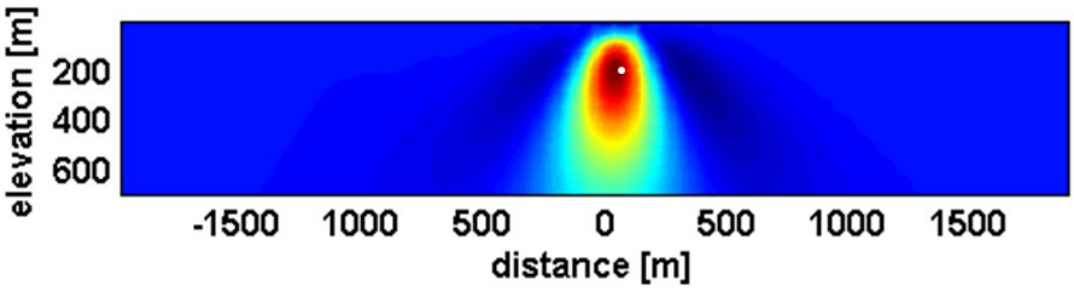

Figure 3.18: *DEXP imaged field obtained starting from the second order vertical derivative of the upward-continued field in Figure 3.15 using as scaling exponent 3.5. The white circle represents the source position.*

Unlike what happens for potential fields, we can improve the model resolution using a higher source frequency. This is a strong point of CSEM method, e.g. we can a priori determine the frequency of our signals and so choose the model resolution.

In Figure 3.19 we show the upward-continued field that we have if the fundamental frequency radiated by the transmitting antenna is 1 Hz; in Figure 3.20 we show the DEXP-scaled field obtained using 1.5 as scaling exponent, α.

As we can see from Figure 3.20, the model has a better resolution than the model in Figure 3.17 obtained using lower frequency data up to a 300 m altitude, which is the difference between δ (in this case 500 m) and the source depth (200 m). In fact, we must take into account that, while increasing the frequency, the skin-depth decreases and then the maximum depth we can detect. We saw however that DEXP introduce a better control on the resolution since we may derive the field and correspondingly increase the resolution without reducing the skin depth (compare Figures 3.18 and 3.20). This is a very suitable feature of the DEXP method.

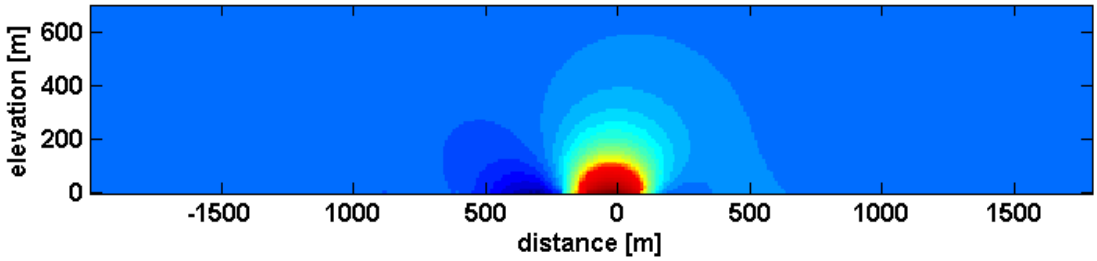

Figure 3.19: *upward continuation of the E_z component of the electromagnetic field scattered by a sphere obtained starting from the model in Figure 3.2, but considering as fundamental source frequency 1 Hz, evaluated at y=0.*

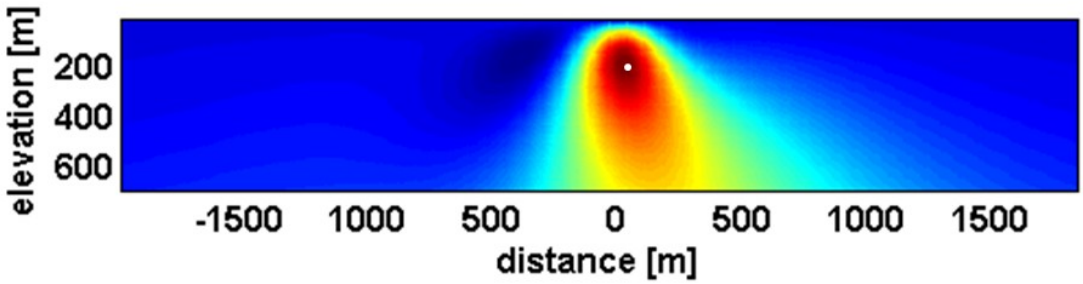

Figure 3.20: *DEXP imaged field obtained starting from the upward-continued field in Figure 3.16 using as structural index, N, 3. The white circle represents the source position.*

The control of the skin-depth on the applicability of the method is shown in Figure 3.21. In fact, in this Figure is shown the scaled field obtained starting from the upward-continued E_z component of the scattered field by a sphere as the one described above, but buried at a depth of 1000m (depth>δ) in a 1 Ωm half-space at 0.3 Hz. From the showed scaled field, we can see that the body (black cross in Figure 3.21) can't be detected; in fact the sufficient condition for detect the bodies that: $|z - z_0| \leq \delta$ where$z$ is the maximum continuation height, z_0 is the source depth and δ is the skin-depth.

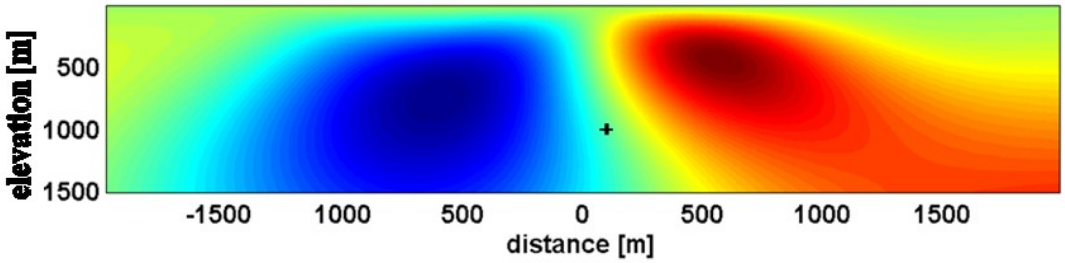

Figure 3.21: *DEXP imaged field obtained starting from the upward-continued field obtained starting from model described in Figure 3.2 but considering the anomalous source at a depth of 1000 m. The structural index is 3. The black cross represents the source position.*

The second one-point source we consider is that of the electromagnetic field scattered by a *homogeneous infinite horizontal cylinder*. The starting model used to obtain the data is the same of the one described in Figure 3.6 . The real part of the E_z component of the field at $y=0$ was upward continued, as shown in Figure 3.8.As we can see from Table 3.1 the scaling exponent, α, needed to perform the DEXP transformation of this kind of field is 1. Also in this case the exponent was estimated using the criterion of DEXP scaling function intercept (Fedi, 2007) (Figure 3.22a) on the white signed portion of the ridge in Figure 3.8. In Figure 3.22b we show the scaled field obtained starting from the continued field in Figure 3.8 and using as scaling exponent 1. The maximum of the scaled field in not perfectly located in correspondence of the body (white circle in the Figure). This comes from the polarization effect, which is not vertical, due to the position of the receiver.

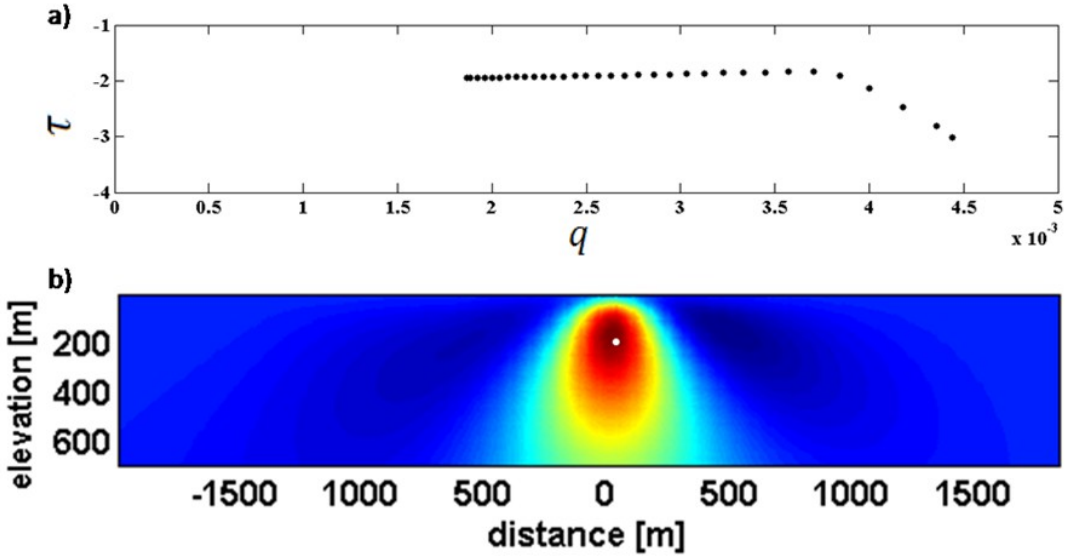

Figure 3.22: *a) estimation of the structural index obtained using the criterion of DEXP scaling function intercept (Fedi, 2007) b) DEXP imaged field obtained starting from the upward-continued E_z component of the electromagnetic field scattered by a homogeneous horizontal cylinder. The field at z=0 is obtained starting from the model in Figure 3.6. In this case was used as structural index, N, 2. The white circle represents the source position.*

As we done in the previous case, we can improve reduce the spreading area around the source deriving the continued field. In fact, as shown in Figure 3.23, representing the DEXP scaled field of the third order vertical derivative of upward-continued E_z. Scaling the derived field, the depth of the source is perfectly estimated. Instead, the horizontal position of the body in not perfectly estimated. In general when the anomaly is dipolar, the estimate of the horizontal position of the source is not straightforward with the DEXP method. The horizontal position lies, in fact, in an intermediate position with respect the minimum and the maximum of the scaled field, which, in turn depends on the position of the receiver respect the antenna. We can obtain a simplified image by applying the DEXP transformation to the modulus of the analytic signal of the continued field (Figure 3.24). We show in Figure 3.24 the scaled field at y=0 of the analytic signal of the continued field. The analytic signal in fact does not depend (or depends weakly) on the inducing field inclination and declination. Also, it has a simpler form, reducing the number of highs and lows associated to a single source. The analytic signal is a functional transformation, which permits to locate the exact

lateral position of the body because the anomaly has a form over causative bodies, that depends on the location of the body but not on the position of the receiver. The analytic signal is formed through a combination of the horizontal and vertical gradient of the field (Blakely, 1995). Starting from a 3D volume of data we get the modulus of the analytic signal from:

$$A = \sqrt{\left(\frac{\partial E_z}{\partial x}\right)^2 + \left(\frac{\partial E_z}{\partial y}\right)^2 + \left(\frac{\partial E_z}{\partial z}\right)^2} \tag{3.60}$$

When we apply the DEXP method to the analytic signal, the right structural index to use in this specific case is 3. In fact, the analytic signal of the field is built as the modulus of the first-order derivatives of the continued electric field.

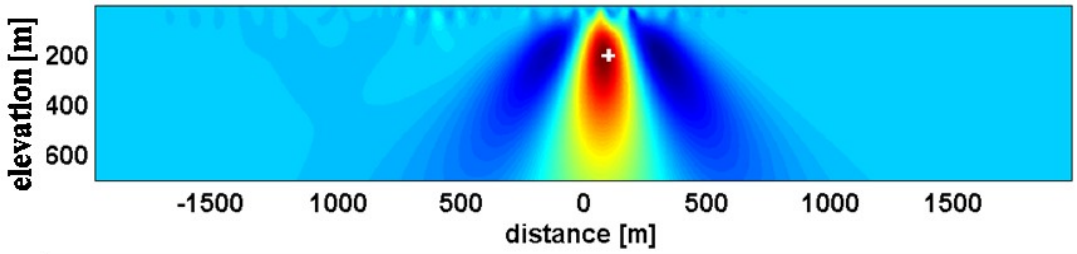

Figure 3.23: *DEXP imaged field of the third order vertical derivative of the upward-continued E_z scattered by the horizontal cylinder described in Figure 3.6. The white cross represents the source position.*

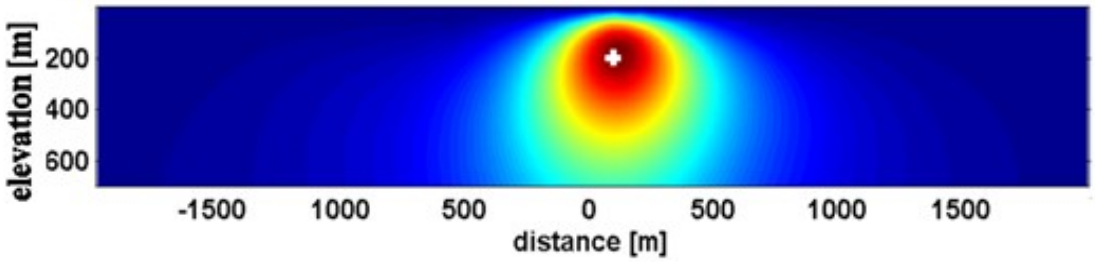

Figure 3.24: *DEXP imaged field of the analytic signal of the upward-continued E_z scattered by the horizontal cylinder described in Figure 3.6. The white cross represents the source position.*

The third and last one-point source we consider is a *semi-infinite plane* as that described in Paragraph 3.2 (Figure 3.11). Also in this case, as in the previous cases the field has been upward-continued obtaining a 3D

volume. We choose just one section of the volume (the section at y=0) to describe the case.

So, starting from the upward-continued field shown in Figure 3.13, we can obtain the DEXP-scaled field, W, multiplying the continued field by $z^{0.5}$ (equation 3.56) where 0.5 (see Table 3.1) is the scaling exponent for a sill, or a horizontal semi-infinite sheet. The structural index was estimated using the criterion of DEXP scaling function intercept (Fedi, 2007) on the white signed portion of the ridge in Figure 3.13 (Figure 3.25a).

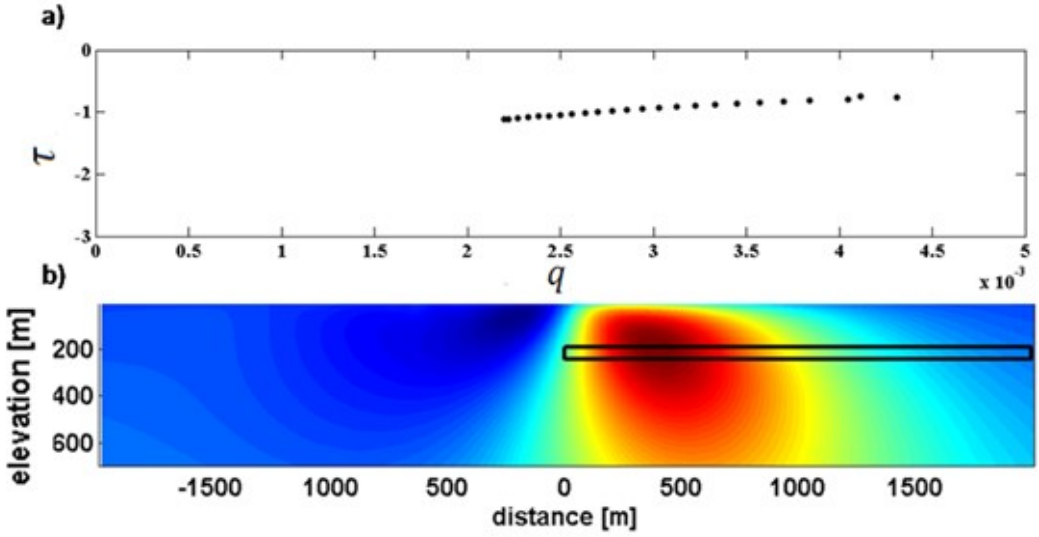

Figure 3.25: *a) estimation of the structural index obtained using the criterion of DEXP scaling function intercept (Fedi, 2007); b) DEXP imaged field obtained starting from the upward-continued field in Figure 3.13 using as structural index, N, 1.*

As we can see from Figure 3.25b, just the part of the body closest the receiver is detected by our method.

We can nevertheless have a full image of the body: we just need the data acquired by more receivers and merge the corresponding DEXP-imaged field, as we will see in Paragraph 3.3.5.

Applying the DEXP method, the depth of the source is perfectly located, but the horizontal position of the boundary of the body in not perfectly estimated and lies in an intermediate position with respect the minimum

and the maximum of the scaled field. To have a better resolution, we have valuate also the scaled field starting from the third vertical derivative of the upward-continued field showed in Figure 3.15 (Figure 3.26). As we can see from the Figure, the model has a better resolution than in the previous case, in fact the spreading area is reduced, but also in this case the horizontal position of the body is in an intermediate position with respect the minimum and the maximum of the scaled field.

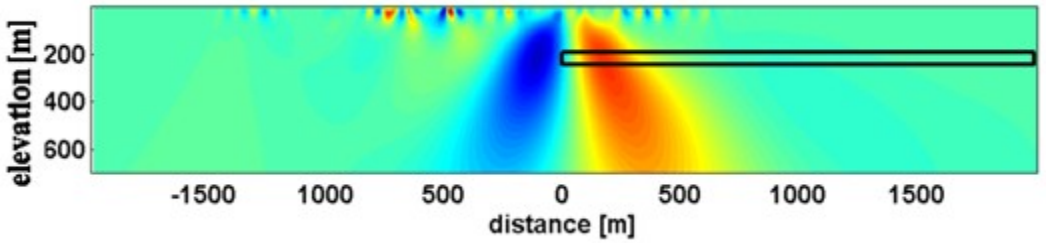

Figure 3.26: *DEXP imaged field obtained starting from the upward-continued field in Figure 3.15 using as scaling exponent 3.5.*

So, as in the infinite horizontal cylinder case, to have a more intuitive DEXP image of the portion of the body closest to the receiver, we have to consider the analytic signal of the upward continued field. We have scaled the 3D data volume of the analytic signal using as scale exponent 1 (0.5+p/2, with p=1) for the above-explained reason. The scaled field, obtained from the analytic signal using as scale exponent 1.5 is shown in Figure 3.27.

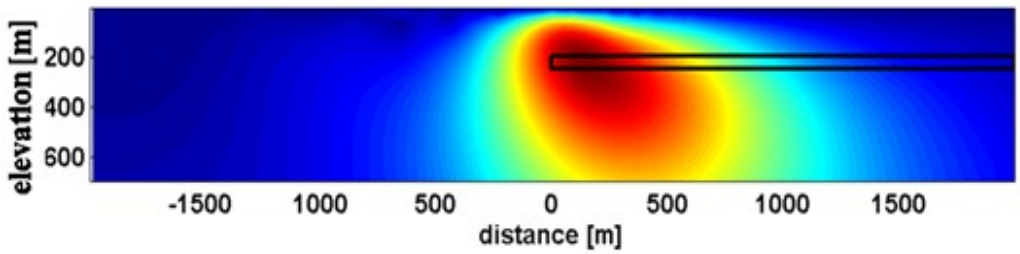

Figure 3.27: *DEXP imaged field obtained starting from the analytic signal of the upward-continued field in Figure 3.13 and using as scale exponent 1.*

The Multiridge and DEXP methods can be successfully applied to all the components of the electromagnetic field. For example, in Appendix 3 we show the results of tests conducted considering the x-component of the electric scattered field, E_x.

3.3.5 More complex bodies

Using the two methods describes above we can estimate the proper scaling exponent, α, to scale the upward-continued field. Using these two methods we can detect complex bodies which do not belong to any class of simple shape body (sphere, horizontal cylinder, thin layer), but can be viewed as a cross between these kinds of bodies. So, using these two methods, we can estimate a real number between 0 and 1.5 (using the second method we will estimate an N that is between 0 and 3 for the electric field) that will be the proper scaling exponent to use to detect the anomalous body.

Moreover, as we said in Paragraph 3.3.3, in order to have a full image of the anomalous body, we have to use the data acquired by several receivers deployed on the sea-floor and then merge the results.

In this paragraph we will show a synthetic test in which we have considered a finite (2km x 3km x 200m) resistive (0.01 Ωm) thin sheet with a thickness of 200 m buried at 150 m in a 1 Ω/m half-space (Figure 3.25). We have considered the signals acquired an array of 13 receivers spaced as shown in Figure 3.28. The antenna is a horizontal electric dipole (HED) 150 m long and emits a signal with a fundamental frequency of 0.3 Hz. The antenna is towed by a ship in x and y direction and is located at a height of 30 m from the sea-floor. The offset (distance antenna-receiver) varies with a step of 10 m in both x and y directions.

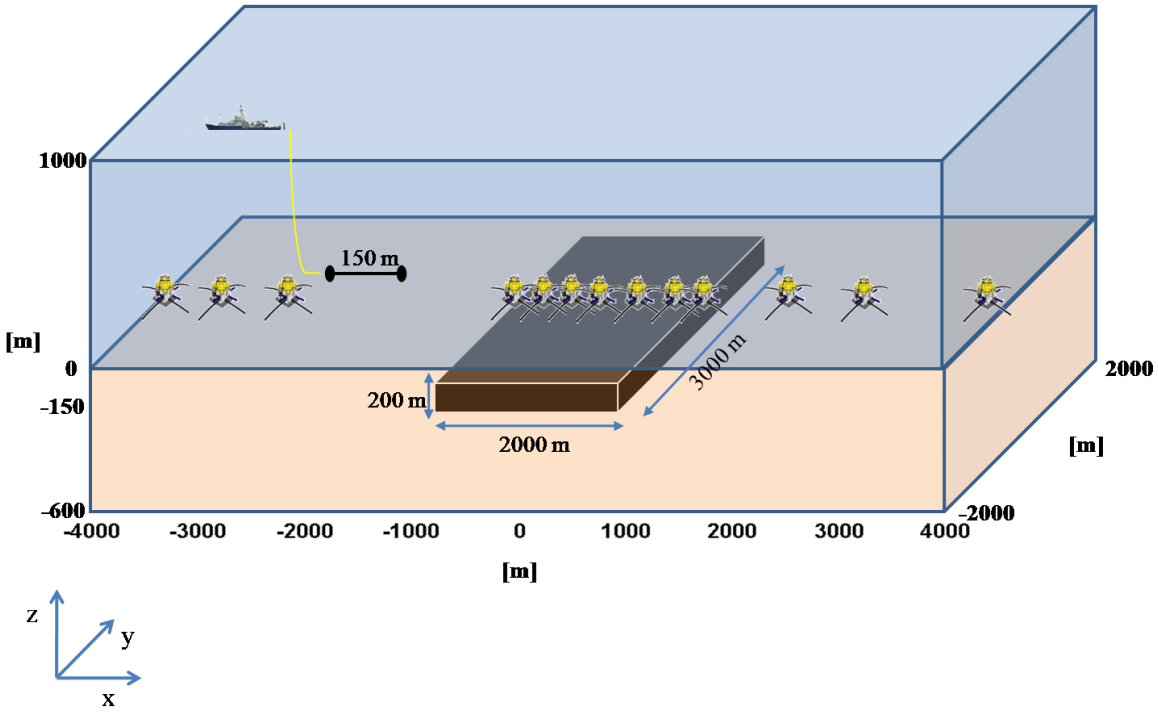

Figure 3.28: *starting model for a thin sheet used to solve the forward problem.*

Then, we have considered the signals at each receiver and we have used them to have a full image of the anomalous body. In particular, we have considered the electric field scattered by the resistive body at each receiver. It is obtained subtracting to the field simulated starting from the model in Figure 3.28 the field that we have is there is not any resistive body buried in the half-space.

In Figure 3.29 is shown the real part of the component E_z of the scattered field acquired by the receiver positioned at P (-4000, 0, 0).

The fields at each receiver are upward-continued using the continuation algorithm working in frequency domain until a elevation of 700 m (less than skin-depth to stay in the near field zone). As done also in the previous cases, to avoid problems linked frequency-aliasing errors which can arise performing upward continuation in frequency domain, the input data sequences are extended to a greater length by mathematical extrapolation using zero-padding.

To better locate the lateral position of the resistive body, is applied the DEXP transformation to the analytic signal of the continued fields at

each receiver. In Figure 3.30*a,….,o* are shown the analytic signals of the continued fields at each receiver evaluated at *z=0*.

The obtained 3D data volumes have been scaled using the scaling exponents (α) estimated for each signal using the methods described above.

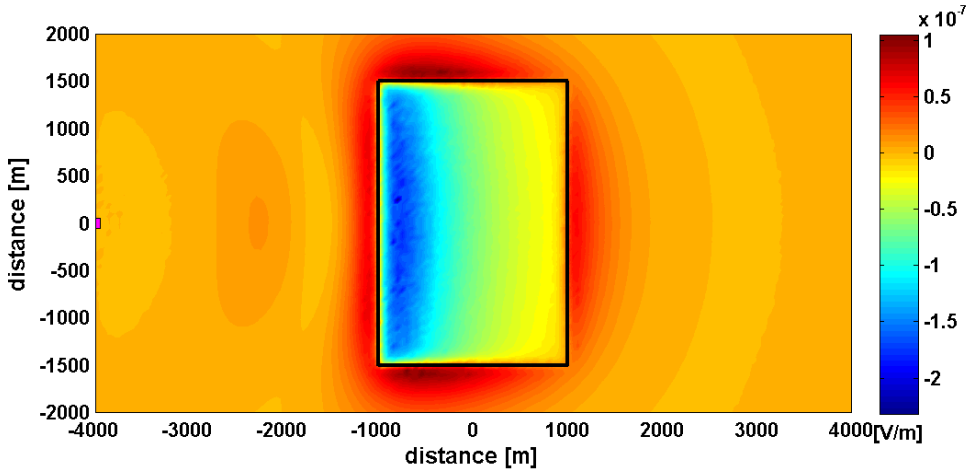

Figure 3.29: *real part of the component E_z of the scattered field acquired by the receiver positioned at P (-4000, 0, 0) in Figure 3.28.*

As we can see from the Figures 3.30*a,…,o*, the shape of the anomaly changes varying the receiver position. In particular, the maximum values of the fields are located in correspondence of the portion of the body closest the receivers. When the receiver is above the anomalous body, the maximum area of the DEXP image is focused in correspondence of the receiver because the greatest contribute to the field comes from that portion of the anomalous body, which is the closest to the antenna.

For this reason also the structural index, *N*, will change varying the receiver position. In fact, when the receiver is above the body (Figure 3.30*d,..,l*) the analytical signal anomaly is similar to that due to a buried concentrated source distribution, e.g., similar to that of a resistive sphere. We then expect a structural index estimate of about 3. Instead, when the receiver is located outside the resistive body the expected structural index estimate is about 1 ($0.7<N<1.4$)

because the anomaly is there more similar to that of a thin infinite layer (Figures 3.31 a; b).

In Figure 3.32*a,….,o* the scaled fields *W*, computed using the estimated scaling exponents, are shown; in particular, to have a better understanding of the images we show the sections of the scaled fields at each receiver and at *y=0*.

Then, to have a meaningful image of the anomalous body, we have merged all the results representing only the maximum of each scaled field in the same plot (Figure 3.33). As we can see from Figure 3.33, in this way we can estimate the exact position and extension of the anomalous resistive body.

Unfortunately, note that this whole picture cannot completely be seen on real data, because the signal is typically saturated in correspondence of the receiver (at zero off-set). So, we cannot evaluate the scattered field in correspondence of the receiver. However, in real cases, we can consider the scattered field only at positive offsets, at distances from the receiver greater than the dimension of the saturation zone of the signal.

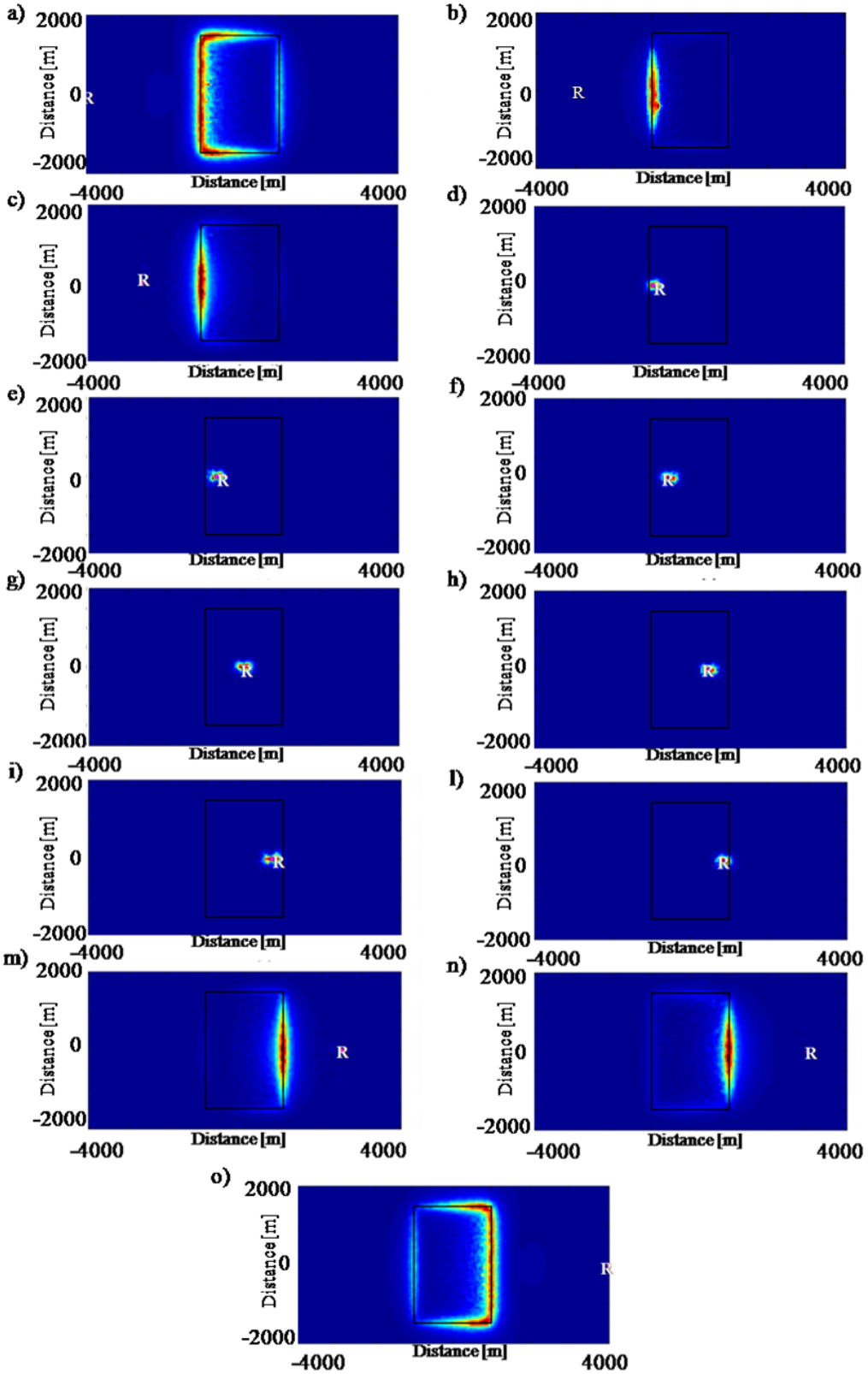

Figure 3.30: *analytic signal of the continued fields at each receiver evaluated at z=0. R denotes the receiver position.*

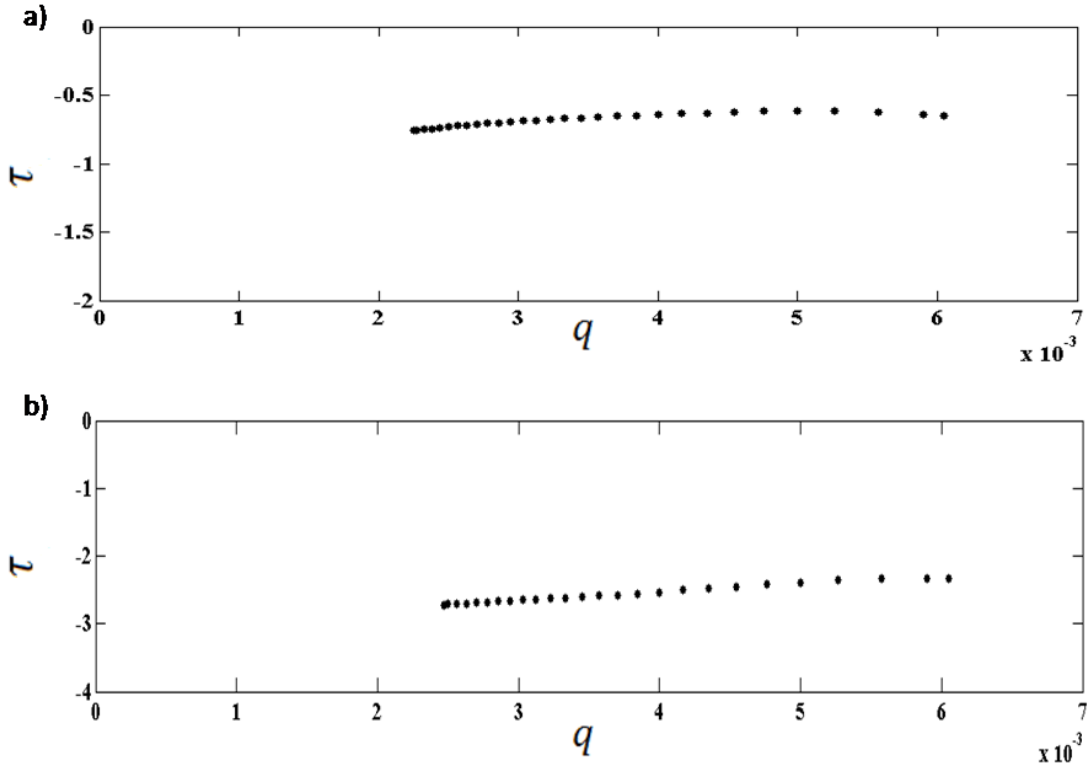

Figure 3.31: *Structural index, N, estimated using the criterion of DEXP scaling function intercept (equation 3.61). a) from the ridges obtained considering the real part of the E_z component when the receiver is at P (-4000, 0, 0); b) from the ridges obtained considering the real part of the E_z component when the receiver is at P (-300, 0, 0).*

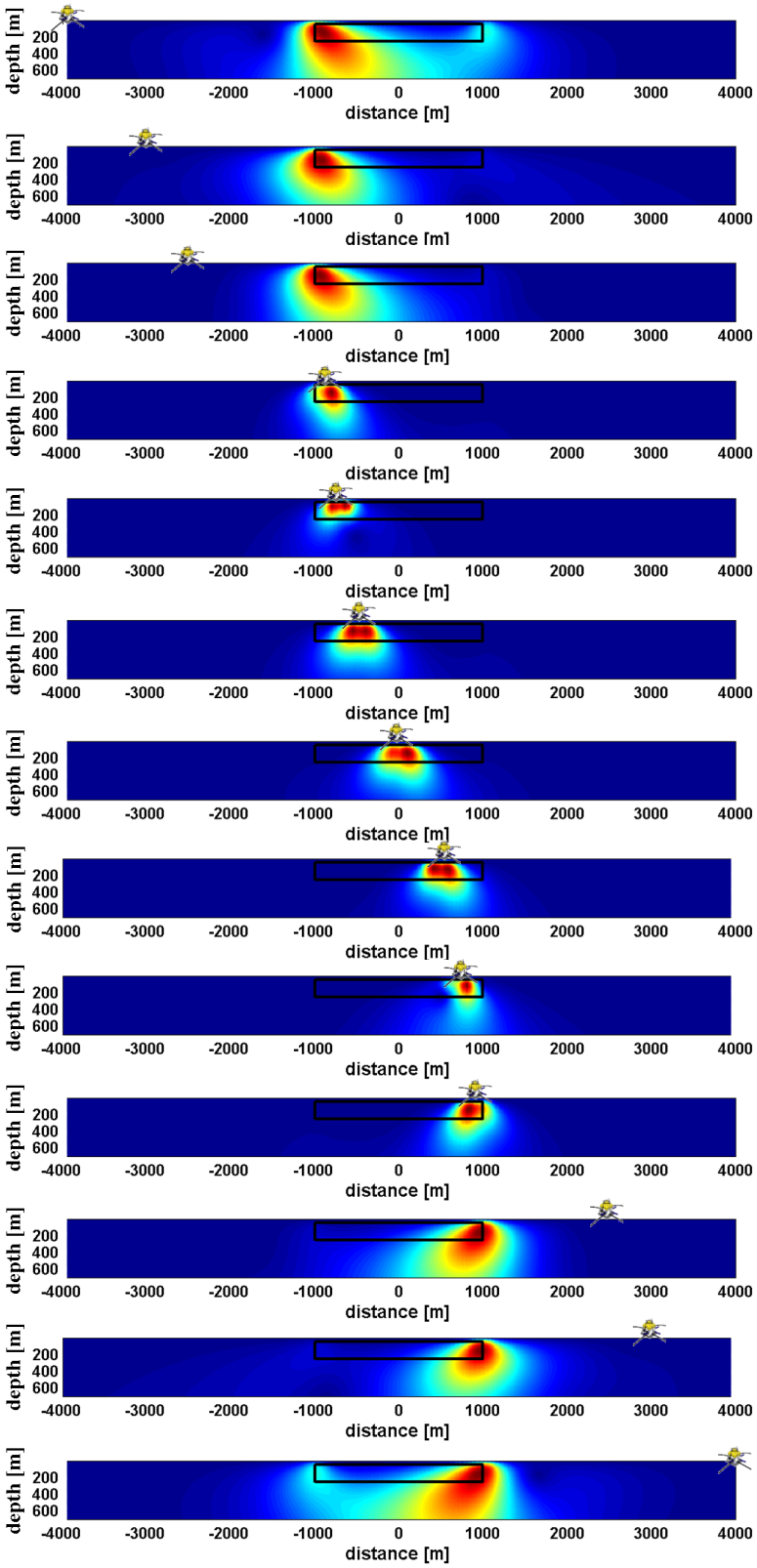

Figure 3.32: *DEXP image sections evaluated at each receiver at y=0, W. The scaling exponents were estimated through equation 3.61 before each DEXP transformation (equation 3.56).*

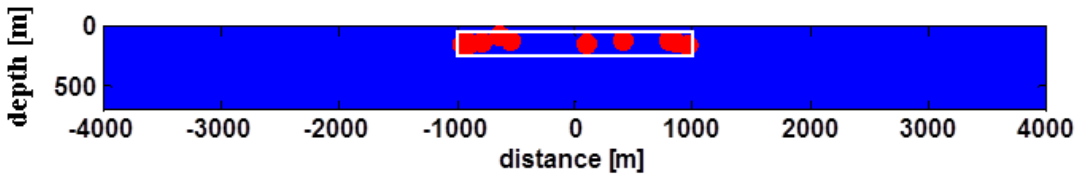

Figure 3.33: *Maxima of the DEXP transformed fields represented in Figure 3.31.*

3.4 Application to real data.

The Multiridge and DEXP methods was tested on a real dataset kindly made available by eni e&p.

The method was applied on data acquired in a well-known complex exploration area where mCSEM method was used to help define the hydrocarbon distribution in narrow and elongated fault compartments with thin stacked reservoir sandstones. The area was previously explored by extensive 2D and 3D seismic campaigns and by wells penetrating hydrocarbon-bearing rocks of Late, Middle and Early Triassic ages (Dell' Aversana, 2012). The area is characterized by the presence of many faults cutting a roll-over structure and a boundary fault. The water depth varies from 260m to 440mand the seabed has a smooth topography.

Although the area was widely explored, there are still uncertainties related to the extent of the accumulation, which depends on the sealing properties of the bounding faults, and the faults inside the roll-over structure.

As we can see from the seismic section in Figure 3.34 (Dell' Aversana, 2012), the area is characterized by the presence of two overlapped reservoir at a depth from the seafloor of about 800 m and 1500m respectively. In particular, the seismic section in Figure 3.34 is the pre-stack depth migration (PSDM) section along line, the blue line in Figure 3.33.

The data was acquired by 83 CSEM receivers deployed along six lines (Figure 3.35) with two fundamental frequencies: 0.5Hz and 0.15Hz. The antenna (a horizontal electric dipole) is towed by a ship in direction of

each-line and we consider at each receiver the in-line component of the electric field.

We study the field in the direction in-line with the transmitter dipole antenna because in this case the electric field lines are purely radial and plunge into the seafloor with a significant vertical component. The associated currents can be interrupted by tabular resistors such as reservoirs, producing a galvanic distortion of the electric field. This will be visible on the seafloor as increased electric field amplitude. Instead, in the direction broadside to the transmitter, electric fields are purely azimuthal and largely horizontal, and will not produce a galvanic response to horizontal boundaries. This results in a large difference in sensitivity between the radial and azimuthal geometries to thin resistive layers. This result was noted in a 1984 proposal submitted to 14 oil companies by Scripps; the authors examined a buried resistive layer model and concluded, “It is the TM mode of the experiment which is most sensitive to resistive structure. This makes the choice of transmitter geometry most important” (Constable, 2010).

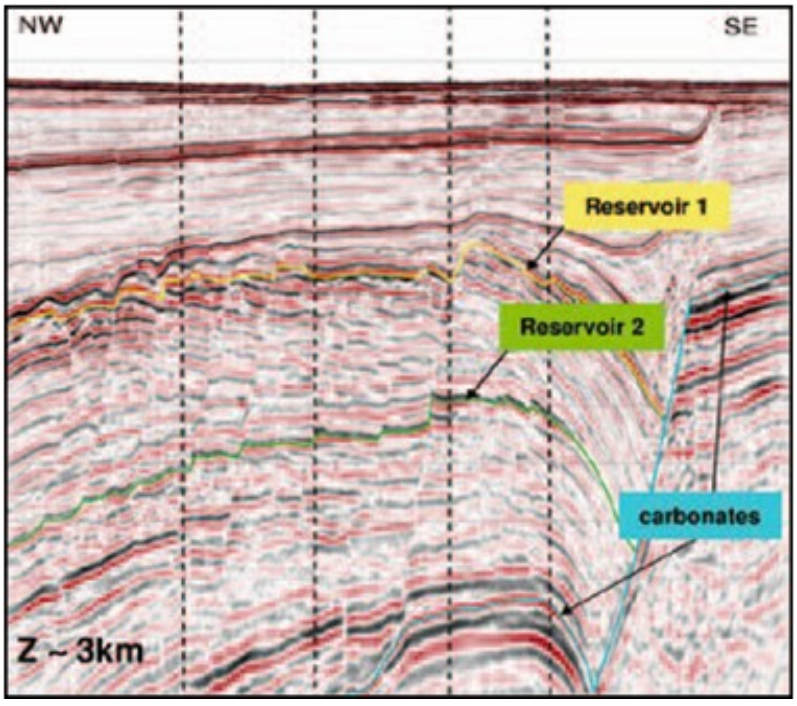

Figure 3.34: *Seismic section acquired along the blue profile in Figure 3.33 (Dell’ Aversana, 2012).*

The offset (distance antenna-receiver) varies with a step of 100 m.

Receiver noise is very low because cultural and MT noise is highly attenuated in the CSEM frequency band (Constable, 2007).

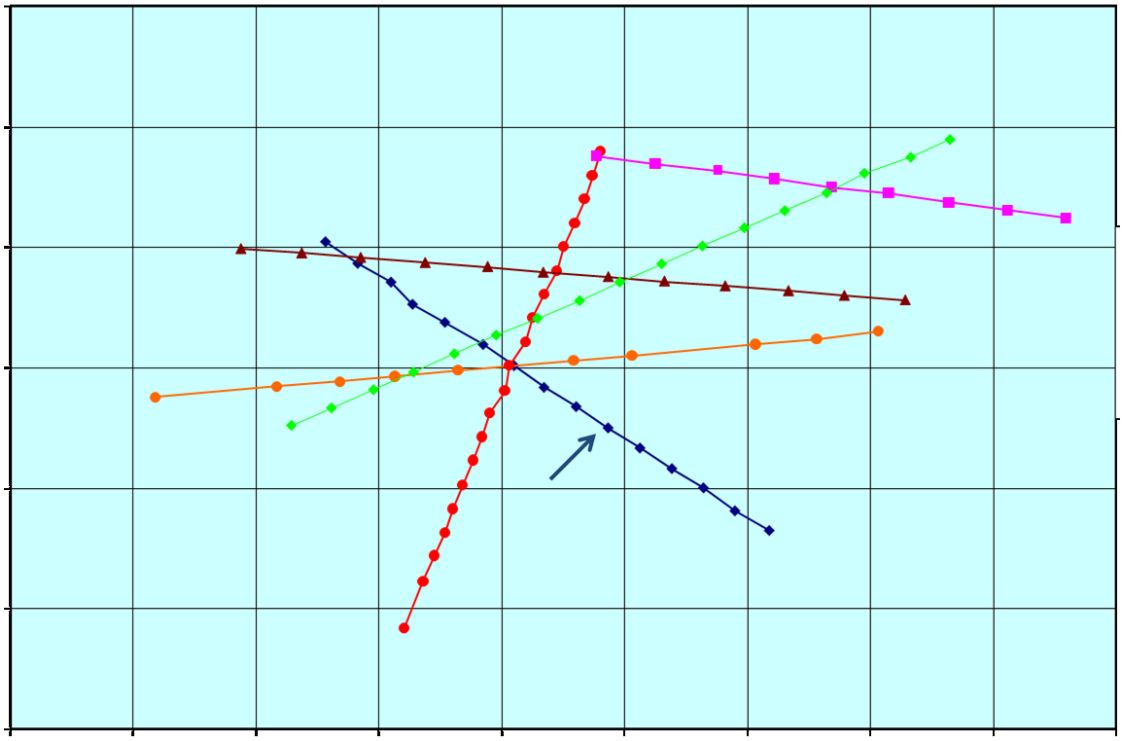

Figure 3.35: *Survey layout.*

We have considered the curves representing the amplitude and the phase of the in-line (radial) component of the electric field at each off-set in semi-logarithmic scale (MVO and PVO curves) evaluated at each receiver for both frequencies 0.5 Hz and 0.15 Hz. Then, to have the signal due to the resistive anomalous buried body, we have chosen a reference signal, that is the signal acquired in a portion of the survey area far to the anomalous body, and we have subtracted it to the acquired signals. In Figure 3.36 is shown one of the MVO curve acquired (blue signal). As we can see, the signal saturates at off-sets $\simeq 0$, so we must consider the signal at off-set > 0 or at off-sets < 0. In the same Figure is shown the MVO curve of the reference signal used to obtain the scattered field (green curve in Figure 3.36). Comparing the two MVO curves in Figure 3.36 we can see that the values of the radial electric

field of the blue MVO curve are higher than the values of the radial electric field of the reference signal; it means that, probably, there is an anomalous resistive body located in correspondence of the maximum difference between the two signals.

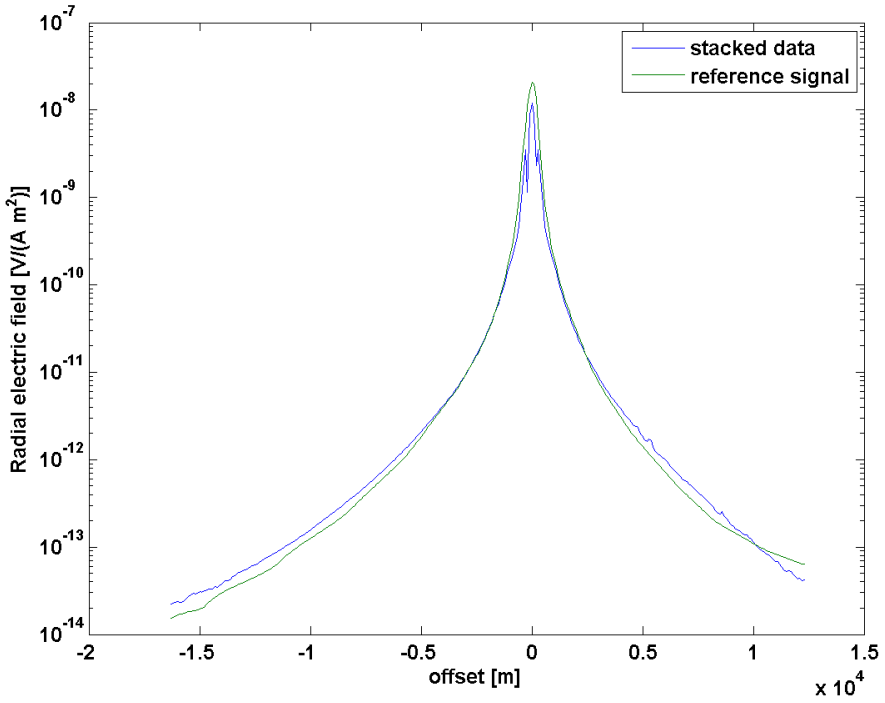

Figure 3.36: *The blue MVO is the signal acquired by a receiver deployed along the blue line, the green MVO is the reference signal.*

We have subtracted to the signals acquired at each receiver, the reference signal. In particular, was considered two reference signals one at 0.15 Hz and one at 0.5 Hz.

Then, from amplitude and phase of the scattered radial electric field we have obtained the real part and the imaginary part of the scattered radial electric field evaluated at each receiver.

The real and imaginary parts of the radial component of the electric field (E_r) have been upward-continued until a height less than skin-depth.

Hence, the Multiridge method was applied on the absolute value of the E_r upward-continued field, to have a preliminary estimation of the sources position.

In particular, according to what required by the Multiridge and DEXP analysis shown in the previous section, the real and imaginary parts of the radial component of the electric field (E_r) was upward-continued up to an altitude less than skin-depth. For the typical formation rock resistivity present in the area of study, the skin depth for the 0.5 frequency may be evaluated as about 1.5 km and for 0.15 Hz as about 2.5 km. In this case, since the data was acquired along profiles (we do not have a matrix of data at each receiver), we used a 1D upward continuation algorithm. Using a 1D upward-continuation algorithm we are assuming that the body is infinite in the direction orthogonal to the profile, but we can recognize the three-dimensional shape and position of the anomalous bodies as well, because we use the data acquired along lines directed in several orientations.

In Figure 3.37d we show an example of the application of the Multiridge method to the data acquired by the receiver indicated by the arrow in Figure 3.35, for a 0.15 Hz frequency. In particular, we have applied the method to the second order vertical derivative of the scattered radial electric field (E_r), obtained subtracting to the total field a reference signal (Figure 3.36) that is the signal acquired by a receiver deployed far from the source of the anomaly. Therefore, as described in the Paragraph 3.2, we have evaluated, starting from the second order vertical derivative of the upward continued E_r, the ridges using the Canny's method (Figure 3.37d). The blue ridges are referred to the zeros of the third order vertical derivative of the field shown in Figure 3.37a. As seen in Paragraph 3.2, just a portion of each ridge is a straight line, but, extending the ridges downward, we have demonstrate that these ridges intersecting at the point x_0, z_0, which is the location of the part of the anomalous body closest to the considered receiver.

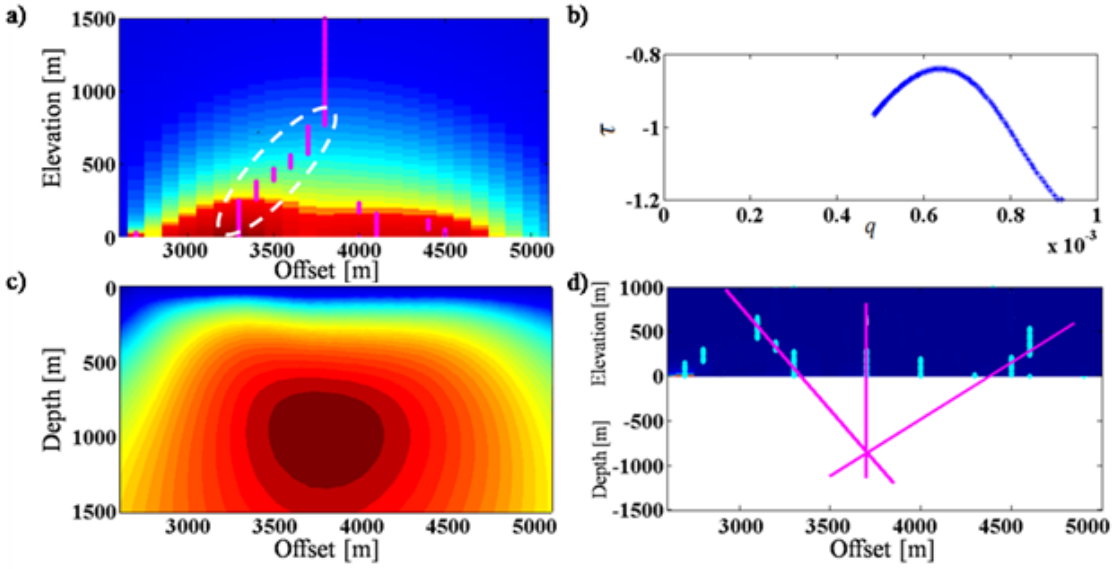

Figure 3.37: *a) Absolute value of the upward-continued E_r component of the scattered field, acquired by the receiver indicated by the arrow in Figure 3.36, and obtained subtracting to the acquired signal a reference signal acquired by a receiver far from the source. The dotted white line represent the portion of ridge considered to estimate the structural index, N. b) Structural index, N, estimated using the criterion of DEXP scaling function intercept (equation 3.61).c) DEXP imaged field obtained using as structural index the structural index estimated and shown in Figure 3.37c. d) Application of the Multiridge method to the absolute value of the second order vertical derivative of the upward-continued E_r component of the scattered field, acquired by the receiver indicated by the arrow in Figure 3.35.*

We have then continued the fields measured at each receiver and at both frequencies, and scaled them using the structural indices, *N*, estimated using the criterion of DEXP scaling function intercept (equation 3.61), along selected ridges. In Figure 3.37*a,b,c* we apply the DEXP method to the 0.15 Hz data acquired by a receiver, indicated by the arrow in figure 3.6. In particular, in Figure 3.37a we show the absolute value of the upward-continued scattered field, obtained by subtracting, to the data acquired by the receiver indicated by the arrow in Figure 3.35, the signal acquired by a far receiver, sited in an area characterized by higher resistivity. Moreover, in the same figure, we show the ridges obtained joining the zeros of the first order vertical derivative of the field. Instead, in Figure 3.37c we show the DEXP imaged field obtained scaling the field in Figure 3.7a using the structural index estimated as shown in Figure 3.37b, using equation 3.61.

The DEXP method, was then applied to all the signals acquired during the survey. In general, the values of the scaling exponents are between 0.9 and 1.5, so the anomalous body is comparable to a relatively thin layer, a shape well in agreement with the oil reservoirs represented in the seismic section (Figure 3.34). Since, as widely demonstrated in the previous paragraph, from a single signal we can see only the part of the anomalous body closest the receiver, to have a full view of the anomalous body we have merged all the results evaluated for each receiver and for each frequency. So, as we done in the synthetic case showed in the previous paragraph we represent the maxima values of each scaled field to have a meaningful image of the anomalous resistivity distribution. The result obtained starting from the data acquired by the receivers deployed in correspondence of the blue dots along the blue line in Figure 3.35 is shown in Figure 3.38. In particular the blue dots represent the maxima of the scaled field at each receiver for the frequency 0.15 Hz and the white dots represent the maxima of the scaled field at each receiver for the frequency 0.5 Hz. In Figure 3.38 is shown also the comparison between the obtained result and the resistivity section obtained by 3D anisotropic inversion of CSEM data for the same profile published by Dell' Aversana (2012).The horizontal gaps between the resistors present in the Figure were not estimated as an inversion results but was highlighted with the asymmetry method developed by Dell' Aversana (2010). As we can see, in this case using the DEXP method we have meaningful information about the location and the extension of the upper reservoir and have just a point located in correspondence of the lower reservoir. But as we can see from the inversion results the resistivity contrast of the lower reservoir is very small and we detect the part of the lower reservoir showing the maximum resistivity contrast with the surrounding rocks.

Is very important to consider that the results obtained using 3D inversion were obtained using very strong constraints coming from seismic and well data. Conversely, our results are obtained without using any constraint and *a priori* information. This shows the usefulness and high potential of the method developed in this thesis, namely the DEXP analysis of electromagnetic fields in the CSEM framework.

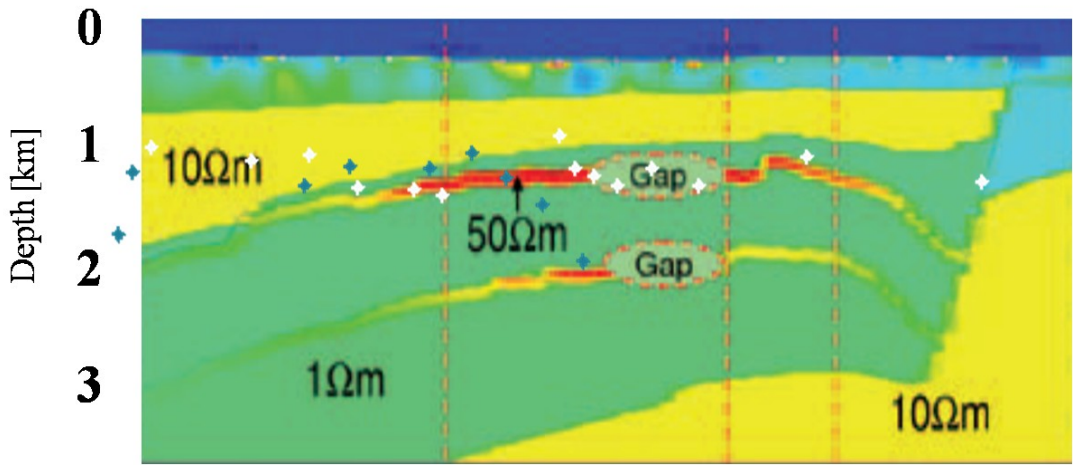

Figure 3.38: *the blue and white dots represent the maxima of the DEXP transformed fields obtained from the data measured by the receivers positioned along the blue line in Figure 3.33 for a fundamental source frequency of 0.15 Hz and 0.5 Hz respectively. The Figure in background is the result of the 3D anisotropic inversion (Dell'Aversana, 2012).*

The DEXP method has been also applied to all the data acquired at each receiver at both frequencies (0.5 Hz and 0.15 Hz) yielding similar very meaningful results. Unfortunately we have not the possibility to access to the inversion-based interpretation along the other profiles, so that we cannot compare with them our results. However we obtained results comparable to those shown in Figure 3.39, that is we localized resistors at similar depths for each profile. And, once again, we obtained depth estimates generally higher in the 0.15 Hz case. The zero-altitude is the sea-floor level.

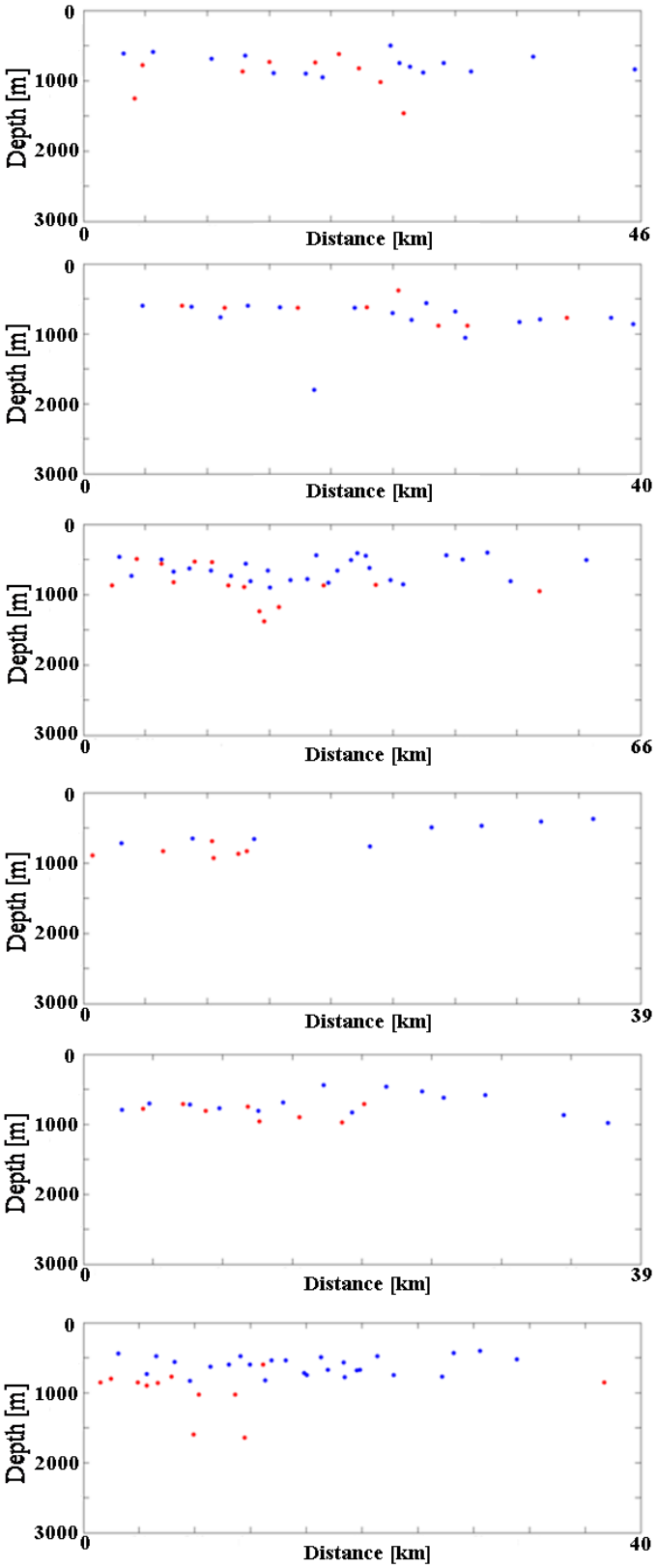

Figure 3.39: *results obtained applying the DEXP method to all the signals acquired during the survey described in the paragraph. The red dots represent the results*

obtained from data acquired with a fundamental frequency of 0.15Hz; the blue dots represent the results obtained from data acquired with a fundamental frequency of 0.5 Hz.

In Figure 3.40 we show, finally the obtained result for the whole survey.

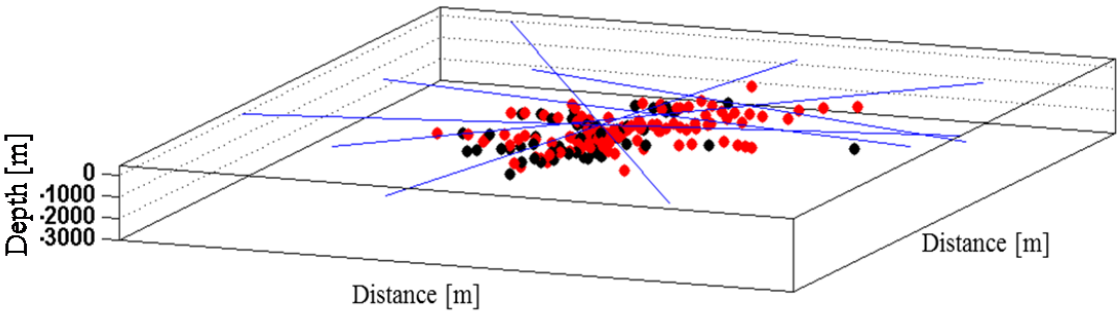

Figure 3.40: *the red and black dots represent the maxima of the DEXP transformed fields obtained from the data measured all the receivers in Figure 3.33 for a fundamental source frequency of 0.15 Hz and 0.5 Hz respectively.*

Conclusions

During my PhD I have developed two methods for a fast interpretation of marine Controlled Source Electro-Magnetic (mCSEM) data.

mCSEM sounding is an electromagnetic method which uses the low frequency (0.1 Hz 10 Hz) signal emitted by an antenna (generally a horizontal electric dipole (HED)), towed by a ship near the sea-floor, to get information about the resistivity distribution beneath the sea-floor. The electro-magnetic field is received by an array of electric and magnetic receivers deployed on the sea-floor. So, this kind of sounding is an useful support tool to other geophysical methods to detect and monitoring oil and gas reservoirs located beneath the sea-floor. In fact, the oil and gas reservoirs show higher values in resistivity than the surrounding rocks.

Generally, for the interpretation of the mCSEM data inversion methods are used, requiring high computational cost and very strong constraints to get reasonable and potentially unique results. Here we have proposed two fast and low computational-cost methods (to use as they are or even before using inversion methods), which have the great advantage of not requiring any *a-priori* information, and proved that they may give us very useful information about the resistivity distribution.

The first proposed method is the “Singular Function Normalization” (SFN). As we have seen in Chapter 2 the SFN method is a fast and low computational cost method for the interpretation of marine controlled source electromagnetic data, based on the quantitative analysis of the MVO curves. MVO represents the observed amplitude of the in-line electric field component versus offset (the distance between the source and the receiver) in a semi-logarithmic scale. As well known, and also shown in Chapter 2, the MVO shape is strictly linked to resistivity

distribution. I propose a new method of analysis, based on determining, on the MVO curves, the best-fit estimation of the exponent coefficients of the exponential singular functions and of the exponents of the Lipchitz singular function. We selected these functions since they may be considered a good approximation of the MVO curves relative to the simplest case of the half-space, which is in fact singular at the zero-offset. Being the behaviour of the MVO branches dependent on the local resistivity distribution, the estimated parameters in the exponents of these singular functions can give information about the horizontal location of buried resistive bodies. So, this method represents a fast and computationally low-cost way to have 2D maps showing areas with the lowest value of drilling risk.

We demonstrated the good performance of the SFN method for both a synthetic and a real dataset, this last kindly made available by eni e&p. The results obtained from the test on real data show a good correspondence with the well logs and the results obtained by Dell'Aversana (2012) for the same area.

The second proposed method is based on the multiscale approach of the Multiridge analysis (Fedi et al., 2009) and of the "Depth from Extreme Points" method (DEXP; Fedi, 2007). These methods were for the first time applied, in this thesis, to low frequency electromagnetic data. These method get information about the depth and the location of the resistive buried sources and the DEXP gives also information about a characteristic parameter of the sources, the structural index *N,* which is linked to the shape of the source, as shown in Chapter 3. The most important feature of these multiscale methods is that this information is extracted from the data without any *a priori* information. The DEXP method was originally developed for the interpretation of static fields, such as gravity and magnetic field. Here we have shown that is possible apply this method also to low-frequency electromagnetic data. The DEXP and the Multiridge methods are based on the evaluation of the field at altitudes higher than the measurement altitudes (upward-continuation). This task is not simple for the electromagnetic field. However, I have shown that is possible to use the upward-continuation algorithm also for non-static low-frequency fields, under the assumption

that the distance from the source has to be less than the skin-depth δ. I tested the method on synthetic data, related to simple models, such as an uniform resistive sphere buried in a half-space or an infinite horizontal cylinder buried in a half-space, and on more complex models such as a horizontal finite thin resistive layer buried in a half-space.

From this analysis we see that there are significant differences between the DEXP method applied to low-frequencies electromagnetic data and the application of the DEXP method to potential field data. The main difference is that the scattered field is strongly influenced by the receiver positions with respect the transmitter, which in turn determines the polarization direction and intensity for each receiver. However, for each profile (with a transmitter and an array of receivers), the portion of the body closest to the transmitter is energized much more than the external parts, so that we can assume there an approximately uniform polarization of constant intensity. Instead, for static fields, as occurs in the magnetostatic case, we may assume that the polarization is uniform in direction and has a nearly constant intensity for the whole source in the crust. For a typical CSEM survey this means that we must consider each profile separately, since each of them is relative to a different position of the transmitter. But, the interesting thing is that merging the results obtained for each transmitter position, we can very well define the position and the shape of the whole resistor, as shown in Figures 3.32 and 3.33.

One more striking feature of the DEXP method for EM fields, as described in Paragraph 3.3.5, is that the structural index is naturally linked to the transmitter and receivers positions. To this end, we have shown the case of a thin resistive sheet. When the transmitter is located close to the resistor we obtain N=3 as structural index, that is the structural index of a sphere, being the part of the source mostly lightened very concentrated. Instead, when we are far from the resistor the structural index is around 1 ($0.7<N<1.4$) because the scattered field anomaly is there more similar to that of a thin infinite layer. The whole picture is clear when looking at figures 3.30 and 3.31.

Finally, I applied the method to the real data-set made available to us by eni e&p. The DEXP imaged results were compared with the results obtained using anisotropic 3D inversion and showed a very good accord with them, when compared along a recently published interpreted section.

References

Abubakar, A., T.M.Habashy,V. L. Druskin, L.Knizhnerman, and D. Alumbaugh, 2008, 2.5D forward and inverse modeling for interpreting low frequency electromagnetic measurements: *Geophysics*, **73**, no. 4, F165–F177.

Akin J.E., 2005, Finite element analysis with error estimators: Butterworth-Heinemann Ltd

Amundsen, L., L. Løseth, R. Mittet, S. Ellingsrud, and B. Ursin, 2006, Decomposition of electromagnetic fields into upgoing and downgoing components: *Geophysics*, **71**, no. 5, G211–G223.

Andréis D., L. MacGregor, 2008, Controlled-source electromagnetic sounding in shallow water: Principles and applications, *Geophysics*, **73**, no.1, F21-F32.

Bannister, P. R., 1968, Electromagnetic fields within a stratified earth produced by a long horizontal line source: *Radio Science*, **3**, 387–390.

Bannister, 1984, New simplified formulas for ELF subsurface-to-subsurface propagation: IEEE Journal of Oceanic Engineering, **OE-9**, 154–163.

Blakely R..J., 1995, Potential theory in gravity and magnetic applications, Cambridge University Press.

Bostick, F. X., Jr., 1977, A simple almost exact method of MT analysis: Proceedings ofthe UniversityofUtah Workshop on Electrical Methods in Geothermal Exploration, 175-188.

Brown V., M. Hoversten, K. Key and J. Chen, 2012, Resolution of reservoir scale electrical anisotropy form marine CSEM data: *Geophysics*, **77**, no.2, E147-E158.

Canny, J., 1986, Acomputational approach to edge detection: IEEE Transactions on Pattern Analysis and Machine Intelligence, **8**, 679–698.

Chave, A. D., S. C. Constable, and R. N. Edwards, 1991, Electrical exploration methods for the seafloor, *in* M. Nabighian, ed., Electromagnetic Methods in Applied Geophysics, 2: SEG, 931–966.

Chave, A. D., and C. S. Cox, 1982, Controlled electromagnetic sources for measuring electrical conductivity beneath the oceans: Part 1 — Forward problem and model study: *Journal of Geophysical Research*, **87**, B7 5327–5338.

Clavaud J.B, 2008,Intrinsic electric anisotropy of shale: the effect of compaction;*Petrophysics,***49**, 243–260.

Commer, M., and G. A. Newman, 2008, New advances in three-dimensional controlled-source electromagnetic inversion: *Geophysical Journal International*, **172**, no. 2, 513–535.

Constable S. C., 2010, Ten years of marine CSEM for hydrocarbon exploration: *Geophysics*, **75**, no. 5, A67-A81.

Constable, S., and C. S. Cox, 1996, Marine controlled source electromagnetic sounding 2: The PEGASUS experiment: *Journal of Geophysical Research*, **101**,B3 5519–5530.

Constable S. C., L. J. Srnka, 2007, An introduction to marine controlled-source electromagnetic methods for hydrocarbon exploration: *Geophysics*, **72**, no.2, WA3-WA12.

Constable, S., and C. J. Weiss, 2006, Mapping thin resistors and hydrocarbons with marine EM methods: Insights from 1D modeling: *Geophysics*, **71**, no. 2, G43–G51.

Cox, C. S., 1981, On the electrical conductivity of the oceanic lithosphere: *Physics of the Earth and Planetary Interiors*, **25**, 196–201.

Cox, C. S., S. C. Constable, A. D. Chave, and S. C.Webb, 1986, Controlled source electromagnetic sounding of the oceanic lithosphere: *Nature*, **320**, no. 6057, 52–54.

Darnet, M.,M. C. K. Choo, R. Plessix, M. L. Rosenquist, K. Yip-Cheong, E. Sims, and J. W. K. Voon, 2007, Detecting hydrocarbon reservoirs from CSEM data in complex settings: Application to deepwater Sabah, Malaysia: *Geophysics*, **72**, no. 2,WA97–WA103.

Dell' Aversana P., 2007, Improving interpretation of CSEM in shallow water: *The leading edge*, **26**, 332-335.

Dell' Aversana P., 2010, Accurate detection of resistivity anomalies using symmetry attribute and inversion of marine CSEM data: *The leading edge,* **29**, 662-668.

Dell' Aversana P., Colombo S., Ciurlo B., Leutscher J., Seldal J., 2012, CSEM data interpretation constrained by seismic and gravity data: an application in a complex geological setting: *First break*, **30**, 43-52.

Edwards, R. N., 1997, On the resource evaluation of marine gas hydrate deposits using sea-floor transient electric dipole-dipole methods: *Geophysics*,**62**, 63–74.

Ellingsrud, S., T. Eidesmo, S. Johansen, M. C. Sinha, L. M. MacGregor, and S. Constable, 2002, Remote sensing of hydrocarbon layers by seabed logging (SBL): Results from a cruise offshoreAngola: *The Leading Edge*, **21**, 972–982.

Eidesmo, T., S. Ellingsrud, L. M. MacGregor, S. Constable, M. C. Sinha, S. Johanson, F. N. Kong, and H.Westerdahl, 2002, Sea bed logging (SBL), a newmethod for remote and direct identification of hydrocarbon filled layers in deepwater areas: *First Break*, **20**, 144–152.

Ellis, M., R. Evans, D. Hutchinson, P. Hart, J. Gardner, and R. Hagen, 2008, Electromagnetic surveying of seafloor mounds in the northern Gulf of Mexico*: Marine and Petroleum Geology*, **25**, no. 9, 960–968.

Ellis M.H., Sinha M.C. and Parr R., 2009, Investigations into the discrepancies between electromagnetic and borehole derived resistivitiesin overburden sediment: 71st EAGE meeting, Amsterdam, the Netherlands, Expanded Abstracts.

Evans, R. L., 2007, Using CSEM techniques to map the shallow section of seafloor: From the coastline to the edges of the continental slope: *Geophysics*, **72**, no. 2, WA105–WA116.

Everett M.E. and Constable S.C., 1999, Electric dipole fields over an anisotropic seafloor: theory and application to the structure of 40 Ma Pacific Ocean lithosphere:*Geophyscial Journal International* **136**, 41–56.

Everett, M. E., and R. N. Edwards, 1993, Transient marine electromagnetics: The 2.5-D forward problem*: Geophysical Journal International*, **113**, 545– 561.

Fedi M, and G. Florio, 2006, SCALFUN: 3D analysis of potential field scaling function to determine independently or simultaneously Structural Index and depth to source: SEG Annual meeting.

Fedi M., 2007, DEXP: A fast method to determine the depth and the structural index of potential field sources: *Geophysics*, **72**, no. 1, I1-I11.

Fedi M., G. Florio, T. Quarta, 2009, Multiridges analysis of potential fields: Geometric method and reduced Euler deconvolution: *Geophysics*, **74**, no. 4, L53-L65.

Fedi M., and Abbas M.A., 2013, A fast interpretation of self-potential data using the depth from extreme points method: *Geophysics,* **78**, no. 2, E107-E116. (in press)

Flosadottir, A. H., and S. Constable, 1996, Marine controlled source electromagnetic sounding 1. Modeling and experimental design: *Journal of Geophysical Research*, **101**, 5507–5517.

Gant F. S. and G. F. West, 1965, Interpretation theory in applied geophysics: McGraw-Hill Book Company.

Jin J., 2002, The finite element method in electromagnetic: John Wiley & Sons

Key, K., 2009, 1D inversion of multicomponent, multifrequency marine CSEM data: Methodology and synthetic studies for resolving thin resistive layers: *Geophysics*, **74**, no. 2, F9–F20.

Kraichman, M. B., 1970, Handbook of electromagnetic propagation in conductingmedia: U. S. Government Printing Office.

Lee, S., McMechrul, G. A, and Aiken, L. V., 1987, Phasefield imaging: The electromagnetic equivalent of seismic migration: *Geophysics*, 52, 679-693.

Li,Y., and K. Key, 2007, 2D marine controlled-source electromagnetic modeling: Part 1—An adaptive finite-element algorithm: *Geophysics*, **72**, no. 2,WA51–WA62.

Lien, M., and T. Mannseth, 2008, Sensitivity study of marine CSEM data for reservoir production monitoring: *Geophysics*, **73**, no. 4, F151–F163.

Løseth, L. O., H. M. Pedersen, B. Ursin, L. Amundsen, and S. Ellingsrud, 2006, Low-frequency electromagnetic fields in applied geophysics: Waves or diffusion?: *Geophysics*, **71**, no. 4, W29–W40.

Løseth, L. O., and B. Ursin, 2007, Electromagnetic fields in planarly layered anisotropic media: *Geophysical Journal International*, **170**, no. 1, 44–80

MacGregor, L.,M. Sinha, and S.Constable, 2001, Electrical resistivity structure of the ValuFa Ridge, Lau Basin, from marine controlled-source electromagnetic sounding: *Geophysical Journal International*, **146**, 217–236.

Maillet R., 1947, The fundamental equations of electrical prospecting: *Geophysics,***12**, 529–556.

Newman, G. A. and D. L. Alumbaugh, 1997, Three-dimensional massively parallel electromagnetic inversion: Part 1—Theory: *Geophysical Journal International*, **128**, no. 2, 345–354.

Newman, G. A., M. Commer, and J.J. Carrazone, 2010, Imaging CSEM data in the presence of electrical anisotropy: *Geophysics,* **75**, no. 2, F51-F61.

Orange, A., K. Key, and S. Constable, 2009, The feasibility of reservoir monitoring using time-lapse marine CSEM: *Geophysics*, **74**, no. 2, F21–F29.

Ramananjaona, C., L. MacGregor, and D. Andréis, 2011, Sensitivity and inversion of marine electromagnetic data in a vertically anisotropic stratified earth: *Geophysical Prospecting*, 59, 341–360.

Reid, A. B., J.M.Allsop, H. Granser, A. J. Millett, and I.W. Somerton, 1990, Magnetic interpretation in three dimensions using Euler deconvolution: *Geophysics*, **55**, 80–91.

Rust, W. M., 1938, A historical review of electrical prospecting methods: *Geophysics*, **3**, 1–6.

Schlumberger, C., M. Schlumberger, and E. G. Leonardon, 1934, Electrical exploration of water-covered areas: Transactions of the American Institute of Mining and Metallurgical Engineers, **110**, 122–134.

Schwalenberg, K., E.Willoughby, R. Mir, and R. N. Edwards, 2005,Marine gas hydrate electromagnetic signatures in Cascadia and their correlation with seismic blank zones: *First Break*, **23**, 57–63.

Schwalenberg, K.,W.Wood, I. Pecher, L. Hamdan, S. Henrys, M. Jegen, and R. Coffin, 2010, Preliminary interpretation of electromagnetic, heat flow, seismic, and geochemical data for gas hydrate distribution across the Porangahau Ridge, New Zealand: *Marine Geology*, **272**, no. 1–4, 89–98.

Sinha, M. C., P. D. Patel, M. J. Unsworth, T. R. E. Owen, and M. R. J. Mac-Cormack, 1990, An active source EM sounding system for marine use: *Marine Geophysical Research*, **12**, 59–68.

Stavrev, P. Y., 1997, Euler deconvolution using differential similarity transformations of gravity or magnetic anomalies: *Geophysical Prospecting*, **45**, 207–246.

Telford W.M., L.P. Geldart, R.E. Sheriff, 1990, Applied geophysics. 2nd edition: Cambridge university press.

Thompson, D. T., 1982, EULDPH: A new technique for making computer assisted depth estimates from magnetic data: *Geophysics*, **47**, 31–37.

Unsworth, M., and D. Oldenburg, 1995, Subspace inversion of electromagnetic data: Application to mid-ocean-ridge exploration: *Geophysical Journal International*, **123**, 161–168.

Unsworth, M. J., B. J. Travis, and A. D. Chave, 1993, Electromagnetic induction by a finite electric dipole source over a 2-D earth: *Geophysics*, **58**, 198–214.

Ward S.H., G. W. Hohmann, 1988, Electromagnetic theory for geophysical applications, *in* M. Nabighian, ed., Electromagnetic Methods in Applied Geophysics, 1: SEG, chap. 4.

Webb, S., Constable, S. C., Cox. C. S. and Deaton. T. K ..1985, A seafloor electric field instrument: *J. Geomagn. Geoelectr*.,**37**,1115-1129.

Weiss, C. J., and S. Constable, 2006, Mapping thin resistors and hydrocarbons with marine EM methods: Part 2 — Modeling and analysis in 3D: *Geophysics*, **71**, no. 6, G321–G332.

Weitemeyer, K. A., S. C. Constable, K.W. Key, and J. P. Behrens, 2006, First results from a marine controlled-source electromagnetic survey to detect gas hydrates offshore Oregon: *Geophysical Research Letters*, **33**, no. 3.

Wright, D. A., A. Ziolkowski, and B. A. Hobbs, 2001, Hydrocarbon detection with a multi-channel transient electromagnetic survey: 71stAnnual InternationalMeeting, SEG, ExpandedAbstracts, 1435–1438.

Wynn, J. C., 1988, Titanium geophysics: The application of induced polarization to seafloor mineral exploration: *Geophysics*, **53**, 386–401.

Yuan, J., and R. N. Edwards, 2000, The assessment of marine gas hydrates through electronic remote sounding: Hydrate without a BSR?:*Geophysical Research Letters*, **27**, no. 16, 2397–2400.

Young, P. D., and C. S. Cox, 1981, Electromagnetic active source sounding near the East PacificRise: *Geophysical Research Letters*, **8**, 1043–1046.

Zach, J., and K. Brauti, 2009, Methane hydrates in controlled-source electromagnetic surveys—Analysis of a recent data example: *Geophysical Prospecting*, **57**, no. 4, 601–614.

Zhdanov M.S., P. Traynin, R. Booker, Underground imaging by frequency-domain electromagnetic migration, *Geophysics*, **61**, no.3, 666-682.

Zonge K. L., L. Hughes, 1991Controlled source audio-frequency magnetotelluric, *in* M. Nabighian, ed., Electromagnetic Methods in Applied Geophysics, 2: SEG, 713–807.

Appendix 1

Electromagnetic induction equations.

This appendix is taken from Chave et al. (1991).

The Maxwell's equations in the quasi-static limit with all electric current terms except the conduction current neglected are:

$$\nabla \cdot \mathbf{B} = 0 \tag{A1.1}$$

$$\nabla \times \mathbf{E} + \frac{\partial}{\partial t}\mathbf{B} = 0 \tag{A1.2}$$

$$\nabla \times \mathbf{B} - \mu_0 \sigma \mathbf{E} = \mu_0 \mathbf{J} \tag{A1.3}$$

where **E** and **B** are the electric field and magnetic induction, $\mu_0$is the magnetic permeability of free space, σ is the electrical conductivity, and **J** is the impressed source electric current density. Using a Mie representation (Backus, 1986), the magnetic induction may be written:

$$\mathbf{B} = \hat{\mathbf{z}} \times \nabla_h \Pi + \nabla_h \frac{\partial}{\partial z} \Psi - \nabla_h^2 \Psi \hat{\boldsymbol{z}} \tag{A1.4}$$

where ∇_h denotes the horizontal gradient operator and II and Ψ are scalar functions representing toroidal and poloidal magnetic (TM and PM) modes, as discussed in the text. The source current in equation (A3) may be decomposed in a similar way to equation (A4):

$$\mathbf{J} = \hat{\mathbf{z}} \times \nabla_h Y + \nabla_h T + \Xi \hat{\mathbf{z}} \tag{A1.5}$$

where Ξ is the vertical part of the source current and Y and *T* are scalar functions which satisfy the Poisson equations:

$$\nabla_h^2 Y = (\nabla \times \mathbf{J}) \cdot \hat{\mathbf{z}} \tag{A1.6}$$

$$\nabla_h^2 T = \nabla_h \cdot \mathbf{J}. \tag{A1.7}$$

lf the electric fie/d is also written in terms of three. scalars, the conductivity profile is assumed to vary only vertically, and the Cartesian components of equations (A2) and (A3) are written out explicitly, it can be shown, using the properties of analytic functions of a complex variable, that the modal scalars satisfy the differential equations:

$$\nabla_h^2 \Pi + \sigma \frac{\partial}{\partial z}\left(\frac{\partial}{\partial z}\frac{\Pi}{\sigma}\right) - \mu_0 \sigma \frac{\partial}{\partial t}\Pi = \mu_0 \Xi - \mu_0 \sigma \frac{\partial}{\partial z}\left(\frac{T}{\sigma}\right) \qquad \text{(A1.8)}$$

$$\nabla^2 \Psi - \mu_0 \sigma \frac{\partial}{\partial t}\Psi = \mu_0 Y \qquad \text{(A1.9)}$$

and the electric field is given by:

$$\mathbf{E} = \hat{\mathbf{z}} \times \nabla_h \frac{\partial}{\partial t}\Psi - \nabla_h \left[\frac{\left(\frac{\partial}{\partial z}\frac{\Pi}{\mu_0} + T\right)}{\sigma}\right] + \frac{\left(\nabla_h^2 \frac{\Pi}{\mu_0} - \Xi\right)}{\sigma \hat{\mathbf{z}}}. \qquad \text{(A1.10)}$$

The differences between equation (A8) and equation (A9) are caused by the nature of the electric currents associated with the two modes. Equation (A8) reduces to that for dc resistivity sounding in the zero frequency limit, while equation (A9) is the usual diffusion equation of EM induction.

The modal equations can be solved conveniently by constructing Green functions which incorporate the necessary EM boundary conditions at the seafloor and sea surface, which are assumed to be flat interfaces. Assuming $e^{i\omega t}$ time dependence, expressing the horizontal spatial components as the Fourier transform pair defined by:

$$\hat{\mathbf{f}}(\eta, \xi) = \iint_{-\infty}^{\infty} dx dy f(x, y) e^{i(\eta x + \xi y)}$$

and

$$f(x, y) = \frac{1}{(2\pi)^2} \iint_{-\infty}^{\infty} d\eta d\xi \hat{\mathbf{f}}(\eta, \xi)\, e^{-i(\eta x + \xi y)} \qquad \text{(A1.11)}$$

and assuming an ocean depth H and conductivity σ_0, then placing the coordinate origin (z = 0) at the seafloor yields:

$$\widehat{\mathbf{\Pi}} = \mu_0 \int_0^H dz' g_\pi(z,z') \widehat{\mathbf{\Xi}}(z') + \mu_0 \int_0^H dz' g_\pi(z,z') \widehat{\mathbf{T}}(z') \tag{A1.12}$$

$$\widehat{\mathbf{\Psi}} = \mu_0 \int_0^H dz' g_\psi(z,z') \widehat{\mathbf{Y}}(z,z') \tag{A1.13}$$

where the Green functions are:

$$g_\pi(z,z') = -\frac{\left[e^{-\beta|z-z'|} + R_L^{TM} e^{-\beta(z+z')} - e^{-2\beta H} e^{\beta(z+z')} - R_L^{TM} e^{-2\beta H} e^{\beta|z-z'|}\right]}{[2\beta(1 + R_L^{TM} e^{-2\beta H})]} \tag{A1.14}$$

$$g_\psi(z,z') = -\frac{\left[e^{-\beta|z-z'|} + R_L^{PM} e^{-\beta(z+z')} + R_A^{PM} e^{-2\beta H} e^{\beta(z+z')} + R_A^{PM} R_L^{PM} e^{-2\beta H} e^{\beta|z-z'|}\right]}{[2\beta(1 - R_A^{PM} R_L^{PM} e^{-2\beta H})]} \tag{A1.15}$$

where R_A are the reflection coefficients at the sea surface and R_L are the reflection coefficients at the seafloor.

These coefficients are given by:

$$R_L^{TM} = \frac{\frac{\beta K}{\sigma_0} - 1}{\frac{\beta K}{\sigma_0} + 1}$$
$$R_A^{PM} = \frac{\beta - K}{\beta + K} \tag{A1.16}$$
$$R_L^{PM} = \frac{\beta\Lambda - 1}{\beta\Lambda + 1}$$

where K and Λ are TM and PM mode response functions which contain all of the information on conductivity below the seafloor necessary to solve the problem and the induction parameter is:

$$\beta = \sqrt{k^2 + i\omega\mu_0\sigma_0} \tag{A1.17}$$

with the composite wavenumber given by $k = \sqrt{\eta^2 + \xi^2}$. Expressions for the modal response functions for both layered and continuous conductivity profiles are given in Chave and Cox (1982), and their different functional forms are caused by the disparate sensitivity of the two modes to electrical structure. Since the reflection coefficients are in general complex, the EM induction phenomena they represent are complicated, involving leaky surface or evanescent waves.

Appendix 2

For the 1D case (in which the earth is represented by a stack of layers), the radial component of the electric field can be decomposed as:

$$E_r = E_r^{TM} + E_r^{PM} \tag{A2.1}$$

Hence, Andréis and MacGregor (2008), starting from the Maxwell's equations, have evaluated the analytic expression of the TM and PM modes for the radial electric field of an HED positioned at an height *z'* above the sea-floor and calculated at a receiver lying at height *z* above the sea-floor:

$$E_r^{TM} = \frac{p}{4\pi\sigma_0}\cos\phi \int_0^\infty \beta_0 \left(kj_0(kr) - \frac{j_1(kr)}{r} \right) \frac{1}{1 - R_{air}^{TM} R_L^{TM}} \times \left(-e^{-\beta_0(z'-z)} + R_L^{TM} e^{-\beta_0(z+z')} + R_{air}^{TM} e^{-\beta_0(z+z')} - R_L^{TM} R_{air}^{TM} e^{\beta_0(z'-z)} \right) dk \tag{A2.2}$$

$$E_r^{PM} = \frac{p}{4\pi\sigma_0}\cos\phi \int_0^\infty \frac{i\omega\mu_0\sigma_0 j_1(kr)}{r\beta_0} \times \frac{1}{1 - R_{air}^{PM} R_L^{PM}} \left(-e^{-\beta_0(z'-z)} + R_L^{PM} e^{-\beta_0(z+z')} + R_{air}^{PM} e^{-\beta_0(z+z')} - R_L^{PM} R_{air}^{PM} e^{\beta_0(z'-z)} \right) dk \tag{A2.3}$$

where r is the distance between the source and receiver, ϕ is azimuth defined as the angle between the dipole axis and the line joining source and receiver, P is the source dipole moment, σ_0 is the conductivity of the seawater layer, k is the horizontal wave-number and β_0 is the complex

wave-number in the sea defined as $\beta_0 = \sqrt{k^2 - i\omega\mu_0\sigma_0}$. J_0 and J_1 are first and second order Bessel functions respectively, defined in equations A2.4 and A2.5 as:

$$j_0(kr) = \sum_{n=0}^{\infty} \frac{(-1)^n}{2^{2n}(n!)^2}(kr)^{2n} \tag{A2.4}$$

$$j_1(kr) = \sum_{n=0}^{\infty} \frac{(-1)^n}{2^{2n+1}n!\,(1+n!)}(kr)^{2n+1} \tag{A2.5}$$

Information about the resistivity structure in which the field diffuses is contained in reflection coefficients R_L and R_{air}. More precisely, information about the earth is contained in coefficients R_L, which are calculated by applying the boundary conditions for the field components recursively at each material boundary in the structure starting from the deepest layer (Figure 1.4) (Andréis and MacGregor, 2008). R_L^{TM} and R_L^{PM} in the layer $l-1$ on the interface with layer l underneath are expressed in equations A2.6 and A2.7 respectively:

$$R_{l-1\to l}^{TM} = \frac{\frac{\beta_{l-1}\sigma_1 - \sigma_{l-1}\beta_1}{\beta_{l-1}\sigma_1 + \sigma_{l-1}\beta_1} + R_{l\to l+1}^{TM} e^{-2\beta_l H_l}}{1 + R_{l\to l+1}^{TM}\frac{\beta_{l-1}\sigma_1 - \sigma_{l-1}\beta_1}{\beta_{l-1}\sigma_1 + \sigma_{l-1}\beta_1} e^{-2\beta_l H_l}} \tag{A2.6}$$

$$R_{l-1\to l}^{PM} = \frac{\frac{\beta_{l-1} - \beta_1}{\beta_{l-1} + \beta_1} + R_{l\to l+1}^{PM} e^{-2\beta_l H_l}}{1 + R_{l\to l+1}^{PM}\frac{\beta_{l-1} - \beta_1}{\beta_{l-1} + \beta_1} e^{-2\beta_l H_l}} \tag{A2.7}$$

Instead, the reflection coefficients R_{air}^{TM} and R_{air}^{PM} represent the reflection coefficients of TM and PM mode at the interface air-sea and depend on the water depth H_0, the conductivities of air and sea-water and the frequency of the signal. These coefficients are given by:

$$R_{air}^{TM} = \frac{\beta_0\sigma_{air} - \sigma_0\beta_{air}}{\beta_0\sigma_{air} - \sigma_0\beta_{air}} e^{-2\beta_0 H_0} \tag{A2.8}$$

$$R_{air}^{PM} = \frac{\beta_0 - \beta_{air}}{\beta_0 + \beta_{air}} e^{-2\beta_0 H_0}. \tag{A2.9}$$

Reflection coefficients are expressed in the horizontal wave-number domain and in the vertical spatial domain. If we assume that the air is infinitely resistive, the TM mode reflection coefficient at the sea surface is -1, instead the R_{air}^{PM} will be given by:

$$R_{air}^{PM} = \frac{\beta_0 - \beta_{air}}{\beta_0 + \beta_{air}} = \frac{\beta_0 - k}{\beta_0 + k}, \quad \text{where} \sigma_{air} \to 0 \tag{A2.10}$$

So, in contrast to the TM mode, the amplitude of the PM mode reflection coefficient is not equal to one (except at zero wave-number), allowing transmission of signals into the air. This indicates that PM and TM mode signals interact differently with the air-sea interface, with the PM mode contributing primarily to the classic *airwave* signature (Andréis and MacGregor, 2008)

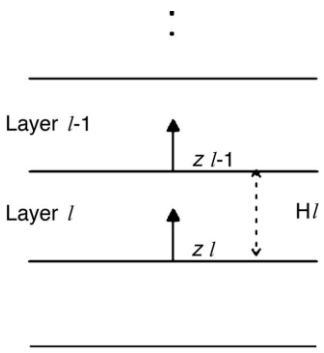

Figure 1.4: *from Andréis et al. (2008); schematic of the referential used for the recursive reflection coefficient calculation. Here, l=0 is the seawater layer with water depth H_0, l=1 is the first earth layer with thickness Hl, and l increases with depth in the earth.*

Appendix 3

Application of the Multiridge and DEXP methods to the horizontal component of the electric scattered field, E_x.

To demonstrate that the methods are applicable successfully to all the components of the electromagnetic fields, the Multiridge and DEXP methods was tested also considering the E_x component of the electromagnetic scattered field.

For example, the methods were applied to the E_x scattered field by a buried resistive sphere obtained starting from the model shown in Figure 3.2 and described in Paragraph 3.2. In particular, in Figure A3.1 is shown the amplitude of field. So, to demonstrate de applicability of the Multiridge method, the real part of the simulated E_z was continued (using a 3D static continuation), in the frequency domain, using a step ΔZ=10 m until the height 2000 m, as shown in Figure A3.2, and then was evaluated the ridges using the Canny' s method described in Paragraph 3.2. In particular, the pink lines in Figure A3.2 are referred to the zeros of the first vertical derivative of the field and the yellow lines are referred to the zeros of the first horizontal derivative of the field. As we can see from this figure, also in this case, as happens for the E_z component, the ridges are not straight lines at all the altitudes, but can be considered straight near the source (the resistive sphere); in fact, as we have mathematically demonstrated in Paragraph 3.1, they are expected to be straight at distances lower than skin-depth (δ). Hence, as expected, extending downward the straight part of the ridges, they intersect at x_0, y_0, as mathematically demonstrated. In particular, the dipolar nature of the electric field is more evident when E_x component is considered rather then we consider the vertical component E_z. For this reason, as widely explained in Chapter 3, we cannot estimate perfectly the horizontal

source position x_0, or we can improve the result considering the analytic signal that reduces a dipolar anomaly in a monopolar anomaly. In fact, in this case, considering only the real part of E_x the ridges converge at x=0 m but the horizontal position of the sphere is at x=100 m, as shown in Figures A3.2 and A3.3. Moreover, also in this case, the number of ridges increases increasing the derivative order, as shown in Figure A3.3 which represent the second order vertical derivative of the real part of E_x with the relative ridges, so that deriving the field we can better locate the anomalous body. Starting from the field shown in Figure A3.3, I have tested also the DEXP method which is described in Paragraph 3.3. So, the upward continued field, shown in figure A3.2, was scaled using the structural index estimated using the criterion of DEXP scaling function intercept (Fedi, 2007), considering the portion of the ridge surrounded by the white dotted line in Figure A3.2, described in Paragraph 3.3.3. The obtained result as shown, in Figure A3.4, is that the structural index, N, we have to use to have the DEXP imaged field is 3 in agreement with those reported in Table 3.1.

Hence, the field in figure A3.2 was scaled using the estimated structural index obtaining as result the DEXP imaged field shown in Figure A3.5. Also in this case, as for the Multiridge method, the depth of the source is perfectly estimated but the source is not perfectly located on the x-axis. This is, as we already said, due to the dipolar nature of the field that is even more evident when we consider the E_x component rather than the E_z component of the electric scattered field.

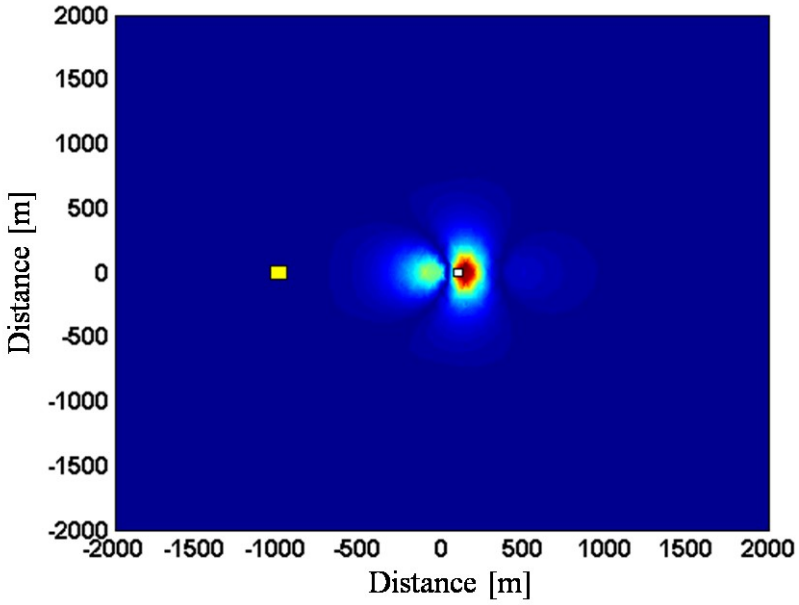

Figure A3.1: *Amplitude of the E_x component of the electromagnetic field scattered by a homogeneous resistive sphere obtained starting from the model described in Figure 3.2. The yellow square represent the receiver position. The white square represent the source position.*

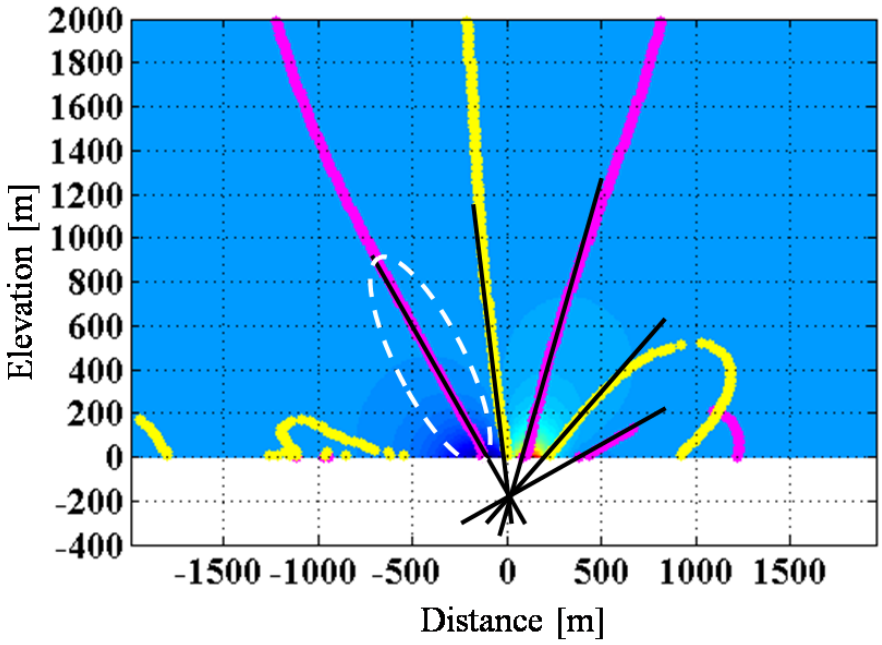

Figure A3.2: *upward-continuation of the real part of E_x scattered by a homogeneous resistive sphere at y=0. The pink lines are referred to the zeros of the first vertical derivative of the field; the yellow lines are referred to the zeros of the first horizontal*

derivative of the field. The dotted white line represents the portion of ridge that we have taken into account for the structural index estimation (see Paragraph 3.3.3).

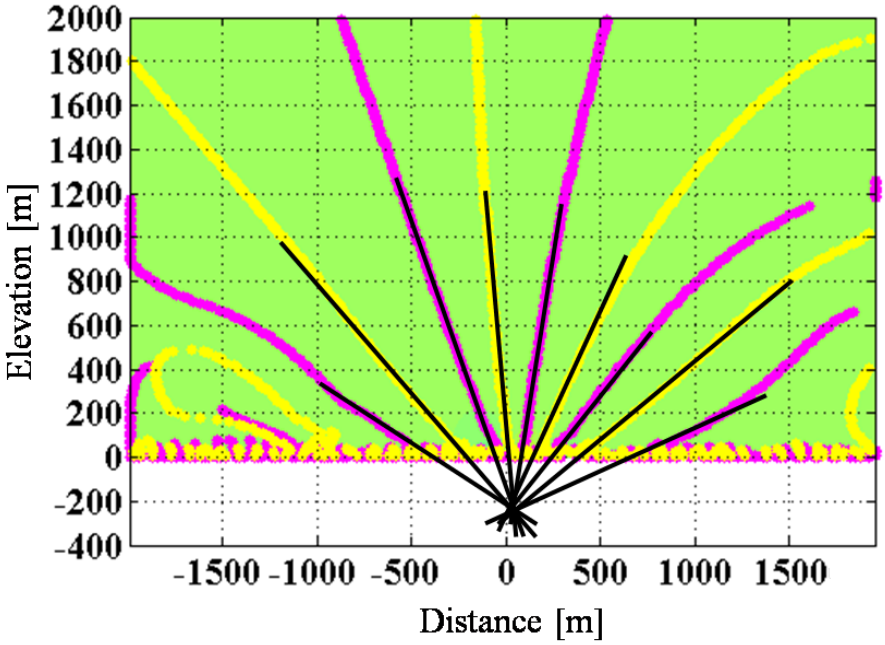

Figure A3.3: *second order vertical derivative of the upward-continuation of the real part of E_x scattered by a homogeneous resistive sphere at y=0. The pink lines are referred to the zeros of the third vertical derivative of the field; the yellow lines are referred to the zeros of the third horizontal derivative of the field.*

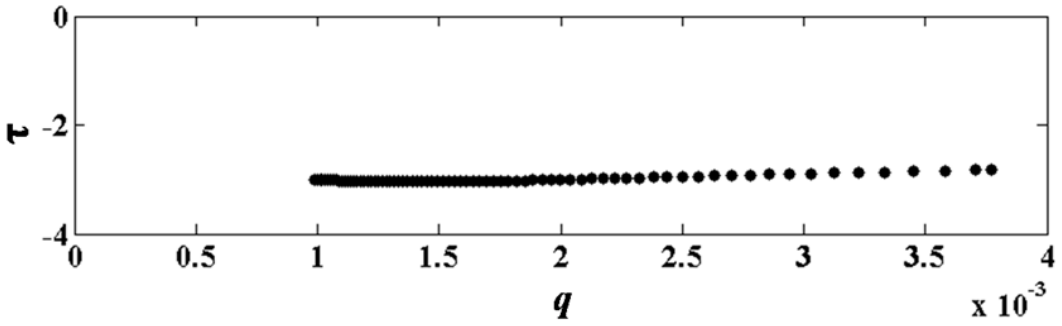

Figure A3.4: *estimation of the structural index obtained using the criterion of DEXP scaling function intercept (Fedi, 2007), obtained considering the portion of ridge shown in Figure A3.2.*

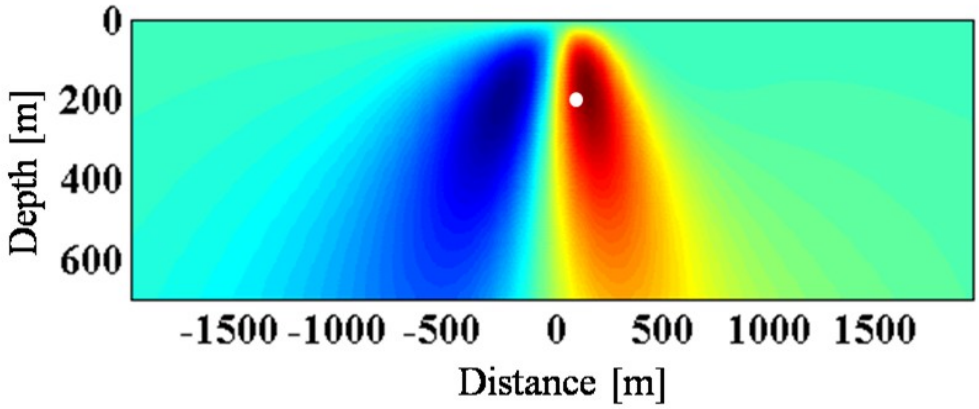

Figure A3.5: *DEXP imaged field obtained starting from the upward-continued field in Figure A3.2 using as structural index 3. The white circle represents the source position.*

Then, the Multiridge and DEXP method was tested considering also the other two kinds of one point sources described in Chapter 3, which are the horizontal infinite cylinder and the semi-infinite horizontal layer.

So, in Figure A3.6 is shown the amplitude of the field scattered by a horizontal infinite cylinder obtained starting from the model in Figure 3.6. Also in this case was applied the Multiridge method upward-continuing the field shown in Figure A3.6 and then evaluating the ridges using the Canny's method (Figure A3.7). Also for this case, are valid all remarks made for the previous cases and then the ridges are not straight at all the altitudes, but are straight until an altitude approximately equal to the skin depth (δ). Also in this case, the straight parts of the ridges converge at a depth perfectly equal to the source depth (Figure A3.7), but the dipolar nature of the field does not permit to estimate exactly the horizontal position of the source considering only the real part of the field. So, to have a better result, the Multiridge method was applied first to the amplitude of the E_x scattered field (Figure A3.8), obtained upward-continuing separately the real and imaginary part of the field and then evaluating the amplitude.

Then, scaling the field shown in Figure A3.7 using the structural index, N, estimated using the criterion of DEXP scaling function intercept (Fedi, 2007), considering the portion of the ridge delimited by the white dotted line, we have obtained the DEXP imaged field (Figure A3.10). As

shown in Figure A3.9, the estimated structural index for this case is 2, in agreement with what reported in Table 3.1. The result obtained in Figure 3.10 gives information about the source location but we can improve our result applying the DEXP method to the second order vertical derivative of the E_x upward continued field (Figure A3.11). As shown in Figure A3.11 the source depth is perfectly estimated, but, as happens all the time we consider only the real part of the electric field, the horizontal position of the anomalous body, located between the two extremes point shown in Figures A3.10 and A3.11, cannot be perfectly estimated. So, to better locate the anomalous body, is better to apply the method to the analytic signal of the scattered E_x component (Figure A3.12).

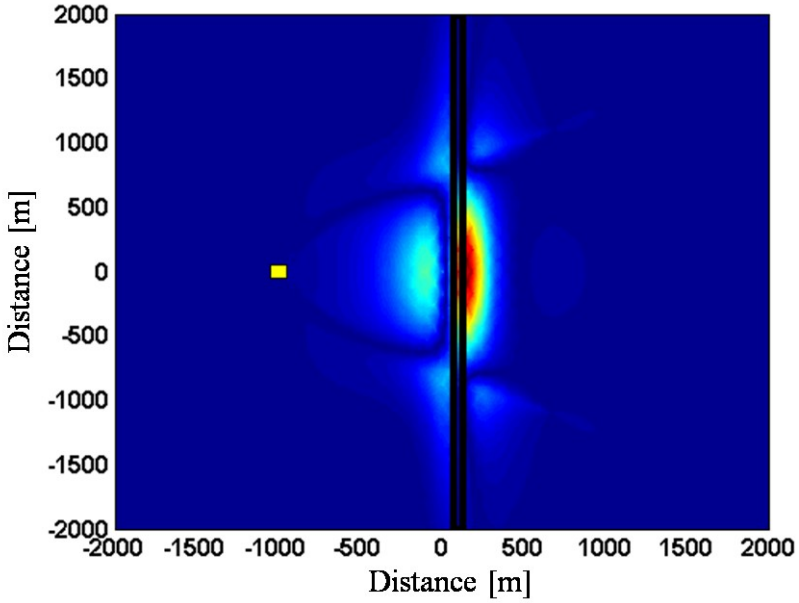

Figure A3.6: *Amplitude of the E_x component of the electromagnetic field scattered by a homogeneous resistive horizontal cylinder obtained starting from the model described in Figure 3.6. The yellow square represent the receiver position. The black rectangle represents the source position.*

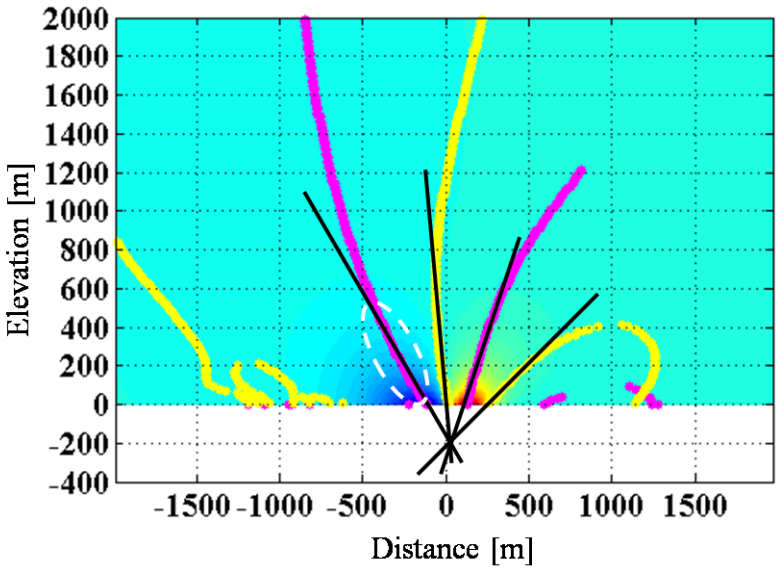

Figure A3.7: *upward-continuation of the real part of E_x scattered by a homogeneous resistive horizontal cylinder at y=0. The pink lines are referred to the zeros of the first vertical derivative of the field; the yellow lines are referred to the zeros of the first horizontal derivative of the field. The dotted white line represents the portion of ridge that we have taken into account for the structural index estimation (see Paragraph 3.3.3).*

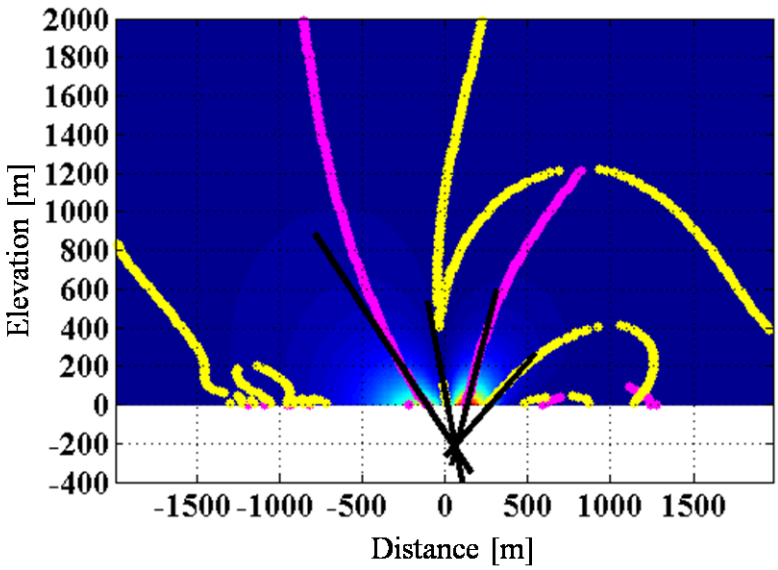

Figure A3.8: *Application of the Multiridge method to the field shown in Figure A3.6.*

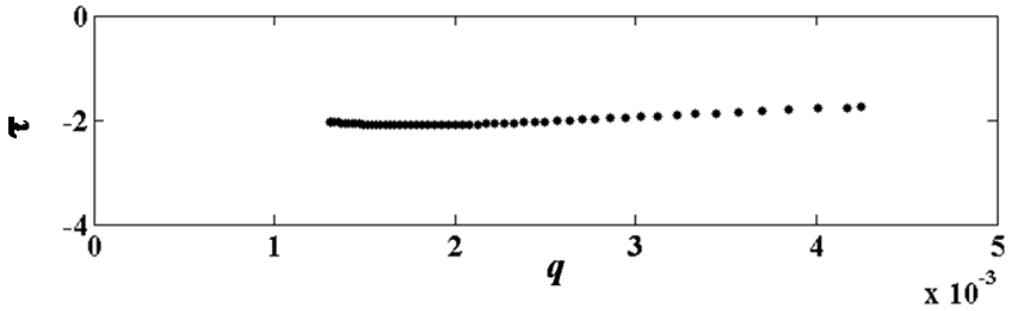

Figure A3.9: *estimation of the structural index obtained using the criterion of DEXP scaling function intercept (Fedi, 2007), obtained considering the portion of ridge shown in Figure A3.7.*

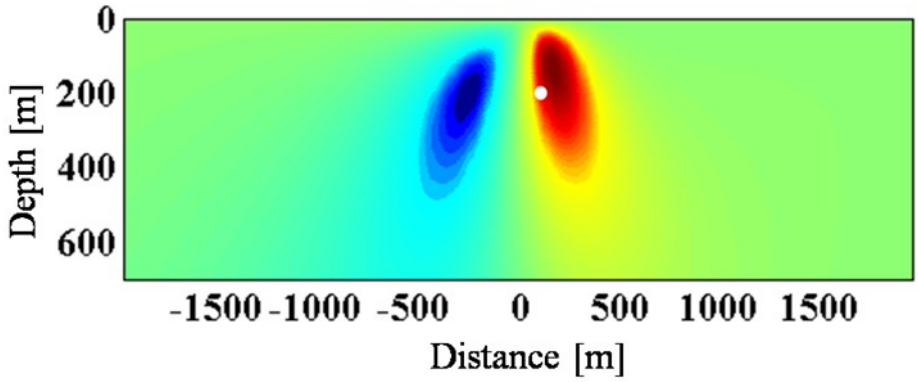

Figure A3.10: *DEXP imaged field obtained starting from the upward-continued field in Figure A3.7 using as structural index 2. The white circle represents the source position.*

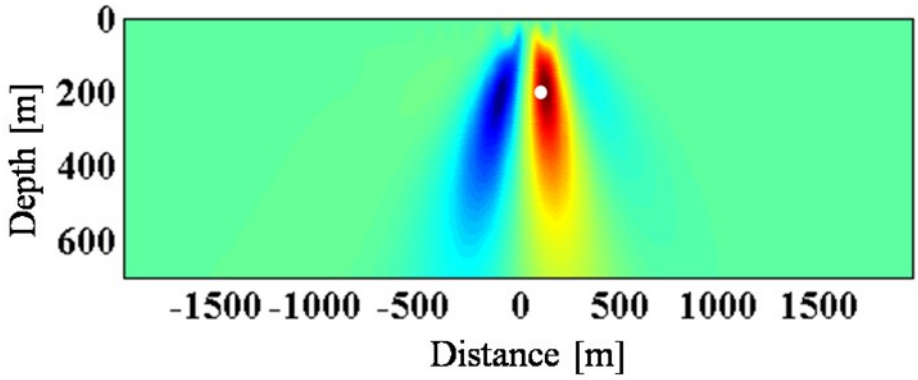

Figure A3.11: *DEXP imaged field obtained starting from the second order vertical derivative of the upward-continued field in Figure A3.7 using as structural index 2. The white circle represents the source position.*

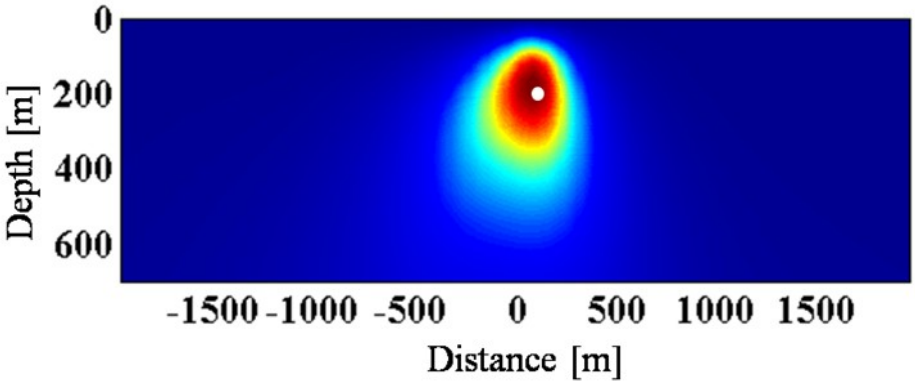

Figure A3.12: *DEXP imaged field obtained starting from the analytic signal of the E_x scattered field, obtained starting from the model shown in Figure 3.6, using as structural index 2. The white circle represents the source position.*

The last case we have considered is that of a semi-infinite horizontal thin layer. So, starting from the model shown in Figure 3.11, was obtained the E_x component of the scattered field. In Figure A3.13 is shown the amplitude of the scattered field. In Figure A3.14 is shown, instead, the real part of E_x. As we can see from this figure, the shape of the anomaly is very different from that observed for the E_z component, but also in this case we can apply successfully both Multiridge and DEXP methods.

Regarding the Multiridge method, in Figure A3.15 is shown the upward-continued field, obtained starting from the field shown in Figure A3.14. As we can see from the figure, extending the strength part of the ridges downward, they converge at a depth equal to the source depth. Then, was applied also the DEXP method. In particular, was first estimated the structural index, using the the criterion of DEXP scaling function intercept (Fedi, 2007), considering the portion of the ridge surrounded by the white dotted line in Figure A3.15 (Figure A3.16). As we see from Figure A3.16, the right structural index we have to use is 1, which is the same value give in Table 3.1 for a semi-infinite horizontal thin layer. So, the field in Figure A3.15 was scaled using the right structural index and was obtained the DEXP imaged field shown in Figure A3.17. From this figure we see that we can estimate perfectly the source depth, indicated by the extreme point of the DEXP imaged field, which in this case is a minimum. Regarding the lateral extension of the anomalous body, we see just the part of the field closest to the receiver, which is located at

x=-1000 m. To have a complete imaging of the anomalous body, we have to apply the DEXP method to data acquired by several receivers and then merge the results, as effectively showed in Chapter 3.

Finally, to have a better result, also in this case we have applied the DEXP method to the analytic signal of the E_x scattered field. In this case, the source location is represented by the maximum of the DEXP imaged field. However, the application of this method to this kind of body is affected by all the limitations described in Chapter 3 linked to the fact that the this body cannot be considered a perfect one point source because, in reality, this body is seen as a finite thin layer due to the fact that just a part of the source contributes effectively to the scattered field.

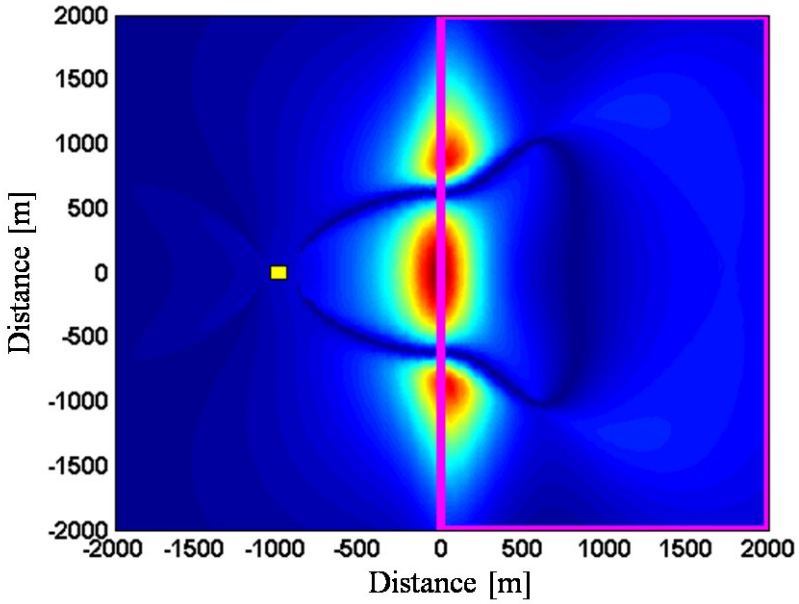

Figure A3.13: *Amplitude of the E_x component of the electromagnetic field scattered by a homogeneous resistive horizontal semi-infinite thin sheet obtained starting from the model described in Figure 3.11. The yellow square represent the receiver position. The pink rectangle represents the geological source position.*

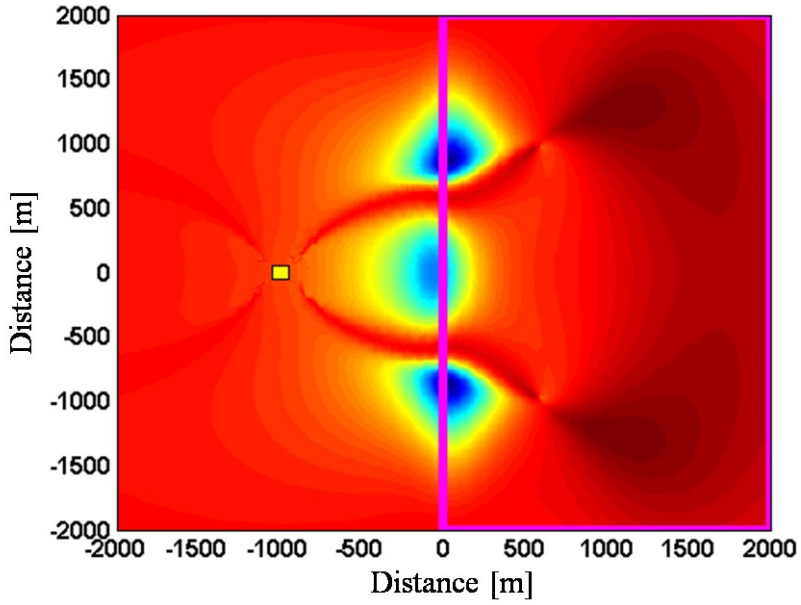

Figure A3.14: *Real part of the E_x component of the electromagnetic field scattered by a homogeneous resistive horizontal semi-infinite thin sheet obtained starting from the model described in Figure 3.11. The yellow square represent the receiver position. The pink rectangle represents the source position.*

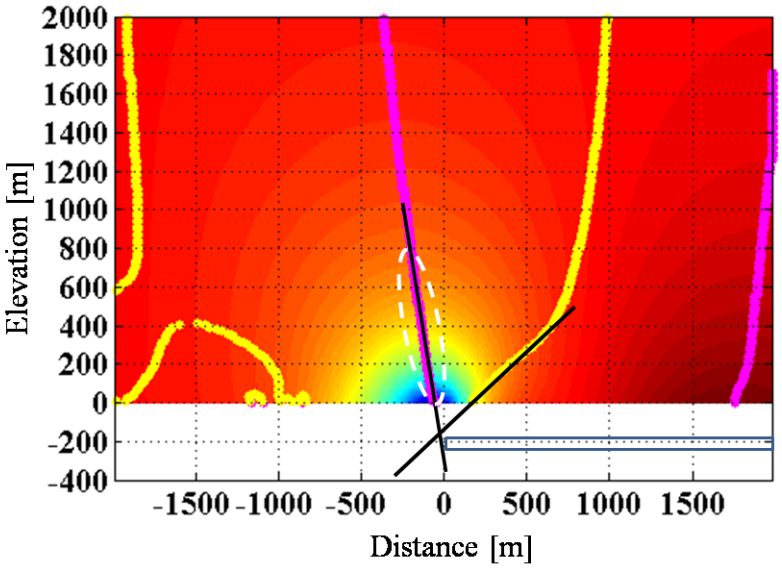

Figure A3.15: *upward-continuation of the real part of E_x scattered by a homogeneous resistive semi-infinite thin layer at y=0. The pink lines are referred to the zeros of the first vertical derivative of the field; the yellow lines are referred to the zeros of the first horizontal derivative of the field. The dotted white line represents the portion of ridge that we have taken into account for the structural index estimation (see Paragraph 3.3.3).*

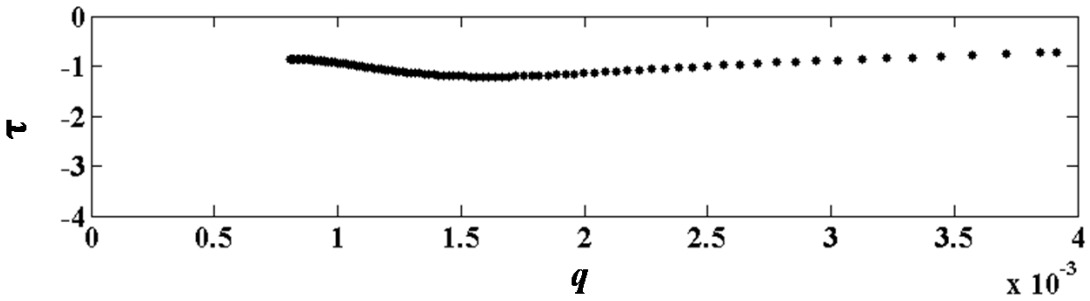

Figure A3.16: *estimation of the structural index obtained using the criterion of DEXP scaling function intercept (Fedi, 2007), obtained considering the portion of ridge shown in Figure A3.15.*

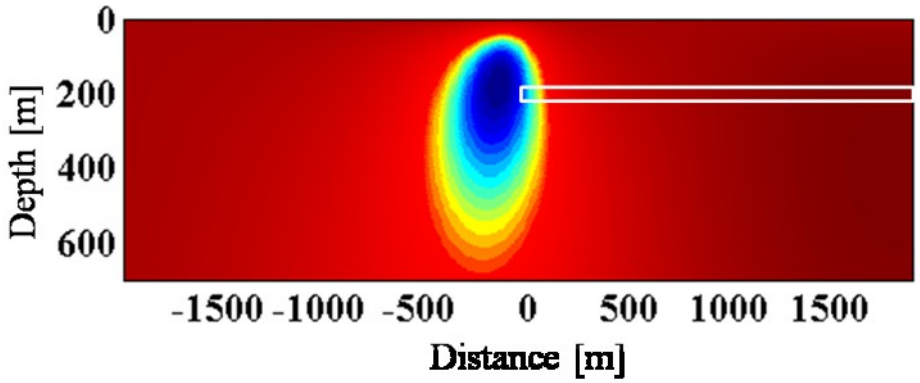

Figure A3.17: *DEXP imaged field obtained starting from the upward-continued field in Figure A3.15 using as structural index 1. The white rectangle represents the source position.*

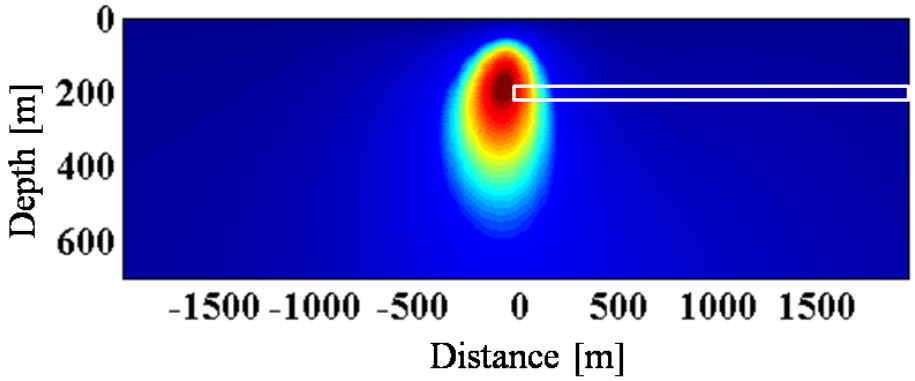

Figure A3.18: *DEXP imaged field obtained starting from the analytic signal of the E_x scattered field, obtained starting from the model shown in Figure 3.11, using as structural index 1. The white circle represents the source position.*

Acknowledgements

I would like to give my sincere thanks to my supervisor, Prof. Maurizio Fedi, who accepted me as PhD student without any hesitation. Thereafter, he offered me so much advice, patiently supervised me, and always guided me in the right direction. I have learned a lot from him, without his help I could not have finished my dissertation.

Special thanks are also given to eni e&p, in particular, to Dr. Luca Mapelli and Dr. Paolo Dell' Aversana, who offered me their time and the data for my case study.

Last but not least, I thank Dr. Francesco Italiano, for his very useful advices, Prof. Giovanni Florio and my friends Simone, Gabriella, Mahomud, Daniela and Mauro that shared with me these three years supporting me and filling my days with joy.